A79-41829

NASA TECHNICAL MEMORANDUM

NASA TM-75805

IMAGE PROPERTIES OF AN X-RAY TELESCOPE OF THE WOLTER-1 TYPE WITH EMPHASIS ON CONTRAST REDUCTION BY DIFFUSE REFLECTION

R. Lenzen

Translation of "Abbildungseigenschaften eines Roentgenteleskops vom Type Wolter-I unter besonderer Beruecksichtigung der Kontrastverminderung durch diffuse Reflexion". Tuebingen Universitaet, Fachbereich Physik, Doktor der Naturwissenschaften Dissertation, 1978, pp 1-123

(NASA-TM-75805) IMAGE PROPERTIES OF AN X-RAY TELESCOPE OF THE WOLTER-1 TYPE WITH EMPHASIS ON CONTRAST REDUCTION BY DIFFUSE REFLECTION Ph.D. Thesis (National Aeronautics and Space Administration) 105 p G3/89

N80-21224

Unclas 47553

NATIONAL AERONAUTICS AND SPACE ADMINISTRATION
WASHINGTON, D. C. 20546 JANUARY 1980

APR 1980
RECEIVED
NASA STI FACILITY
ACCESS DEPT.

STANDARD TITLE PAGE

1. Report No. NASA TM-75805	2. Government Accession No.	3. Recipient's Catalog No.
4. Title and Subtitle IMAGE PROPERTIES OF AN X-RAY TELESCOPE OF THE WOLTER-1 TYPE WITH EMPHASIS ON CONTRAXT REDUCTION BY DIFFUSE REFLECTION		5. Report Date January 1980 6. Performing Organization Code
7. Author(s) R. Lenzen		8. Performing Organization Report No. 10. Work Unit No. 11. Contract or Grant No. NASW-3198
9. Performing Organization Name and Address SCITRAN P. O. Box 5456 Santa Barbara, CA 93108		13. Type of Report and Period Covered Translation
12. Sponsoring Agency Name and Address National Aeronautics and Space Administration Washington, D. C. 20546		14. Sponsoring Agency Code

15. Supplementary Notes

Translation of "Abbildungseigenschaften eines Roentgenteleskops vom Type Wolter- I unter besonderer Beruecksichtigung der Kontrastverminderung durch diffuse Reflexion," Tuebingen Universitaet, Fachbereich Physik, Doktor der Naturwissenschaften Dissertation, 1978, pp 1-123 (A79-41829

16. Abstract

Theoretical and experimental results are presented on the geometrical-optic imaging properties of a Wolter-I type paraboloid-hyperboloid X-ray telescope. Particular consideration is given to the effect of microroughness of the mirror on the imaging properties. Experiments were conducted in which scattering properties were determined as a function of wavelength, incidence angle, and roughness of the plane mirrors. Results indicate the need for optimization of mirror material and polishing technology as well as the development of improved mirror manufacturing techniques. The use of transmission gratings along with the Wolter-I type telescope in spectroscopy applications is discussed.

17. Key Words (Selected by Author(s))	18. Distribution Statement Unclassified - Unlimited		
19. Security Classif. (of this report) Unclassified	20. Security Classif. (of this page) Unclassified	21. No. of Pages 105	22. Price

NASA-HQ

CONTENTS

1. Introduction 1

2. The X-Ray Telescope of the Type Wolter I

2.1. Basic Principles of the Telescope 3
2.2. Dimensioning and Effective Surface of the Telescope 5
2.3. Positioning and Dimensioning of Diaphragms 8
2.4. Design-related image errors 9

3. Reflection of X-rays: Reflectivity and Scattering

3.1. Survey 17
3.2. Reflection theory a) Reflection by matter under normal conditions 19
b) Reflection by the surface of a neutron start 21
3.3. Scattering Models 27
3.4. Scattering theory for statistically rough surfaces 29
3.5. Contribution by Thomson scattering 35
3.6. The influence of scattering on the image quality of the telescope 38

4. Scattering measurements

4.1. Experimental setup 44
4.2. Survey of the Investigated Samples and of the Measured Roughness 45
4.3. Integral Scattering Components 51
4.4. Scattering Distribution 60
4.5. Dependence of the Scattering on the Surface Treatment 64
4.6. Two-dimensional Scattering Distribution 65
4.7. Scattering Measurements on Replica Samples 70
4.8. Dependence of the Scattering on the Polishing Direction 72
4.9. Influence of the Roughness on the Integral Reflectivity 73

4.10 Comparison measurements of the roughness 78

5. Spectroscopy with Telescope and Transmission Grating

5.1. Introduction 87

5.2. Grating Errors and Correction Possibilities 87

5.3. Position of the Transmission Grating 92

6. Summary 94

7. References 96

8. Curriculum Vitae 101

INTRODUCTION

The rapid development of X-ray astronomy made it possible /1* that this field reached within three decades the level which optical astronomy achieved when Galileio pointed a telescope for the first time at the sky: The soft X-ray region (0.2 to 2.0 keV) has obtained by now the first imaging systems for the observation of extrasolar X-ray sources. By the end of the year 1978, HEAO-B will carry the first X-ray telescope for satellite-based observations of extrasolar sources.

After the first observations of cosmic X-ray sources (1949: first observation of the sun in the X-ray range from V2-rockets, 1962: discovery of the first extrasolar source, Sco X-1) an astronomical observational program got started, resulting in an extensive catalogue of cosmic X-ray sources (UHURU satellite) and surprising observations of individual sources (ANS, Ariel-5, SAS-3,)S)-8). At present, we know of about 300 cosmic X-ray sources, among them the novel types of Cyg X-3 or Her X-1 with their short-period fluctuations in brightness that have given theoreticians new ideas (neutron stars, black holes). These interesting results were obtained with the aid of instruments of small energy and angle resolution, such as mechanically collimated proportional counters with an angular resolution of some arcmin and an energy resolution of about $E/\Delta E = 5$. A second /2 generation of X-ray satellites (HEAO-B, EXOSAT) will make use of focussing imaging systems and use their advantages to improve the angular as well as the energy resolution (the latter by a combination with transmission gratings) by factors of order 10-50. The focussing systems have the added advantage of suppressing the background noise: The signal to noise ratio is improved corresponding to the large ratio of collector surface and detector surface. For instance, HEAO-B will have a sensitivity which is about 10^4 times that of the UHURU satellites.

*Numbers in margins indicate foreign pagination

The MPE (Max-Planck Institut fur Extraterrestrische Physik Garching, FRG) is currently involved in the development of an X-ray telescope which is supposed to be flow in three versions toward the end of the year 1978 in rockets. The concept of this telescope is not so much aimed at a high resolution (the design postulates asked for a resolution of about 20 arcsec and a FWHM width of less than 5 arcsec was reached; by comparison, the HEAO-B has a point resolution of 3.5 arcsec FWHM); instead the emphasis is on a low level of scattering background. The telescope is meant to be used for the study of extended X-ray sources, such as the supernova remnants in Vela, Puppis, and Cygnus, and for measuring the dust scattering halos of the type expected in the case of the bright sources such as Cyg X-1 due to scattering by interstellar dust. This task requires a high contrast, both with respect to the detector and the reflecting system proper: While Rayleigh's criterion

$$\sqrt{g} = \frac{4\pi \sin\alpha\, \sigma}{\lambda} \ll 1$$

is in the optical range reasonably satisfied even for perpendicular incidence and a roughness of $\sigma = 50$ Å. The value of g is unity for the same roughness, a wavelength of 10 Å and a typical grazing angle of 1 degree. As a consequence, there is always significant scattering radiation in the case of soft X-rays decreasing the contrast of the image of an X-ray telescope.

The present paper is concerned with the imaging properties of X-ray telescopes and is closely related to the development of this particular one. Special emphasis is placed on the analysis of the influence of the mirror microroughnesss on the point imaging function.

A computer code was developed to determine the geometrical-optics imaging properties of a paroboloid-hyperboloid telescope of the type described by H. Wolter [51]. This code allows to follow the ray path through the telescope and to determine in this fashion imaging errors, effective surfaces, and the influence of diaphrams. The influence of micro-roughness on the scattering behavior of X-rays under reflection by polished surfaces is computed for the telescope on the basis of the stat-

istical surface scattering theory [1]; the influence of volume /4
scattering is estimated. The scattering experiment provides measurements of the dependence of the integral scattering contribution and of the scattering distribution on the wavelength, the grazing angle, and the roughness of the plane mirros. The results are then compared with the results provided by theory. Scattering measurements are also used in checking the optimizing of the reflecting material and the polishing techniques, and also in studying novel methods for mirror production (replicas). The roughness obtained from scattering measurements by means of scattering theory are compared with other measurement techniques for surface roughness.

While this work was going on, the discovery of cylcotron line emission from HerX-1 brought up the question as to the reflection of X-rays from the surface of a neutron star with its extreme physical conditions. The computations we have carried out in this respect were added in Section 3.2b to this report.

A final section discusses the use of transmission gratings together with X-ray telescopes. We point out the possibility of increasing the spectral resolution through grating corrections. We also study the question as to the optimum position of the grating behind the telescope for a given wavelength and grazing angle range.

2. THE X-RAY TELESCOPE OF THE TYPE WOLTER I /5

2.1. Basic Principles of the telescope

The refractive index of all materials under normal conditions is for X-rays less than unity, with the departures from unity in the soft X-ray region (0.2 to 2 KeV) being of order 10^{-4} to 10^{-2} in the case of gold; c.f. Section 3.2. Thus, total reflection occurs in this energy range of electromagnetic radiation

below an angle of incidence which is obtained from the relation

$$\cos \alpha_c = Re(n) = 1 - \delta$$

If the angle α_c are small, we then have $\alpha_c = \sqrt{2\delta}$. Since the limiting angles for total reflection in the region of soft X-rays are between 0.5 and 8 degrees, mirror telescopes for X-rays are run under conditions of grazing incidence.

H. Wolter [51,52] suggested the design for such a telescope in 1951 for applications with soft X-rays. It is easy to show that mirror systems with an odd number of reflections under grazing incidence violate Abbe's sine conditions in an extreme fashion. Consequently, Wolter's telescope consists of two mirrors, that is, a paraboiloid and a confocal coaxial hyperboloid. The MPE developed in collaboration with the Zeiss Company (Oberkochen) a 32 cm telescope of the Wolter type 1 (Fig. 1). The radiation /6 which arrives at the paraboloid parallel to the optical axis is focussed toward the lhs focus and then impinges on the hyperboloid mirror which deflects it to the second (rhs) focus. Thus, radiation arriving parallel to the axis is focussed in ideal fashion, as would be the case for a single paraboloid. The difference to this case, however, is the fact that a source which is not situtated on the optical axis (at infinity) is imaged in a diffraction pattern in the focal plane with the center situated near the Gaussian image point and with the size of the diffraction pattern small by comparison with the displacement from the axis. The image errors of such a telescope and their measurability in the optical range of wavelengths are discussed in Section 2.5. Since the effective surface of a Wolter telescope is a ring surface, diaphragms are needed to prevent radiation to reach the detector without reflection. Additional diaphragms are used to protect the detector from singly reflected radiation. The effect these diaphragms have on the dependence of the collector surface of the telescope on the off-axis angle, that is, the angle be-

tween the direction of the incoming radiation with respect to the optical axis, is discussed in Section 2.3. We first, in Section 2.2, determine the parameters of the mirror surfaces and the dimension of the 32 cm telescope. /7

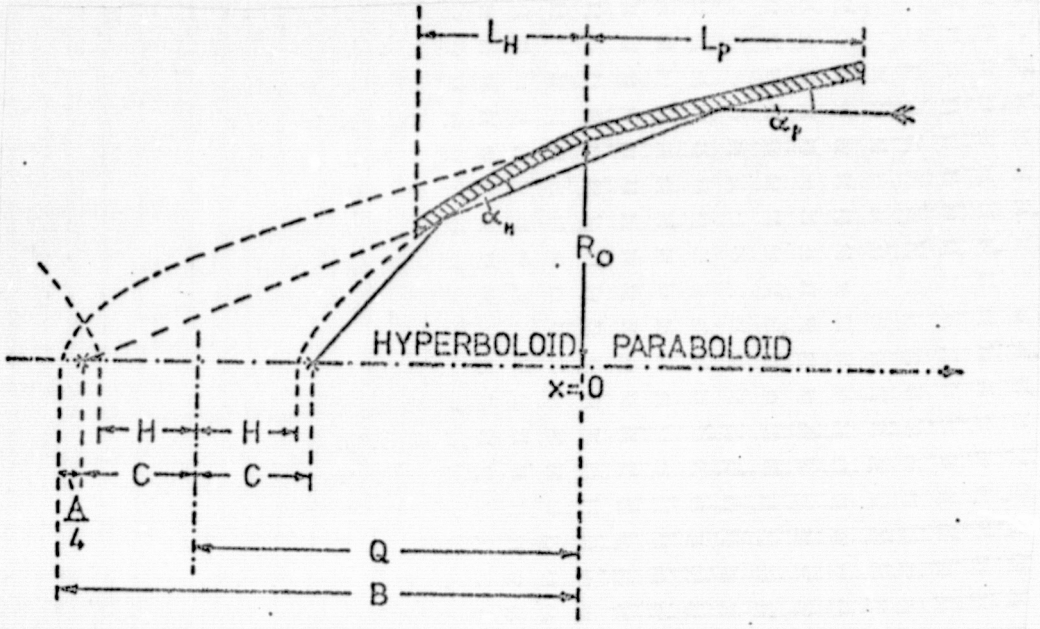

PARABOLOID: $R_p^2 = A(X + B)$

HYPERBOLOID: $R_H^2 = (C^2 - H^2)((X + Q)^2/H^2 - 1)$

Figure 1. Schematic drawing of the Wolter telescope Type I

2.2. Dimensioning and effective surface of the telescope

The determination of the relative position of the two mirrors with respect to each other (coaxially and confocally) restrict the freedom in the definition of the form to a total of three parameters. Together with the length of the individual mirrors the system is determined by five parameters. If the length of the hyperboloid mirror is chosen at least such that all the radiation reaching the paraboloid parallel to the axis hits the hyperboloid as well after the first reflection, then the geometrical collector surface for paraxial rays depends only on two

parameters: $F_{geom} = AL_p$; here, A is half of the distance between /8 focus and the directrix surface of the paraboloid, L_p is the axis length of the paraboloid mirror. The maximum interior radius of the telescope reads

$$r_v = \sqrt{A(L_p + B)}$$

If this radius is chosen for the representation of the paraboloid (it is limited by the size of the carrier rocket) together with the angle of incidence in the case of reflection of paraxial rays at the position x = 0, then we find for the geometrical collector surface

$$F_{geom} = 2\pi L_p \tan\alpha \left[L_p \tan\alpha - \sqrt{r_v^2 + L_p^2 \tan^2\alpha} \right] \qquad (1)$$

The effective collector surface is obtained by mutliplying the geometrical surface with the reflectivities $R(\alpha_p)$ and $R(\alpha_H)$. For slim Wolter-type telescopes we find that the sum of α_p and α_H is nearly constant. If $\alpha_p = \alpha - \varepsilon$, $\alpha_H = \alpha + \varepsilon$, then we have for the product of the two reflectivities /9

$$R(\alpha_p) \cdot R(\alpha_H) \approx R^2(\alpha) - [\varepsilon R'(\alpha)]^2 + \varepsilon^2 R''(\alpha)$$

In the range of energies of X-rays for which the telescope was optimized (1 to 1.5 KeV) the second derivative of the angle of incidence is negative (that is, for angles less than 2°). Then the product of the two reflectivities is a maximum, if $\alpha_{p_0} = \alpha_{H_0} = \alpha$. If $\alpha = 1.5°$, the computed effective surface shows a maximum for 1.5 KeV or about 8.3 Å. Thus, we have chosen an angle of incidence of 1.5° at the position of x = 0 for the 32 cm telescope. This completely determines the paraboloid together with the maximum radius of 160.9 mm and the axial length restricted to 430 for design reasons. The remaining two parameters of the hyperboloid were determined in such a fashion that on one hand the

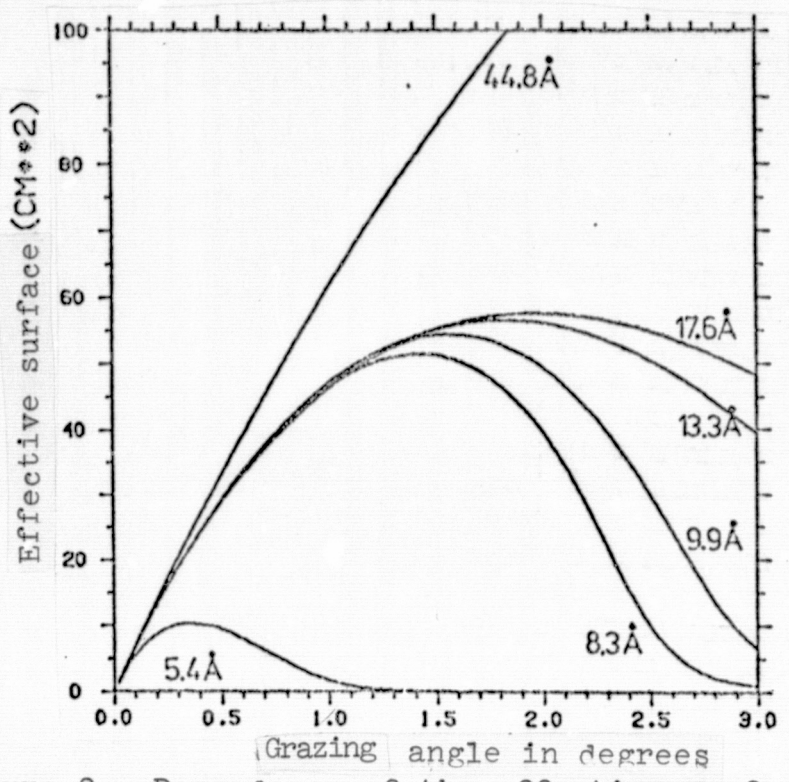

Figure 2. Dependence of the effective surface on the grazing angle. Optical constants according to B. Aschenback. L_p = 43 cm.

slope of the hyperboloid for x = 0 equals $\tan(3\alpha_p)$ (so that for x = 0 we have $\alpha_{H_o} = \alpha_{p_o}$), while on the other hand at the position x = 0 the radii of paraboloid and hyperboloid are the same. In this manner, we find the following parameters according to Fig. 1:

r_v (mm)	α	H (mm)	L_p (mm)	L_H (mm)
160.9	1.5°	715.5	430.0	380.0

The remaining radii and angles of incidence and the focal length are then obtained as follows:

r_o (mm)	A (mm)	B (mm)	C (mm)	Q (mm)	r_H (mm)	α_H	α_v	f (mm)
150.0	7.8	2864.1	717.5	2144.7	119.7	1.83°	1.40°	1427.2

Here, α_H is the grazing angle at which a paraxially incoming /10 ray is reflected at the hyperboloid, if it hits the telescope at the front edge of the paraboloid.

2.3. Positioning and Dimensioning of Diaphragms

In order to compute the effective area for off-axis incidence and the amount of image errors for the telescope a ray-tracing program was developed which permits to follow the radiation incident from an arbitrary direction through the telescope in the manner of geometrical optics, until it is either absorbed by one of the diaphragms in the telescope, or in the detector plane. The latter is not necessarily identical with the focal plane. We have computed the grazing angle on reaching the paraboloid and the hyperboloid and weighted the respective points of incidence with the reflectivities. The program also computes the influence of the diaphragms on the geometrical collector surface. Three diaphragms /11 were required to remove radiation that had not been reflected or had been reflected only once (fig. 3). The diaphragms were designed in such a manner that the geometrical collector area is not impaired out to 20 arcsec off axis. The following Table summarizes the data for the three diaphragms:

	x-position (mm)	Radius (mm)	Radius tolerance (mm)
Diaphragm 1	430	147.5	0.5
Diaphragm 2	-380	107.8	0.5
Diaphragm 3	630	162.6	0.5

The influence of the various diaphragms on the collector surface /12 is shown in Fig. 4 for objects off axis: While the collector area without the diaphragms decreases with increasing off-axis angle so slowly that at 1.5° still half of the area is available, the combination of the three diaphragms limits the field of view for all practical purposes to about 30 arcmin.

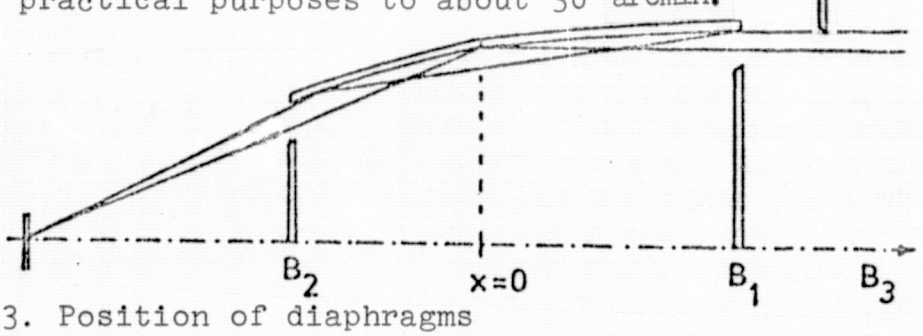

Figure 3. Position of diaphragms

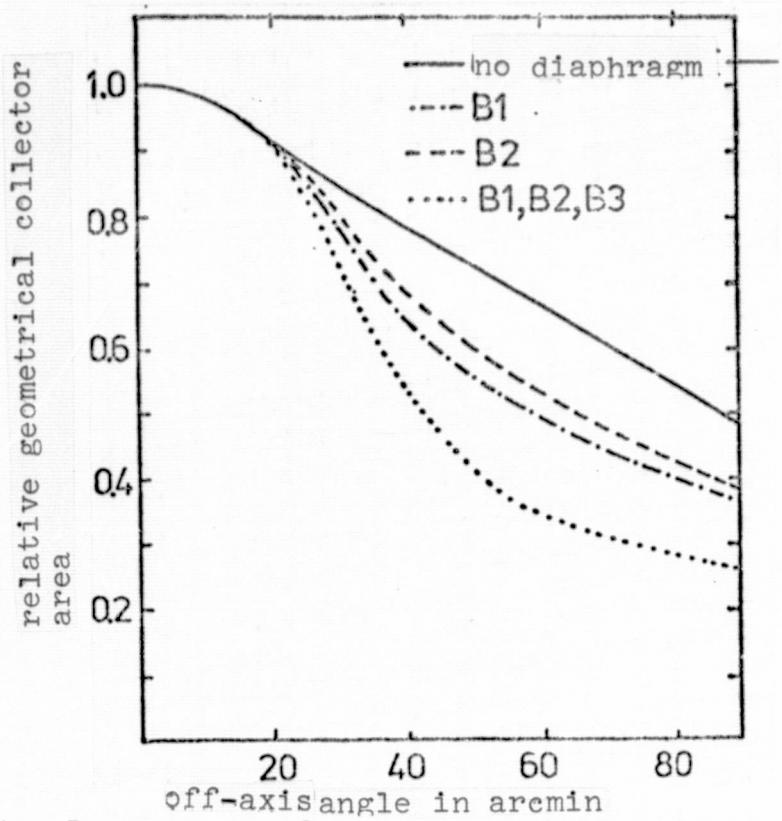

Figure 4. Dependence of the geometrical collector area on the off-axis angle collector area on the off-axis angle for various combinations of diaphragms.

2.4. Design-related image errors

One of the aims of the development of the 32 cm telescope is the discovery and measurement of astrophysical halos, that is, the intensity distribution of X-rays scattered by interstellar dust [40]. In order to measure such dust-scattering halos, the following requirements must be met by the telescope: First, the experimental scattering halo produced by reflection at the telescope mirrors must have an energy flux density below that of the astrophysical halo. In the case of interstellar dust, at 1 keV, an integral scattering contribution of about 30-50% is expected (Cyg X-1, Crab), depending on the grain size and density of the dust. This then places severe requirements on the polishing /13 technology. Second, in order to be able to measure the behavior of the astrophysical halo as a function of the scattering angle, the half width of the point image function of the telescope must

be small with respect to the half width of the astrophysical scattering halo. The current discussion favors average grain sizes of the interstellar dust between 0.15µand 0.05 µm. This type of dust results in a scattering halo width of 4 to 10 arcmin. As a consequence, astrophysical halos can only be measured with the aid of telescopes whose resolution is clearly better than 4 arcmin. For the 32 cm telescope an on-axis point image resolution of 20 arcsec is aimed at.

We shall compute in this section the theoretical resolution of the 32 cm telescope as a function of the off-axis angle; this yields the requirements for the polishing accuracy. We shall also investigate possibilities to test the on-axis resolution optically.

Aside from the violation of the sine condition and the resulting coma, the Wolter telescope has all known image errors of the third order [50, 21]; the construction of strictly aplanar X-ray telescopes is discussed in [52]. An improvement of the resolution was obtained by W. Werner [49] by means of representing the mirror surface by a polynomial. The 32 cm telescope is strictly a Wolter Type I telescope. L. P. Van Spreybroeck and R. C. Chace have published [39] approximate formulas for the resolution (rms blur circle) of such a paraboloid - hyperboloid system:

$$\sigma_p = \frac{1}{5} \cdot \frac{\varepsilon^2}{\alpha} \left(\frac{L_p}{f} \right) + 4 \varepsilon \alpha^2$$

(2)/14

Here, σ_p is the rms radius of the point image function in the case of optimum curvature of the detector surface, ε is the off-axis angle, f the focal length of the telescope, that is the distance of the focal plane from the joining surface. α and L_p, respectively, are as before the grazing angle and the length of the paraboloid. This empirical formula describes the off-axis behavior of the point resolution for a curved detector surface. However, there is currently no spatially resolving X-ray detec-

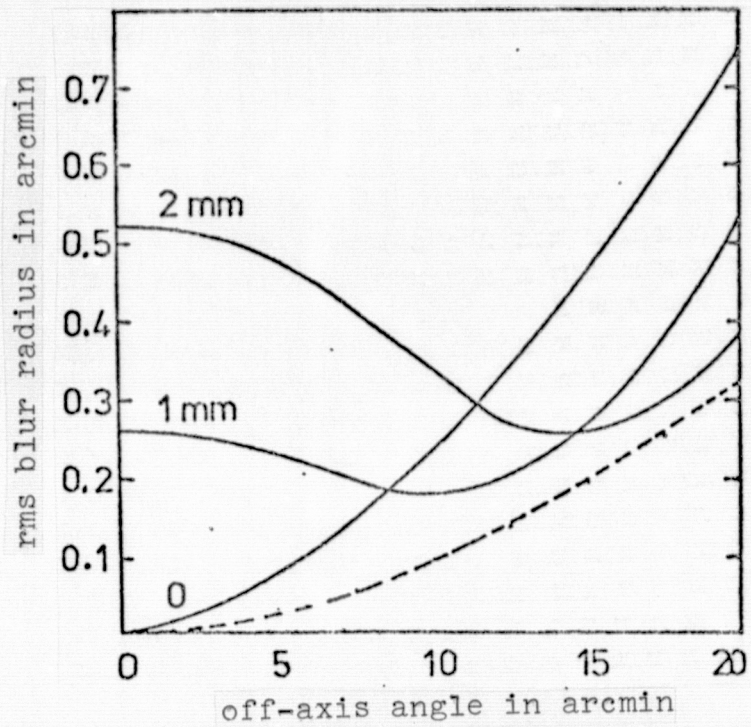

Figure 5. Resolution of the 32 cm telescope as a function of the off-axis angle. Dashed curve: approximation according to Van Spreybroeck.

tor with a curved sensitive surface available. Thus, we have computed with the aid of the computer program for ray tracing mentioned in Section 2.3 the behavior of the off-axis resolution for a plane image surface (Figure 5). The parameters "0 mm" to 2 mm" show the distance of the detector plane from the focal /15 point. While the image plane goes through the focus, the rms blur circle depends about quadratically on ε : $\sigma' \approx A\varepsilon + B\varepsilon^2$ with $A = 8.5 10^{-3}$ and $B = 1.45\ 10^{-3}\,\text{arcmin}^{-1}$ The approximation formula by Van Spreybroeck yields for A and B the values: $A' = 2.74\ 10^{-3}$, $B' = 6.69\ 10^{-4}\,\text{arcmin}^{-1}$. The resolution may be improved by a curvature of the detector surface($x/\text{mm} = 0.043\ (r/\text{mm})^2$) by typically a factor of 2. This optimum resolution for the 32 cm telescope is shown in Fig. 5 by the dashed curve. If the detector plane is moved toward the telescope, the resolution for large off-axis angles is improved, however, at the expense of

the resolution for the on-axis situation. The dependence of the intensity distribution of the point picture on the off-axis angle and the position of the image plane is shown in Fig. 6. In the case of paraxial incidence, and for displacing the detector plane, the δ-shaped point image function changes into an ever wider ring shape. By contrast, the distribution is even without displacement smeared out for values such as ε = 10 arcsec. If the image plane is moved toward the telescope, the diffraction pattern becomes narrower. The optimum of the resolution is obtained for δ values between 0.5 and 1.0 mm. If the displacement is further increased, the intensity in the center of the diffraction pattern decreases with the result that the point image again is transformed into a ring pattern. As we see from Fig. 7,/17 decreasing the half width does not improve the point image; instead, displacing the image plane results in a disappearance of the wide base of the intensity distribution.

Aside from the theoretical errors of importance for the off-axis behavior of the telescope the manufacturing faults result in a decrease of the resolution even in the case of incidence parallel to the axis. In order to avoid the significant effort requir-/18 ed to test the image errors of the telescope and its individual mirrors in the X-ray range, we try to find out to what extent optical tests allow the determination of image errors, and to what limiting resolution; in this manner we do not expect results with respect to microroughness of the mirrors from optical scattering measurements, since the scattering, as shown in Section 3, depends on λ^{-2}, so that in the optical range only a scattering contribution of about 0.01% is to be expected.

The half width of the point image function is independent of the wavelength so long as the diffraction by the ring aperture of the telescope can be neglected. Thus, we calculate in the following the diffraction by the paraboloid mirror, starting from Helmholtz's integral:

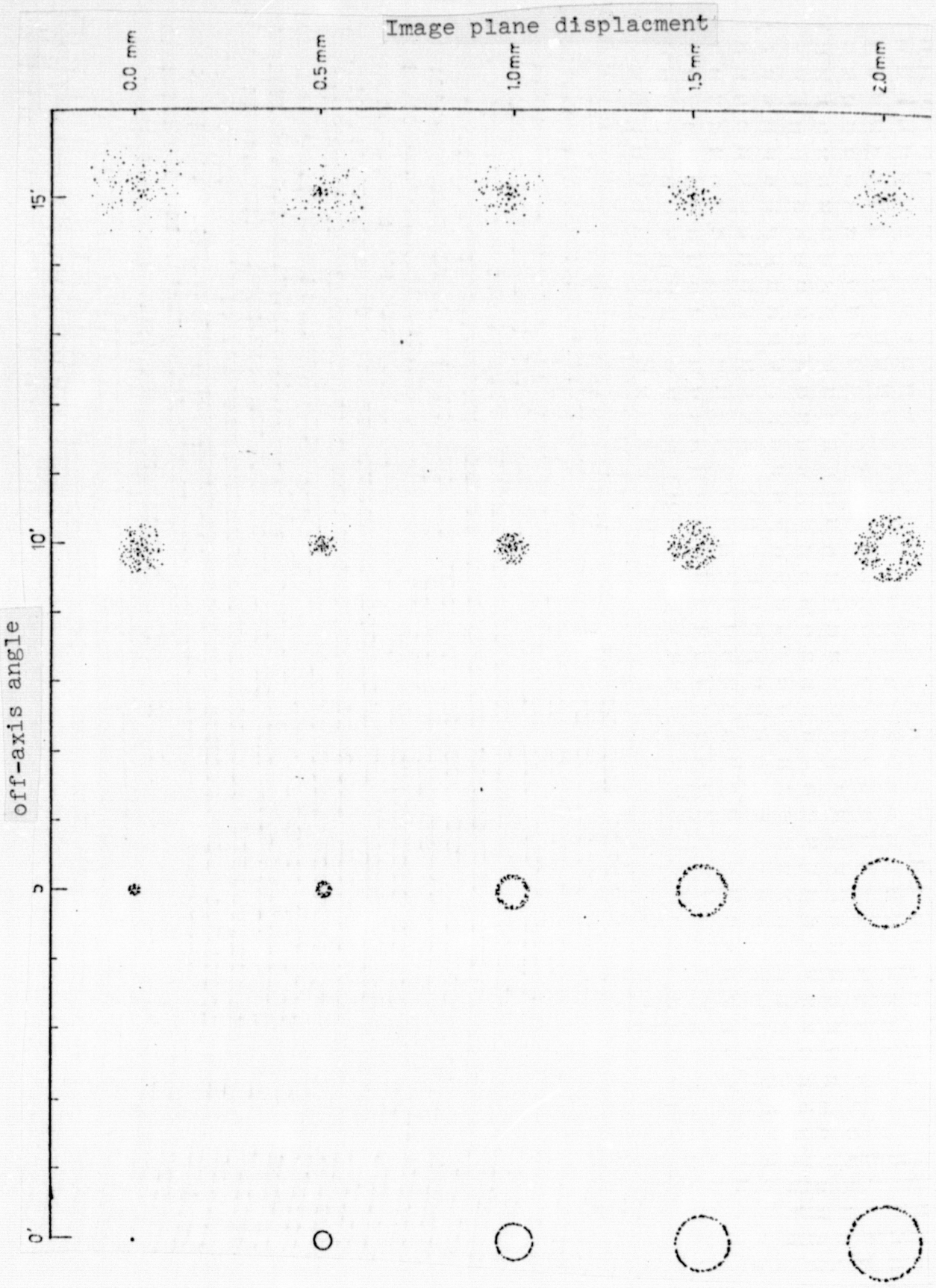

Figure 6. The intensity distribution in the point image as a function of off-axis angle and detector-plane position; geometrical optics approximation.

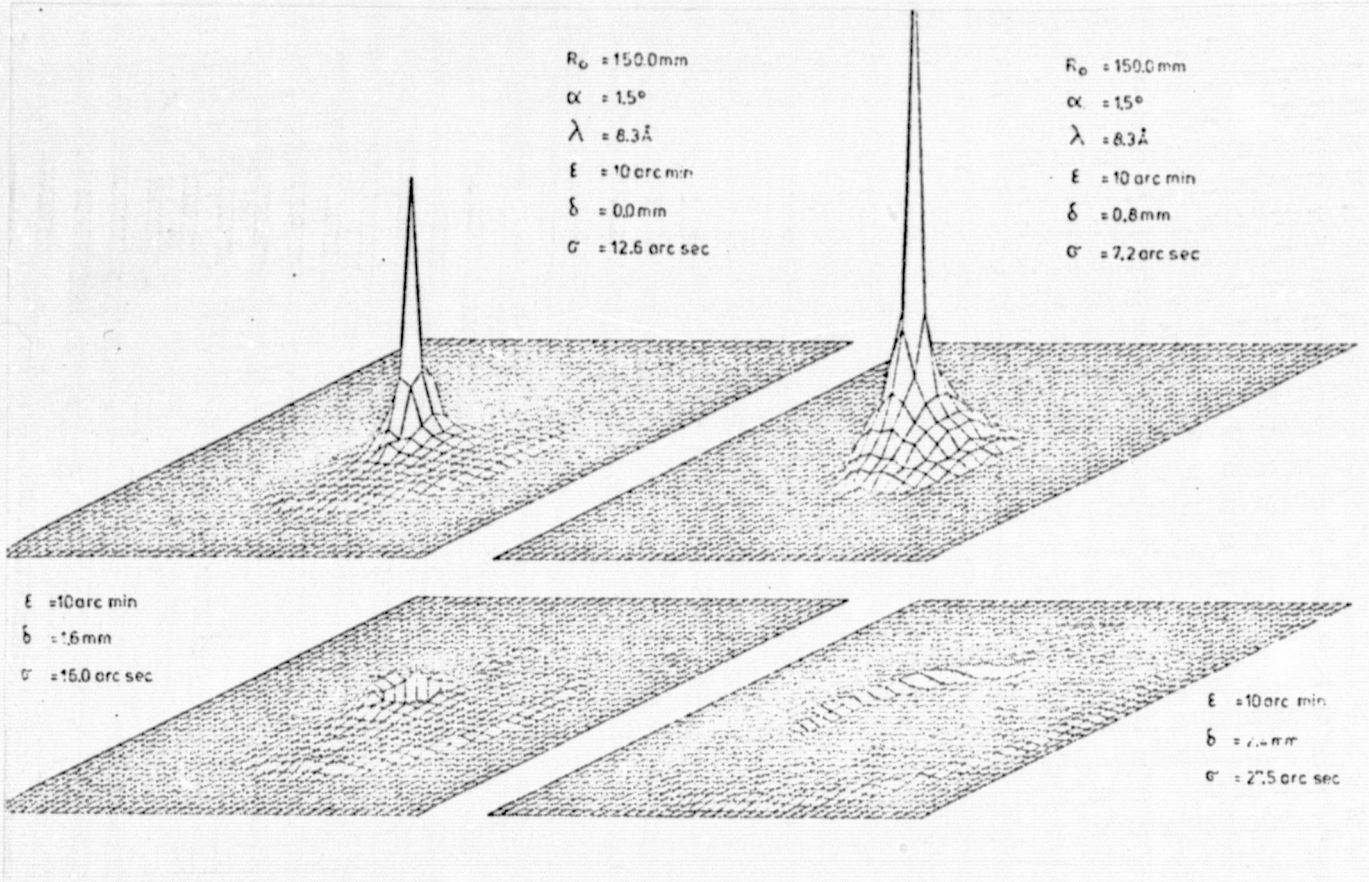

Figure 7. Change of the point image function for an off-axis angle of 10 arcmin as a function of a displacement of the image plane (λ = 13.3 A).

$$U(\rho) = \frac{1}{4\pi}\iint_S \left(E_s \frac{\partial \Psi}{\partial n} - \Psi \frac{\partial E_s}{\partial n} \right) dS \quad \text{mit} \quad \Psi = \frac{e^{i\vec{k}_2 \vec{R}'}}{R'} \tag{3}$$

and the well-known Kirchoff boundary conditions for reflection:

$$E_s = E_1 (1+R) e^{-i\vec{k}_1 \vec{r}} \qquad \frac{\partial E_s}{\partial n} = E_1 (1-R) (\vec{k}_1 \vec{n}) e^{-\vec{k}_1 \vec{r}} \tag{4}$$

Referring to Figure 11, we have $\vec{k}_1$ for the wave vector of the incident wave, $\vec{k}_2$ for that of the reflected wave. $\vec{R}'$ is the vector from the point of reflection to the point of observation, E_1 the amplitude of the electric field of the incident wave. R is Fresnel's reflection coefficient, r the coordinate vector of the point of reflection. Introducing the boundary conditions

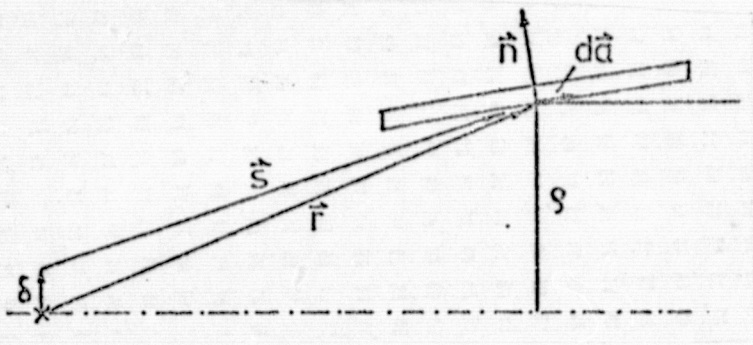

Figure 8. Summary of diffraction at the paraboloid.

[4] into Eq. (3) yields for R = 1:

$$U(p) = \frac{E_1}{2\pi}\iint \frac{e^{ik(s-r)}}{s^2}\left(ik-\frac{1}{s}\right)(\vec{s}\,\vec{n})\,dA \tag{5}$$

If we place the origin of the reference frame into the focal /19 point, then the equation of the paraboloid reads $y^2+z^2=2px+p^2$. Thus,

$$\vec{r}\vec{n} \approx \vec{s}\vec{n} = \frac{x\cdot p + p^2}{\sqrt{2px+2p^2}}$$

and, with $\varsigma = \sqrt{y^2+z^2}$ we have $dA = \sqrt{y^2+z^2}\,d\varphi da = \sqrt{1+\left(\frac{\rho}{\varsigma}\right)^2}\,d\varphi dz$

Neglecting 1/s against k,

$$U(p) = \frac{ikE_1p}{2\pi}\iint \frac{e^{i\vec{k}_1(\vec{s}-\vec{r})}}{r}\,d\varphi\,dx\,.$$

From $s^2-(\vec{s}+\vec{\delta})^2 = -r^2+s^2$ we have $s \approx r-y\delta/r$ with $\vec{\delta} = (o,\delta,o)$

From all this we obtain from Eq. (6)

$$U(p) = ikE_1p\int_{x_1}^{x_2}\frac{J}{r}o\left(\frac{k\varsigma\delta}{r}\right)dx = ikE_1\int_{\varsigma_1}^{\varsigma_2}\frac{\varsigma}{r}J_o\left(\frac{k\varsigma\varsigma}{r}\right)d\varsigma \tag{7}$$

This integral has been numerically evaluated for p = 3.927 and $\lambda = o.5\,\mu$ (Fig. 9). The diffraction pattern is similar to that of a ring diaphragm [45] the first minimum at 3.8μ corresponds to diffraction at a circular aperture with a radius of 16 cm.

Superposed on this function with its high oscillation frequency is another function with a much lower frequency which represents the influence of the ring width of the aperture. If the distance from the axis is chosen as the width of the diffraction pattern such that the amplitude is decreased, on the average (envelope) to e^{-1}, then Fig. 9 shows a width of 10 μm. At a focal width of the paraboloid of 2862.1 mm this corresponds to a diffraction /20 width of 0.7 arcsec. The first minimum of the envelope is at 130 μm or 9 arc sec.

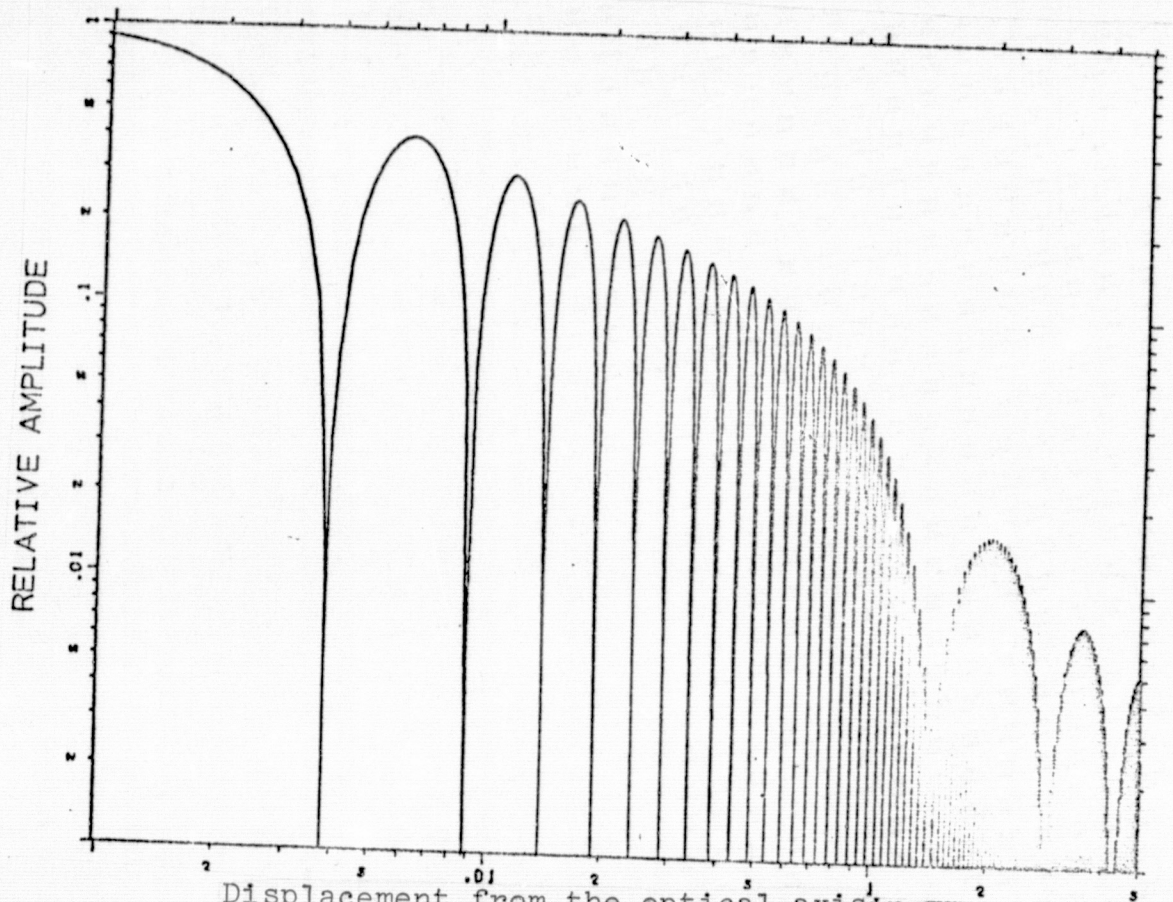

Figure 9. Diffraction pattern of the paraboloid of the 32 cm telescope. $\lambda = 0.5\ \mu$

These calculations show that the required resolution of 20 arcsec can be easily tested by optical means with the 32 cm telescope.

Optical measurements with the prototype of the 32 cm telescope resulted in a FWHM of 5 arcsec which clearly satisfies the /21
resolution of 20 arcsec.

In addition to the image errors of the geometrical-optics type which are due to the type of telescope and manufacturing inaccuracies, the scattering upon reflection deteriorates the point image function. Thus, in the following, we investigate the reflection of X-rays on ideally plane as well as rough boundary layers both theoretically and experimentally.

3. REFLECTION OF X-RAYS: REFLECTIVITY AND SCATTERING

3.1. Survey

If a plane electromagnetic wave is incident on a plane boundary layer between a material body, part of the wave enters a vacuum and a material body, part of the energy enters in the form of a plane wave the second medium, while another portion is reflected in the form of a plane wave. The complex refractive index n des- /22
cribes the optical behavior the material. The reflectivity is obtained from Fresnel's formulas. Section 3.2 treats the reflection problem at an ideal boundary surface for "normal" material as well as for a highly magnetized plasma of high density (neutron star surface). By contrast, if the boundary layer is not an ideal plane, but rough in some manner, then both the wave front of the reflected and of the refracted wave are perturbed, and the two waves are not any longer plane. Energy is scattered into angles outside of the specular direction and even outside of the plane of incidence. So long as the situation can be described by means of geometrical optics, the scattering is independent of the size of the roughness-causing agent (Section 3.3). If the problem is treated in the framework of Fresnel optics, then the scattering /23
behavior (in the far field) is constant, if the ratio of the wavelength and the roughness is constant (Section 3.4).

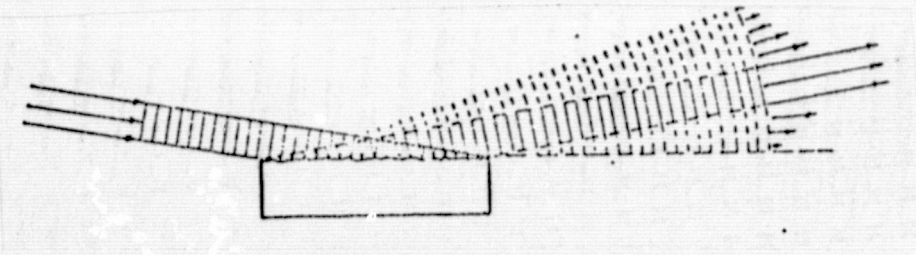

Figure 10. Schematics of reflection at a rough surface.

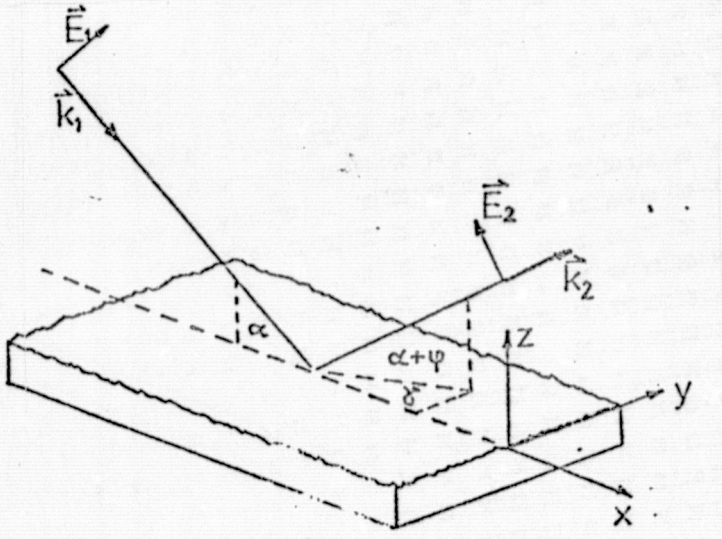

Figure 11. The choice of a reference frame and the definition of angles.

The wave vector $\vec{k}_1$ and the electric field vector $\vec{E}_1$ describe the incident wave. A Cartesian coordinate system is defined in such a manner that the xz-plane coincides with the plane of incidence. The xy-plane is the major plane of the mirror, that is, if h(x,y) describes the surface, then

$$\iint_F h(x,y)\,dxdy = \langle h \rangle = 0$$

where α is the angle of incidence, γ the angle between the plane

of incidence and the plane in which the outgoing wave is situated. $\alpha+\varphi$ is then the angle in this plane for this outgoing wave. However, for the time being we assume $\varphi = \gamma = 0$, that is, we consider reflection at an ideal surface, and we neglect the diffraction at the edges of the mirror.

3.2. Reflection Theory

a) Reflection by matter under normal conditions

Outside of absorption edges, the refractive index in the energy range of soft X rays is determined by the plasma frequency

$$\omega_p = \sqrt{\frac{4\pi e^2}{m_e} n_e}$$

with

$$n = \sqrt{1-\left(\frac{\omega_p}{\omega}\right)^2}$$

For matter under normal conditions we have for the electron density $n_e \approx 10^{24}/cm^3$, resulting in a plasma frequency $\omega_p \approx 5\times10^{16}/sec$ and the corresponding quantum energy $\hbar\omega_p \approx 30$ eV . The energy of the X-rays is large compared to that energy. This means that/24

$$n \approx 1 - \frac{1}{2}\left(\frac{\omega_p}{\omega}\right)^2 \Rightarrow 2\delta \approx \left(\frac{\omega_p}{\omega}\right)^2 \Rightarrow \alpha_c \approx \frac{\omega_p}{\omega}$$

Total reflection occurs for $\alpha \leq \frac{\omega_p}{\omega}$. A quantitative study must take into account the shell structure of atoms: The simplest approximation is provided by the Kramers-Kallman-Mark theory of anomal dispersion which results for δ in

$$\delta = 2.7\times10^{10}\left(\frac{\rho}{M}\right)\lambda^2\left[Z - \sum_q g_q\left(\frac{\lambda}{\lambda_q}\right)^2 \log\left|\frac{\lambda^2-\lambda_q^2}{\lambda^2}\right|\right]$$

Here, M is the molecular weight, Z the nuclear charge, λ_q and g_q wavelength and oscillator strength of the energy level q, respectively. All quantities are given in cgs units [10]. The following

two tables contain the optical constants; they will be used for comparison with measurements with gold and nickel (B. Aschenbach, personal communication).

Gold $n = 1 - \delta - i\beta$				Nickel		
λ	δ	β	α_c	δ	β	α_c
5.4	$1.4\ 10^{-4}$	$1.1\ 10^{-4}$	0.96°	$3.6\ 10^{-4}$	$8.6\ 10^{-5}$	1.54°
8.3	$9.0\ 10^{-4}$	$2.2\ 10^{-4}$	2.43°	$7.8\ 10^{-4}$	$3.4\ 10^{-4}$	2.26°
9.9	$1.2\ 10^{-3}$	$3.4\ 10^{-4}$	2.80°			
13.3	$2.4\ 10^{-3}$	$1.1\ 10^{-3}$	3.96°	$9.3\ 10^{-4}$	$1.5\ 10^{-3}$	2.47°
17.6	$3.7\ 10^{-3}$	$2.4\ 10^{-3}$	4.92°	$1.8\ 10^{-3}$	$5.9\ 10^{-3}$	3.43°
44.8	$2.1\ 10^{-2}$	$9.9\ 10^{-3}$	11.61°	$1.5\ 10^{-2}$	$1.5\ 10^{-2}$	9.83°

If the complex refractive index is known, then the reflectivity is obtained from Fresnel's formulas to read

$$\frac{E_{2\parallel}}{E_{1\parallel}} = \frac{n\cdot\sin\alpha - \sin\zeta}{n\cdot\sin\alpha + \sin\zeta} \qquad \frac{E_{2\perp}}{E_{1\perp}} = \frac{\sin\alpha - n\cdot\sin\zeta}{\sin\alpha + n\cdot\sin\zeta}$$

where $\sin\zeta = \frac{1}{n}\sqrt{n^2 - \cos^2\alpha}$

If the radiation is not polarized, so that $|E_{1\parallel}| = |E_{1\perp}|$, then/25 we have for the reflectivity

$$R = \frac{I}{I_0} = \frac{1}{2}\left[\frac{|E_{2\parallel}|^2}{|E_{1\parallel}|^2} + \frac{|E_{2\perp}|^2}{|E_{1\perp}|^2}\right] \qquad (8)$$

and with $\alpha \approx \sin\alpha$, $\zeta \approx \sin\zeta$, $\delta \ll 1$, $\beta = 0$

$$R = \begin{cases} 1 & \text{for} \quad \alpha \leq \alpha_c \\ \dfrac{1-\sqrt{1-(\alpha_c/\alpha)^2}}{1+\sqrt{1-(\alpha_c/\alpha)^2}} & \text{for} \quad \alpha > \alpha_c \end{cases}$$

The reflectivity is constant up to $\alpha = \alpha_c$ (unity); then it suddenly decreases (half width: $(\frac{3\sqrt{2}}{4} - 1)\cdot\alpha_c$)) with increasing grazing angle. In the case of $\beta \neq 0$ the intensity decreases even

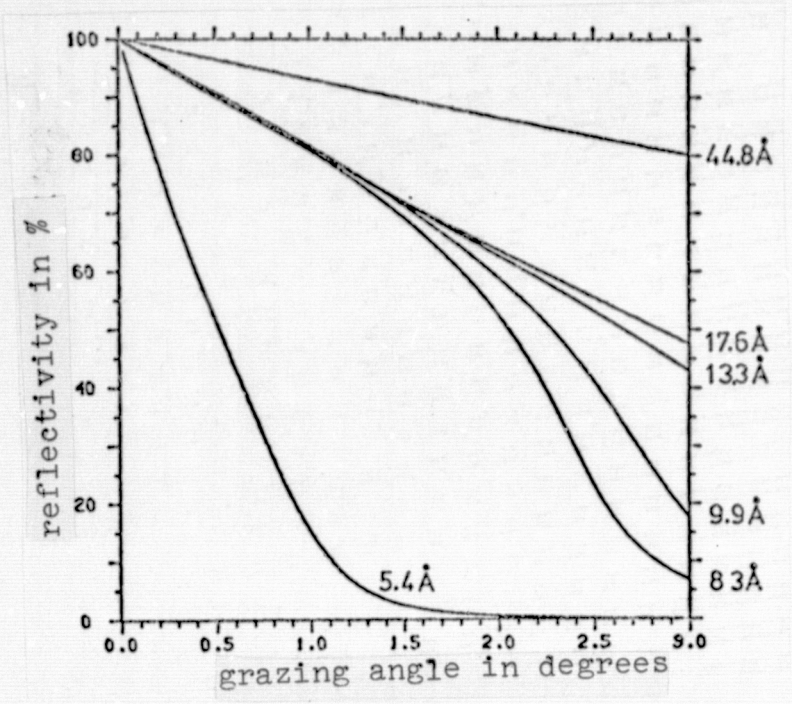

Figure 12. Dependence of the reflectivity on the grazing angle and the wavelength in the case of gold.

before the critical angle α_c is reached; nevertheless, the grazing angle is still a measure for the width of the reflectivity curve. Fig. 12 shows for the optical constants of the above table the corresponding reflectivity curves. For $\alpha = \alpha_c$ we have the /26 reflectivity

$$R = \frac{2\delta + 2\beta - 2\sqrt{2\delta\beta}}{2\delta + 2\beta + 2\sqrt{2\delta\beta}}$$

Since β is of the order δ in the case of soft X-rays, we have the following rule of thumb: The reflectivity for $\alpha = \alpha_c$ amounts to about 20%. In Section 4.9 we shall compare these theoretical curves with measured values. Right now, we would like to take a little detour into astrophysics.

b. Reflection by the surface of a neutron star

While in the case of solids on earth the electron density is

of the order 10^{24} cm^{-3}, the current models [33, 17] of the surface of neutron stars lead to values of order $10^{28} cm^{-3}$. The plasma frequency , the frequency of free electron oscillations, is therefore higher by a factor of about 100, if compared with material under normal conditions. External total reflection should occur for 1 keV radiation until nearly perpendicular incidence, and it should occur at grazing angles of 1 to 2° for radiation up to 100 keV. There is a second difference in the reflection behavior of the surface of a neutron star by comparison with normal conditions: Neutron stars have high magnetic fields (order 10^{12} Gauss). This makes the electron plasma anisotropic so that the electrons are free to move in the direction of the magnetic field, while their motion perpendicular to the field is quantized. Thus, the medium is birefringent, and the refractive index depends on direction.

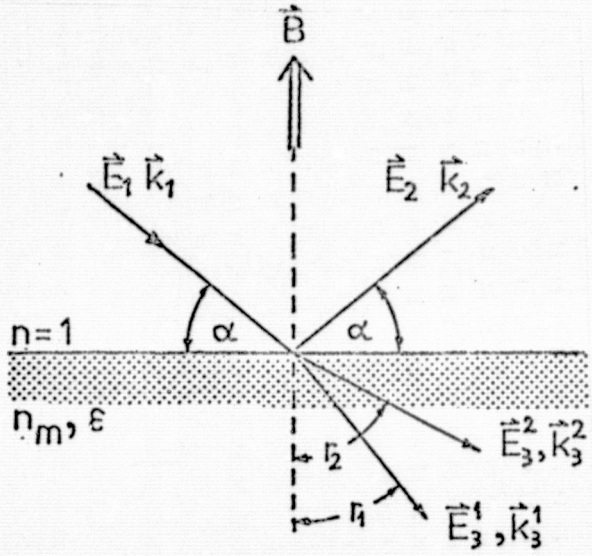

Figure 13. Reflection at the surface of a neutron star.

The electron density at the surface of a neutron star [17] is

$$n_e = 1.2 \times 10^{27} \; Z_{26}^{2/5} \; B_{12}^{6/5} \; cm^{-3} \qquad /27$$

If the surface consists of iron, then the plasma frequency yields $\hbar\omega_p = 1.45 \; B_{12}^{3/5}$ (KeV) while the cyclotron frequency is $\omega_B \hbar = \frac{eB}{m_e c} \hbar = 11.6 \; B_{12}$ (KeV) . The binding energies of the elec-

trons are negligible, since most have energies below 2 keV (W. Hillebrandt, private comm.).

We restrict in the following our considerations to the neighborhood of the magnetic poles of the neutron star. This leads to /28 the situation depicted in Fig. 13. The dependence of the electrical field strengths $\vec{E}_2$ and $\vec{E}_3^1, \vec{E}_3^2$ on $\vec{E}_1$, $\vec{k}_1$ and the grazing angle 4 is obtained from the continuity conditions for the electric field at the surface and the refractive indices n_1 and n_2 which in turn depend on the refraction angles r_1 and r_2. We neglect the effects of birefrigency that appear at high field strengths in the vacuum [31], since the departure of n from unity is only 10^{-5}. We place the xy-plane into the surface of the star. Then, the dispersion relationship for the electron plasma reads

$$\begin{bmatrix} S - n_m\cos^2 r_m & -iD & -n_m^2 \sin r_m \cos r_m \\ iD & S - n_m & 0 \\ -n_m^2 \sin r_m \cos r_m & 0 & P - n_m^2 \sin^2 r_m \end{bmatrix} \cdot \begin{bmatrix} E_{3x}^m \\ E_{3y}^m \\ E_{3z}^m \end{bmatrix} = 0 \qquad (10)$$

with

$$\begin{aligned} R &= 1 - \left(\frac{\omega_p}{\omega}\right)^2 \frac{\omega}{\omega - \omega_B + i\omega_p} \\ L &= 1 - \left(\frac{\omega_p}{\omega}\right)^2 \frac{\omega}{\omega + \omega_B + i\omega_p} \\ P &= 1 - \left(\frac{\omega_p}{\omega}\right)^2 \frac{\omega}{\omega + i\omega_p} \\ S &= \frac{R+L}{2} \\ D &= \frac{R-L}{2} \end{aligned} \qquad (11)$$

(See, for instance, reference [41]). ω_p is a collision frequency or some general damping frequency. m = 1 and 2, respectively, describe the ordinary and the extraordinary mode of propagation. This dispersion relation yields the amplitude ratios:

$$\frac{E_{3x}^m}{E_{3z}^m} = \frac{P - n_m^2 \sin r_m^2}{n_m^2 \sin r_m \cos r_m} \doteq \alpha_m \qquad (12)$$

$$\frac{E_{3y}^m}{E_{3z}^m} = \frac{-iD\alpha_m}{S - n_m} \doteq \beta_m$$

Since the determinant in Eq. (10) must vanish, we have

$$
\begin{aligned}
&A\cdot(n^m)^4 - B(n^m)^2 + C = o \text{ mit:}\\
&A = S\sin^2 r_m + P\cos^2 r_m\\
&B = RL\sin^2 r_m + PS(1+\cos^2 r_m)\\
&C = PRL
\end{aligned}
\tag{13}
$$

Snell's law is valid for both modes of propagation, that is, $n_m = \frac{\cos\alpha}{\sin r_m}$ where n_m depends explicitly on r_m. The determination of the electrical field components requires, in addition, the boundary conditions for $\vec{E}$, $\vec{D}$, $\vec{B}$ and $\vec{n}$ at the surface

$$
\begin{aligned}
&\left[\vec{E}_1 + \vec{E}_2 - \hat{\varepsilon}\sum_{m=1}^{2}\vec{E}_3^m\right]\vec{z}_o = o\\
&\left[\vec{k}_1\times\vec{E}_1 + \vec{k}_2\times\vec{E}_2 - \sum_{m=1}^{2}\vec{k}_3^m\times\vec{E}_3^m\right]\cdot\vec{z}_o = o\\
&\left[\vec{E}_1 + \vec{E}_2 - \sum_{m=1}^{2}\vec{E}_3^m\right]\times\vec{z}_o = o\\
&\left[\vec{k}_1\times\vec{E}_1 + \vec{k}_2\times\vec{E}_2 - \sum_{m=1}^{2}\vec{k}_3^m\times\vec{E}_3^m\right]\times\vec{z}_o = o
\end{aligned}
\tag{14}
$$

where $\vec{z}_o$ is the unit vector in the direction normal to the surface. Introducing Eqs. (12) into (14) we find

$$
\begin{bmatrix} E_{1\perp} \\ E_{1\parallel} \\ E_{1\perp} \\ E_{1\parallel} \end{bmatrix} = \begin{bmatrix} \beta_1 & \beta_2 & -1 & o \\ \frac{n^1\cos r_1\beta_1}{\sin\alpha} & \frac{n^2\cos r_2\beta_2}{\sin\alpha} & 1 & o \\ \frac{\alpha_1}{\sin\alpha} & \frac{\alpha_2}{\sin\alpha} & o & 1 \\ \frac{\rho}{\cos\alpha} & \frac{\rho}{\cos\alpha} & o & -1 \end{bmatrix} \begin{bmatrix} E_{31}^1 \\ E_{32}^2 \\ E_{2\perp} \\ E_{2\parallel} \end{bmatrix}
\tag{15}
$$

We were able to split $\vec{E}_1$ and $\vec{E}_2$ into the transverse components parallel and perpendicular to the plane of incidence; $\vec{E}_3$, however, has also a component in the longitudinal direction. Inverting the matrix yields the dependence of the field strengths $\vec{E}_2$ and $\vec{E}_3^m$ on $\vec{E}_1$, α and ω.. The corresponding reflectivities

$$R_{\parallel} = \frac{|\vec{E}_{2\parallel}|^2}{|\vec{E}_{1\parallel}|^2} \quad \text{and} \quad R_{\perp} = \frac{|\vec{E}_{2\perp}|^2}{|\vec{E}_{1\perp}|^2}$$

as a function of the photon energy are shown in Figs. 14 to 16, taking the following values of ω_p, ω_e and ω_D: $\hbar\omega_p$ = 4 KeV, $\hbar\omega_B$ = 58 KeV, $\hbar\omega_D$ = 0.1 KeV. . These values for ω_p and ω_B are /31 obtained for a magnetic field of 5×10^{12} Gauss as is was measured spectroscopically in the case of Her X-1 [44]. The value ω_D for the damping frequency is an upper limit, estimated in reference [47].

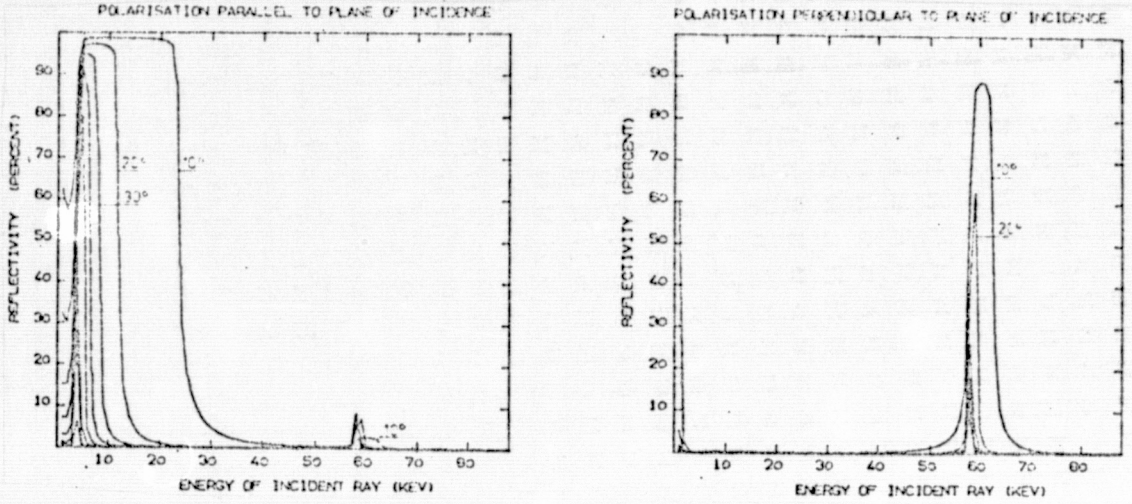

Figure 14. Reflectivity as a function of the photon energy.

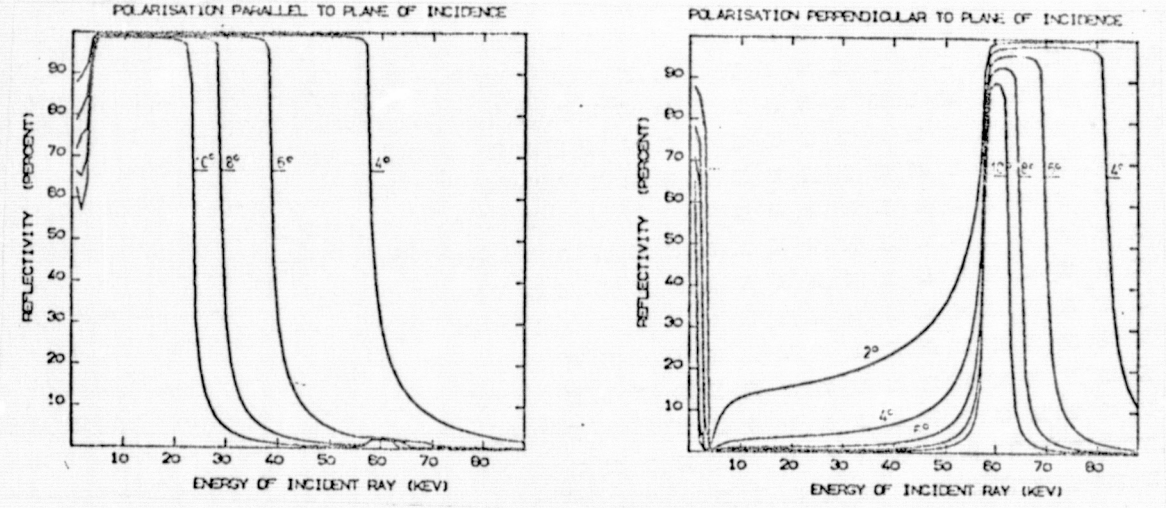

Figure 15. Reflectivity as a function of photon energy.

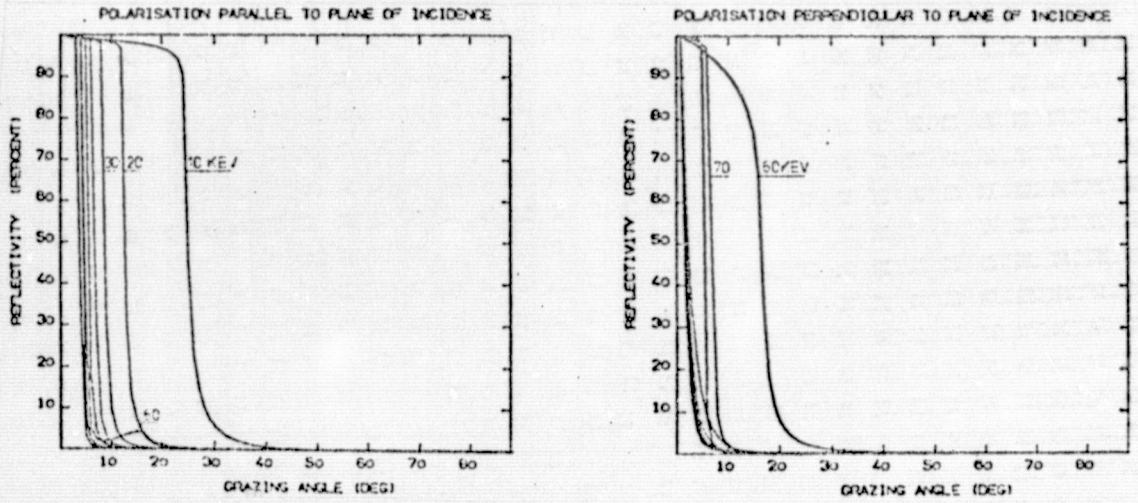

Figure 16. Reflectivity as a function of grazing angle.

Figs. 14 and 15 show that for X-ray radiation that is polarized parallel to the plane of incidence the reflectivity is close to unity up to a cut-off energy which depends on the grazing angle. In the case of polarization perpendicular to the plane of incidence we find total reflection above the cyclotron frequency. Again, the width of the energy band for which we have total reflection depends on the grazing angle. If the grazing angle is small, the reflectivity increases markedly between plasma and cyclotron frequency for this mode of polarization.

If we plot the reflectivity vs. grazing angle with the photon energy as parameter (Fig. 16), then we find the typical behavior of total reflection: For $\alpha \approx 0$ the reflectivity tends to unity. If the grazing angle is increased, the reflectivity slowly decreases and then, at a critical angle $\alpha_c = \cos^{-1}\left(\sqrt{1 - \left(\frac{\omega_p}{\omega}\right)^2}\right)$ rapidly goes to zero. This behavior in the case of polarization parallel to the plane of incidence corresponds to total reflection in the case of normal material with little absorption β . In the case /32 that the polarization is perpendicular to the plane of incidence, this analogy is not valid, since here the grazing angle for total reflection at 60 keV is larger than for 10 keV due to the fact that

total reflection starts above the cyclotron frequency.

The results of Section 3.2b have been published in reference 24.

3.3. Scattering Models

According to the Rayleigh criterion a mirror may be considered ideal if $\frac{4\pi \sin\alpha \cdot \sigma}{\lambda} \ll 1$ where σ represents the mean departure from the ideal plane: $\sigma^2 = \langle h^2 \rangle$. If $\sigma = 50$ Å, $\alpha = 1^\circ$, and $\lambda = 10$ Å, the ratio on the lhs is just equal to 1. The Rayleigh criterion is not really satisfied in the X-ray range, except for very small grazing angles (less or about 1 arcmin). Thus, we shall discuss in the following the theory of scattering under reflection.

The first type of theory, known as Lambert's Law, which /33
treats the angular distribution of scattered electromagnetic radiation assumes that the radiation is so often scattered at the surface or in the interior of the mirror that it has "forgotten" where it came from. The outgoing direction is then random, and the energy flux produced by a surface element is proportional to the cosine of the outgoing angle and independent of the angle of incidence: $I \propto \cos\theta_2$. If ds is a surface element that is normal to the outgoing direction, then the energy flux per ds is constant. There are very few scattering materials which satisfy this law even to some approximation, and for grazing incidence Lambert's Law is never fulfilled.

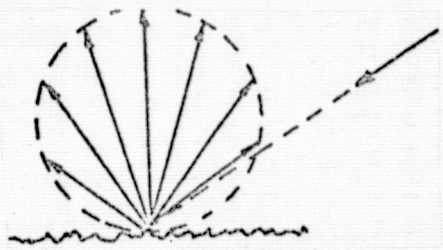

Figure 17a. Scattering according to Lambert.

The first theory that allowed to explain the departures found in experiment from Lambert's Law while still taking only single scatterings into account is due to Bouguer [7,8]. The surface is described as an assembly of small bevels each of which reflects as an ideal mirror. The directions of the bevels are randomly oriented (for instance, according to a normal distribution) with the result that the scattered radiation, too, shows a random distribution. Diffraction and the edges of the bevels are neglected. A similar model has been described by T. S. Trowbridge and K.P. /34
Reitz [43]. However, in this case not only the bevel directions have a normal distribution, but also their radii of curvature. Since a curved surface can be approximated by plane bevels, the results of this theory can be compared with those of a plane-bevel theory.

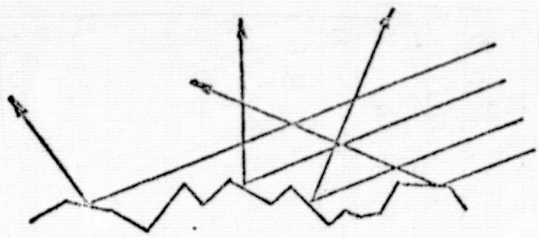

Figure 17b. Bevel model.

These theories on the basis of geometrical optics have the advantage of being simple; even shadowing effects and multiple scattering can be included without much difficulty. Agreement with experiment, however, can only be expected, if the surface can actually be described by bevels that are large by comparison with the ratio of wavelength and grazing angle $\frac{\lambda}{\alpha}$ and if the relation $\frac{4\pi\sigma \sin\alpha}{\lambda} \gg 1$ is valid.

Interesting is the attempt by V. Twersky [46] who treats the reflection by rough surface on the basis of diffraction optics. The model describes the mirror surface as an ideal surface which

is subject to defects by individual scattering centers (for instance, of hemispheric form). The scattering by such a surface can be treated in the framework of diffraction optics. The remarkable feature of this theory, however, is the possibility to treat the influence of polarization: If the radii of the scattering centers, a, are small, then the radiation is proportional to $(\frac{a}{\lambda})^4$ and $(\frac{a}{\lambda})^2$ for horizontal and vertical polarization, respectively. If, on the other hand, the surface shows large unevenness, the corresponding dependencies read $(\frac{a}{\lambda})^2$ and $o(\frac{\lambda}{b})$. However, since it is assumed that the distance of the scattering centers from each other is large by comparison with their radii, this type of surface is not very similar to the roughness of polished surfaces. A better approach in this case is the description by means of a statistical model which will be developed in the following.

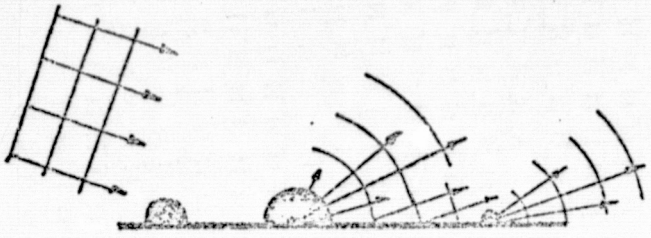

Figure 17c. Scattering model according to Twersky.

3.4. Scattering theory for statistically rough surfaces

H. Davis [12] published in 1953 a treatment of rough surfaces which contains the basic features of a scattering theory for statistically rough surfaces. The surface is described by means of /36 two statistical functions, namely, the height distribution w(z) and the autocorrelation function $c(\tau)$: Let h(x,y) be the surface in the reference frame of Section 3.1. We then have for the autocorrelation function

$$c(\tau) = \frac{\langle h(x_1,y_1)\cdot h(x_2,y_2)\rangle}{\langle h^2(x_1,y_1)\rangle} \quad \text{with} \quad \tau = \sqrt{(x_1-x_2)^2+(y_1-y_2)^2} \qquad (16)$$

where here and in what follows the symbol $\langle\ \rangle$ represents averaging over the mirror surface. The function w(z) is the probability that there is a height z on the surface. The transition from the geometrical-optics case ($\sigma \gg \frac{\lambda}{\alpha}$) to the case of diffraction optics ($\sigma \ll \frac{\lambda}{\alpha}$) is not discussed in this paper, and the scattering probability is only stated in the above two extreme cases. P. Beckmann [1] describes the continuous transition between the two cases. We follow in our treatment his basic assumptions and terminology.

If an electromagnetic wave hits a boundary layer h(x,y), then the amplitude of the electrical field strength at the surface equals the sum of the amplitudes of incoming and outgoing wave, that is, $(E)_s = (1+R_F)E_1$, where R_F is Fresnel's reflection coefficient; the latter allows to introduce a phase jump where necessary. The change of amplitude in the direction of the normal direction to the surface reads $\left(\frac{\partial E}{\partial \vec{n}}\right)_s = E_1(1-R_F)(\vec{k}_1\vec{n})$. This formula is Kirchhoff's approximation for the boundary conditions in the case of reflection. If we make use of these boundary conditions we implicitly assume that the surface is sufficiently smooth: The radius of curvature of uneven points is large with respect to the wavelength, shadowing effects and multiple scattering events are neglected. On the basis of this set of boundary conditions we solve Helmholtz's in- /37
tegral [3] with

$$\Psi = \frac{e^{i\vec{k}_2(\vec{r}_0 - r)}}{r_0}$$

(see Figure 17d). By replacement we have:

$$E_2 = \frac{ie^{ikr_0}}{4\pi r_0}\iint_c (R_F\vec{v}-\vec{p})\vec{n}e^{i\vec{v}\vec{r}}dS \quad \text{with} \quad \vec{p}=\vec{k}_1+\vec{k}_2,\ \vec{v}=\vec{k}_1-\vec{k}_2.$$

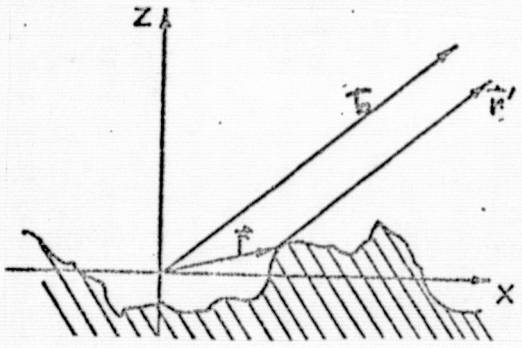

Figure 17d. Statistical model

If we neglect the correlation between R_F and $h(x,y)$ and the derivatives of this function with respect to x and y, then we can write for the expectation value of $|E_2|^2$:

$$\langle |E_2(R_F(h'), \alpha, \frac{\sigma}{\lambda})|^2 \rangle \approx \langle |R_F|^2 \rangle \langle |E_2(R_F=1, \alpha, \frac{\sigma}{\lambda})|^2 \rangle$$

Here, $\langle |R_F|^2 \rangle \approx R(\alpha)$, where R is the reflectivity (see Section 3.21).

Thus, without restriction to generality, we can set R = 1 and find from Eq. (17)

$$E_2 = \frac{ik\, e^{ikr_0}}{2\pi r_0} \int_{-X}^{X}\int_{-Y}^{Y} \left(a \frac{\partial h}{\partial x} + c \frac{\partial h}{\partial y} - b \right) e^{i\vec{v}\vec{r}}\, dx\, dy$$

where

$$a = 2\cos(\alpha+\varphi)\cos\gamma$$

$$b = 2\sin(\alpha+\varphi)$$

$$c = 2\cos(\alpha+\varphi)\sin\gamma$$

Partial integration results in

$$E_2 = \frac{-ik\, e^{ikr_0 \sin\alpha}}{2\pi r_0} F(\alpha,\varphi,\gamma) \int_{-X}^{X}\int_{-Y}^{Y} e^{i\vec{v}\vec{r}}\, dx\, dy$$

where

$$F(\alpha,\varphi,\gamma) = \frac{1 + \sin\alpha \sin(\alpha+\varphi) - \cos\alpha \cos(\alpha+\varphi)\cos\gamma}{\sin\alpha\,(\sin\alpha + \sin(\alpha+\varphi))}$$

For small grazing angles we have $\sin\alpha = \alpha$, $\sin(\alpha+\varphi) = \alpha+\varphi$, and

/38

$$F(\alpha,\varphi,\gamma) = 1 + \frac{\varphi}{2\alpha} - \frac{\gamma^2}{4\alpha^2 + 2\varphi\alpha} \qquad (20)$$

In addition, the integral [19] disappears already for very small angles γ, and we can write with good accuracy

$$F(\alpha,\varphi,\gamma) = F(\alpha,\varphi) = 1 + \frac{\varphi}{2\alpha} \qquad (21)$$

Comparing the result of Eq. (19) with that obtained from [16], that is $E_{20} = E_2(h=0)$ we have

$$\varsigma \doteq \frac{E_2}{E_{20}} = \frac{F(\alpha,\varphi)}{A}\int_{-X}^{X}\int_{-Y}^{Y} e^{i\vec{\nu}\vec{r}}\,dx\,dy \quad \text{with} \quad A = 4XY. \tag{22}$$

In the case of a statistically rough surface we are interested in the average of the square of the absolute value of ς:

$$\langle|\varsigma|^2\rangle = \frac{F^2}{A^2}\,\frac{\langle\exp(i\nu_z\cdot(h(x_1,y_1)-h(x_2,y_2)))\rangle}{\int_{-X}^{X}\int_{-X}^{X}\int_{-Y}^{Y}\int_{-Y}^{Y}\exp(i\nu_x(x_1-x_2)+i\nu_y(y_1-y_2))\,dx_1\,dx_2\,dy_1\,dy_2} \tag{23}$$

while the square of the absolute value of the average of ς reads:

$$\begin{aligned}|\langle\varsigma\rangle|^2 &= \frac{F^2}{A^2}\left|\langle\exp(i\nu_z\,h(x,y))\rangle\int_{-X}^{X}\int_{-Y}^{Y}\exp(i\nu_x x + i\nu_y y)\,dx\,dy\right|^2 \\ &= \frac{F^2}{A}\,\mathrm{sinc}^2(\nu_x X)\,\mathrm{sinc}^2(\nu_y Y)\cdot\left|\langle\exp(i\nu_z z)\rangle\right|^2.\end{aligned} \tag{24}$$

Since

$$\langle|\varsigma|\rangle = |\langle\varsigma\rangle|^2 + D(\varsigma) \quad \text{with} \quad D(\varsigma) = \langle|\varsigma - \langle\varsigma\rangle|^2\rangle \tag{25}$$

we find that Eq. (24) represents the specularly reflected contribution to Eq. (23). In order to further develop the theory from Eqs. (23) and (24), we need assumptions as to the form of the surface. First we assume that h(x,y) follows a normal distribution:

$$w(z) = \frac{1}{\sigma\sqrt{2\pi}}\,e^{-\frac{z^2}{2\sigma^2}}$$

This assumption is reasonable as is shown by many direct measurements of the roughness of surfaces; c.f., for instance, reference [3]. An additional argument is the agreement of the results obtain-/39
ed on the basis of the assumption with the measurements discussed in Section 4.3. The simple assumption of normal distribution allows already to derive an important result from Eq. (24): The expectation value in Eq. (24) reads in the case of a normal distribution:

$$\langle\exp(i\nu_z z)\rangle = \frac{1}{\sigma\sqrt{2\pi}}\int_{-\infty}^{\infty}\exp\left(i\nu_z z - \frac{z^2}{2\sigma^2}\right)dz = e^{-\frac{g}{2}}$$

where $g = \sigma^2 v_z^2$. Since F is unity in the specular direction, we find that in the case of a rough surface the contribution I_{sp} which is reflected specularly is decreased by a factor $e^{-(2k\sin\alpha\cdot\sigma)^2} = e^{-g_o}$ by comparison with an ideal mirror. Since we started with unity reflectivity, the scattering contribution is therefore $I_{st} = 1 - I_{sp}$. The integral scattering contribution depends only on the height distribution and reads for a normal distribution $1 - e^{-g_o}$. This dependence of the integral scattering contribution on wavelength, grazing angle, and the average roughness allows to determine the roughness from scattering measurements without knowledge of the lateral distribution, that is, of the autocorrelation function. The indirect determination of the roughness from scattering measurements has the advantage of the strong σ - dependence of the scattering; for small g_o the dependence is quadratic. The largest scattering increase is obtained as a function of σ , if α and λ are chosen such that $g_o \approx 1$.

If we assume an exponential distribution of heights, $w(z) = \frac{1}{2\sigma} e^{-\frac{|z|}{\sigma}}$, then we have for the specularly reflected contribution $I_{sp} = \frac{1}{(1+g_o)^2}$ and for the scattering contribution $I_{st} = \frac{g_o(2+g_o)}{(1+g_o)^2}$ In general we find that the (symmetric) height distribution is proportional to the Fourier transform of the square root of the integral scattering component: $w(z) = \mathcal{F}^{-}(\sqrt{I_{str}(v_z)})$. Due to the dependence of the integral scattering component on grazing angle and /40 the ratio of wavelength and roughness we are able to determine the height distribution.

We have already mentioned that the statistics of the surface are not completely determined by the height distribution; the required additional information is a measure for the lateral distances of mountains and valleys. The probability to find at a point (x_1, y_1) a height z_1 and a point (x_2, y_2) a height z_2 does not equal the product of the two individual probabilities $w(z_1)w(z_2)$; instead, the values are correlated:

$$w(z_1,z_2) = \frac{1}{2\pi\sigma^2\sqrt{1-C^2}} \exp\left(-\frac{z_1^2 - 2C z_1 z_2 + z_2^2}{2\sigma^2(1-C^2)}\right) \qquad (27)$$

if w(z) is a normal distribution.

One can easily verify that

$$\langle h(x_1,y_1)h(x_2,y_2)\rangle = \int_{-\infty}^{\infty}\int_{-\infty}^{\infty} z_1 z_2 w(z_1,z_2)\,dz_1 dz_2 = C\,\sigma^2,$$

that is, $C = \frac{\langle h_1 h_2\rangle}{\langle h_1^2\rangle}$. Thus, C is the autocorrelation function as defined in Eq. (16) for isotropically rough surfaces. If we compute the expectation value needed in Eq. (23), viz.,

$$\langle \exp(iv_z(h(x_1,y_1)-h(x_2,y_2))\rangle = \exp(-g(1-C)) \qquad (28)$$

and introduce Eq. (28) into (23), then

$$\langle|s|^2\rangle - |\langle s\rangle|^2 = D(s) = \frac{2\pi F^2}{A}\int_0^{\infty} J_0(\tau\sqrt{v_x^2+v_y^2})\left[e^{-g(1-C)} - e^{-g}\right]\tau\,d\tau \qquad (29)$$

where $x_1 - x_2 = \tau\cos\varphi$ and $y_1 - y_2 = \tau\sin\varphi$. At this point, we have reduced the quadruple integral of Eq. (23) to a single integral. Eq. (29) already shows that the scattering distribution in the γ-direction is reduced by the factor $\sin\alpha$ with respect to the φ-direction, that is $\sqrt{v_x^2+v_y^2} \approx k\sqrt{\varphi^2\alpha^2+\gamma^2}$. If $\varphi = 0$ and $\gamma = \gamma_0$,/41 then we find for $D(s)$ the same value at $\gamma = 0$ and at $\varphi = \frac{\gamma_0}{\alpha}$. This statement will be verified in a quantitative form in Section 4.6. All other measurements require for the comparison an integration of $D(s)$ over γ:

$$\int_{-\frac{\pi}{2}}^{\frac{\pi}{2}} D(s)\,d\gamma \approx \frac{2\pi F^2}{A}\int_0^{\infty}\left\{\int_{-\infty}^{\infty} J_0(\tau k\sqrt{\varphi^2\alpha^2+\gamma^2})\,d\gamma\right\}_1 \cdot \left\{e^{-g(1-C)} - e^{-g}\right\}_2 \tau\,d\tau$$

The first curved bracket under the integral reduces to

$$\{\}_1 = 2\varphi\alpha\int_{-\infty}^{\infty} x\,\frac{J_0(xy)}{\sqrt{x^2-1}}\,dx = 2\varphi\alpha\,\frac{\cos y}{y} \qquad \text{with} \quad y = \tau\varphi\cdot\alpha\cdot k$$

from where

$$\int D(\varsigma)\, d\gamma = \frac{2\pi F^2}{A} \int_0^\infty \frac{2\cos(\tau\varphi\alpha k)}{k} \left[e^{gC} - 1 \right] e^{-g}\, d\tau$$

$$\int D(\varsigma)\, d\gamma = \frac{4\pi F^2}{kA} e^{-g} \sum_{m=1}^{\infty} \frac{g^m}{m!} \int_0^\infty \cos(\tau\varphi\alpha k)\, C^m(\tau)\, d\tau$$

If in particular, $g \ll 1$, so that the series can be terminated after the first term, then the distribution of the incoherently reflected radiation at the slit image function is proportional to the Fourier transform of the autocorrelation function (except for the weak angular dependence of g on φ):

$$D(\varsigma) = g \frac{4\pi F^2}{Ak} e^{-g} \int_0^\infty \cos(\tau\varphi\alpha k) C(\tau)\, d\tau$$

In the case of a Gaussian autocorrelation function, $C(\tau) = e^{-\left(\frac{\tau}{T}\right)^2}$ the scattering halo is proportional to

$$I_{Str} \propto F^2 \sum_{m=1}^{\infty} \frac{g^m}{m!\sqrt{m}} e^{-\left(\frac{\varphi}{\Theta_m}\right)^2} \quad \text{with} \quad \Theta_m = \frac{2\sqrt{m}}{Tk\alpha}$$

Optical measurements [13] suggest an exponential autocorrelation function: $C(\tau) = e^{-\frac{|\tau|}{T}}$. This results in a scattering halo proportional to

$$I_{Str} \propto \sum_{m=1}^{\infty} \frac{g^m}{m!\sqrt{m}} \frac{1}{1 + \left(\frac{\varphi}{\Theta_m}\right)^2} \quad \text{with} \quad \Theta_m = \frac{m}{kT\alpha}$$

We shall compare in Section 4.4 these results with measurements.

3.5. Contribution by Thomson Scattering /42

Aside from surface scatterings, processes in deeper layers of the mirror material contribute to the total scattering intensity. In order to obtain estimates of this contribution by volume scattering, we first need the penetration depth of an electromagnetic wave.

Upon reflection at the boundary layer between the vacuum and a material medium, an electromagnetic wave spreads through the latter with the amplitude decreasing with depth z according to the formula

$$A = A_o \exp(-k \sqrt{\cos^2\alpha - n^2} \cdot z \qquad (37)$$

c.f., for instance, reference [6]. The same is true in the case of external total reflection, except that here (for $\beta = o$) no energy enters the medium, that is, the wave stays at the surface. Eq. (37) yields for perpendicular incidence: $A = A_o e^{-iknz}$. The penetration depth T where the energy has decreased to 1/e is found from $2\,\mathrm{Re}(iknT) = 1$ so that $T = \frac{1}{2k\beta} = \frac{1}{\tau}$ where τ is the well-known absorption coefficient. In the case of grazing incidence, however, the penetration depth is not only determined by absorption. In particular, in the case that $\alpha = o$, we have

$$T = \frac{1}{2k\,\mathrm{Re}\sqrt{2i\beta + 2\delta}} = \frac{1}{2k\sqrt{\delta + \sqrt{\beta^2 + \delta^2}}} \qquad (38)$$

The penetration depth does not vanish for $\alpha \to o$; the behavior of this depth as a function of the grazing angle is shown in Fig. 18. The penetration depth is nearly the same for different energies in the case of grazing incidence. This is explained by the fact that δ is proportional to λ^2, except for the influence of the atomic shell structure (see Section 3.2.). If one neglects in Eq./44 (38) the absorption, the T is independent of λ .

In order to obtain estimates of the volume scattering contribution we assume a total (that is, coherently and incoherently scattered) cross section of typically 4.0 barn/atom; this value is based on gold and 1 keV, according to reference [55]. The corresponding scattering coefficient is $\mu = 0.24\ \mathrm{cm}^{-1}$. If the penetration depth is only 20 Å, then the scattering contribution without absorption at the point of leaving is about 5×10^{-8}. In the framework of our current work this level is much below measurability.

Abnormal reflection known as Yoneda effect is not expected in

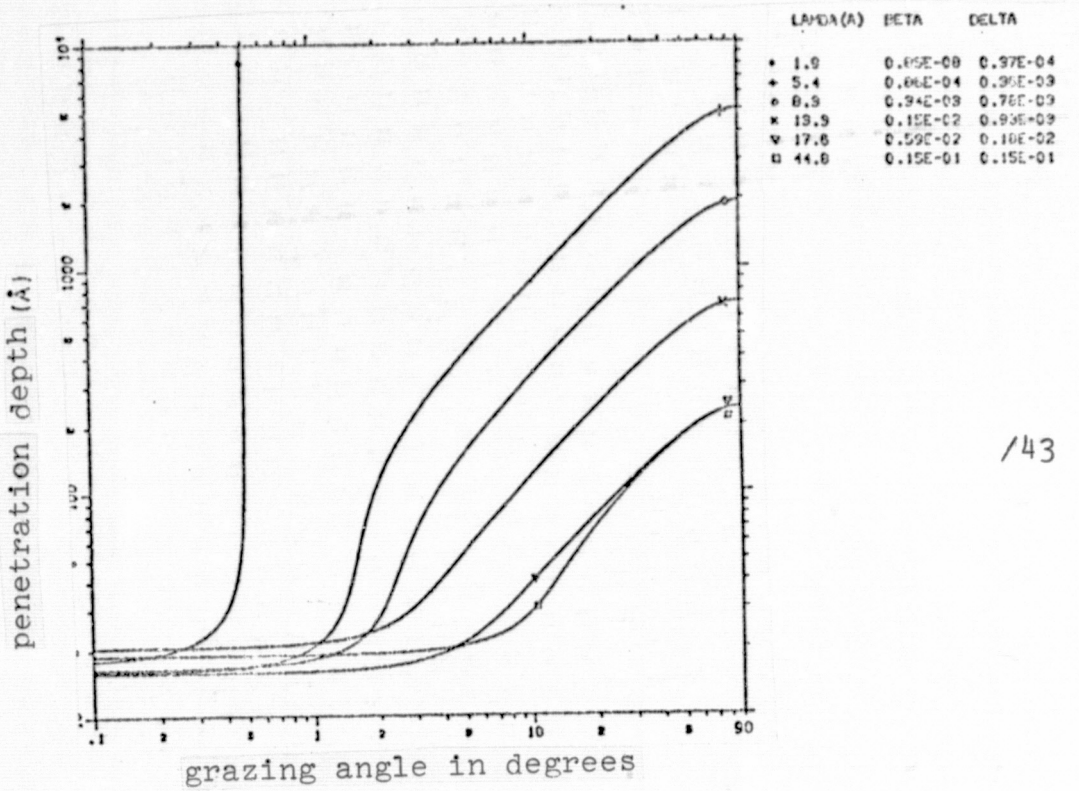

/43

Figure 18a. Penetration depth as a function of wavelength and grazing angle. Mirror material: nickel.

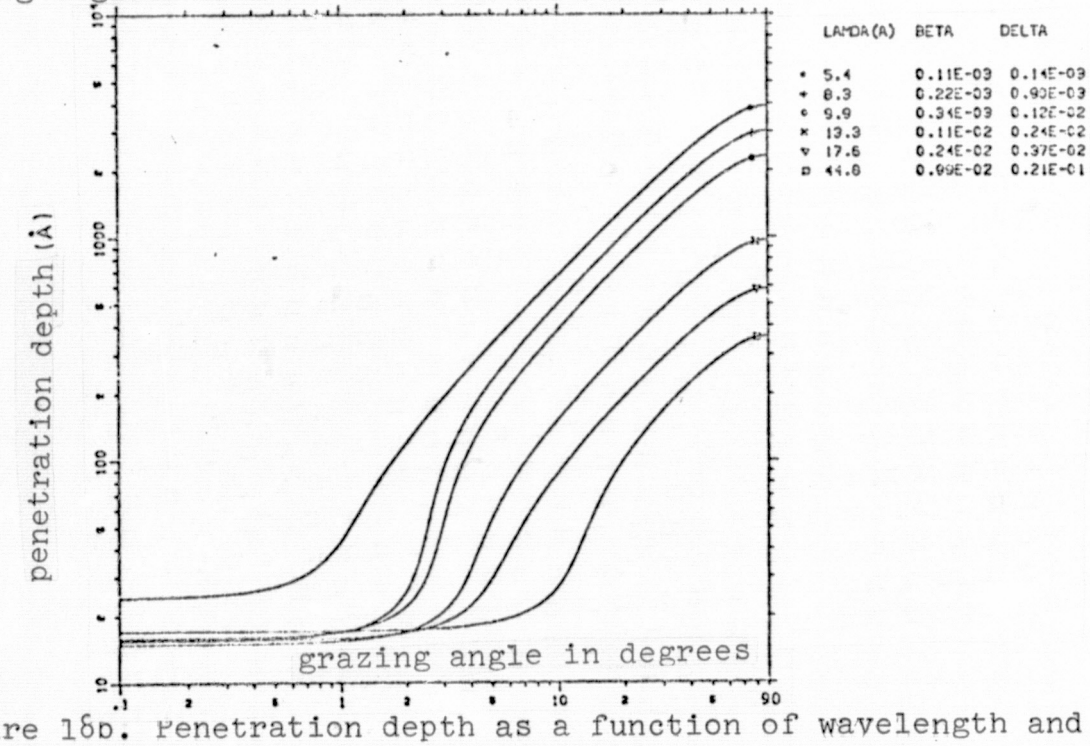

Figure 18b. Penetration depth as a function of wavelength and grazing angle. Mirror material: gold.

the angular range below the limiting angle for total reflection; in addition, it can be excluded on the basis of measurements, since no maximum of the scattering intensity was observed outside the specular direction.

As a consequence, we feel that scattering under reflection is well described by simple surface scattering in the case of soft X-rays.

3.6. The Influence of Scattering on the Image Quality of the Telescope

/45

There are two points in which the scattering by plane mirrors as we have treated it so far differs from the case of scattering in the actual telescope: for one, the mirrors are curved, so that a translation onto rotational symmetry is required, although locally the scattering events can be described by the results of the theory in the framework of plane mirrors. Second, there is double scattering. The distribution into specularly reflected and into scattered components in the case of double reflection is shown in Fig. 19. Here, the q_i's are the scattered components as computed in Section 3.4: $q_i = 1 - e^{-g_{oi}} R_i$ are the reflectivities for the grazing angle α_i. The total specularly reflected contribution then read (normalized to the total of incoming energy):

$$\frac{I_{sp}}{I_o} = (1 - q_1)(1 - q_2) \tag{39}$$

for the total scattered contribution, and we have

$$\frac{I_{str}}{I_o} = q_1 + q_2 - q_1 q_2 \tag{40}$$

In the case of very weak scattering at the surface, $q_i \ll 1$, we find that the integral scattering contribution in the case of double reflection is about twice the amount of single reflection.

We now compute the angular distribution for the case of a /46

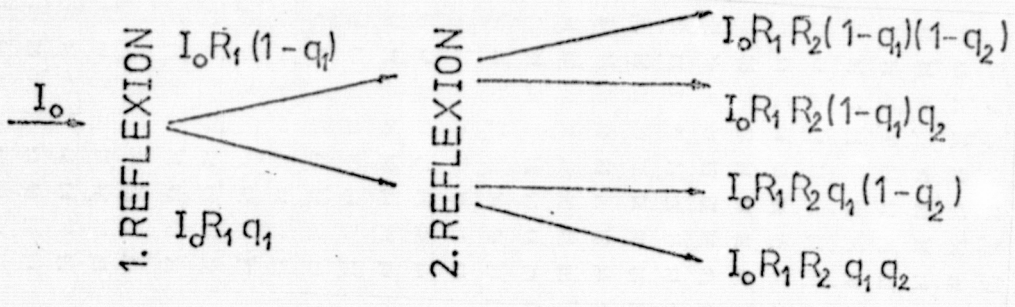

Figure 19. Schematics of double reflection with scattering.

Gaussian autocorrelation function: If the direction of incidence is in the xy-plane (that is, the x-axis corresponds to the optical axis), then the intensity distribution reads according to the above discussion:

$$I(y,z) = \text{const} \times \left\langle \frac{q_1}{\Theta_1} \exp\left[-\left(\frac{y}{x_1\Theta_1}\right)^2 - \left(\frac{z}{x_1\Theta_1\alpha_1}\right)^2\right] + \frac{q_2}{\Theta_2}\left[-\left(\frac{y}{x_2\Theta_2}\right)^2 - \left(\frac{z}{x_2\Theta_2\alpha_2}\right)^2\right] \right\rangle \quad (41)$$

where we have taken into account the fact that the integral scattering contribution as well as the width of the halo, Θ_i, depend on the grazing angle. If we set $x_1 = f + s$, $x_2 = f - s$, $\alpha_1 = \alpha_o - \delta$, $\alpha_2 = \alpha_o + \delta$ and if we compute I(y,z) in first approximation for small s $(s \ll f)$ and for $\delta \ll \alpha_o$, then we obtain, recalling that $\alpha_i \Theta_i = \text{const.} \stackrel{!}{=} \alpha_o \Theta_o$:

$$I(y,z) = \text{const.} \times \left\langle \exp\left(-\left(\frac{y}{f\Theta_o}\right)^2 - \left(\frac{z}{f\Theta_o\alpha_o}\right)^2\right) \left\{ \frac{q_1 q_2}{\Theta_o \alpha_o} \exp(A) + \frac{q_1 \alpha_2}{\Theta_o \alpha_o} \exp(-A) \right\} \right\rangle \quad (42)$$

where

$$A = 2\left(\frac{y}{f\Theta_o}\right)^2 \left(\frac{\delta}{\alpha_o} + \frac{s}{f}\right) + \left(\frac{z}{\Theta_o \alpha_o f}\right)^2 \frac{s}{f} .$$

If in addition we recall that q_i is proportional to α_i^2 (see Section 3.4), then we can apply an expansion and find that the curved bracket is independent of the point of incidence:

$$I(y,z) = \text{const.} \times \exp\left(-\left(\frac{y}{f\Theta_0}\right)^2 - \left(\frac{z}{f\Theta_0\alpha_0}\right)^2\right). \qquad (43)$$

Hence, we see that the different grazing angles and distances to the focal point at the points of reflection do not change the scattering intensity distribution by comparison with the case of single reflection. The only effect is a doubling of the scattering amplitude. If one also takes into account the fact that the radiation that had been scattered at the first mirror does not encounter during the second (specular) reflection a plane mirror, then one finds a small widening and flattening of the scattering distribution

/47

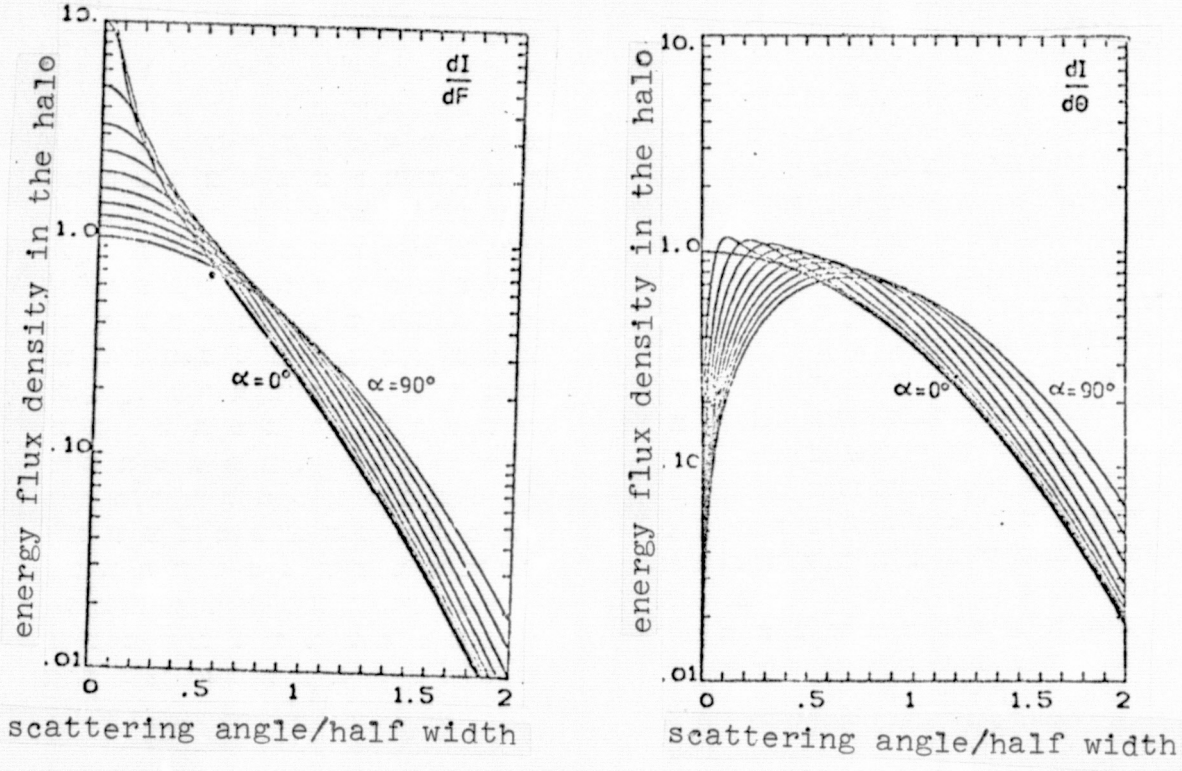

Figure 20. Rotationally symmetric scattering distribution:

a) $I_F dF$ b) $I_\Theta d\Theta$

In order to change to the rotationally symmetric situation we introduce in the focal plane the coordinates φ and ϑ:

PRECEDING PAGE BLANK NOT FILMED

$\frac{y}{f} = \vartheta\cos\varphi$, $\frac{z}{f} = \vartheta\sin\varphi$. The quantity $d\Theta = 2\pi\vartheta d\vartheta$ then represents an infinitesimal ring element. The Gaussian scattering distribution, transformed to rotational symmetry, reads in these coordinates: $I_\Theta d\Theta \propto (\int_0^{2\pi} \exp(-x^2 - (\frac{y}{s})^2)\,\vartheta\, d\varphi)\, d\Theta$. The scattering width was set equal to 1 arcmin without loss of generality; s is the sine of the grazing angle. Integration results in $I_0\, d\Theta \propto e^{-\frac{\vartheta^2}{2}(1-\frac{1}{s^2})}\, J_0\left(\frac{1}{2}\vartheta^2(1-\frac{1}{s^2})\right) d\Theta$

Figure 20 shows these functions for $\sin\alpha = I \times 0.1$, $I \in [0, 10]$ The curves are normalized in such a fashion that the integral over $d\Theta$ is constant. If α tends to zero, the Gaussian form is retained; up to $\sin\alpha = 0.1$ the departures from the Gaussian shape are small and restricted to the range $\Theta \leq 0.2'$. Since the grazing angles for the 32 cm telescope are in the neighborhood of 1.5°, we expect behind the telescope a scattering distribution in $d\Theta$ similar to the one in $d\eta$ for the case of single scattering. Fig. 20a shows the transformation to constant surface elements dF in the focal plane.

The image contrast can be obtained from these data in the following fashion. If

$$I(\Theta) = \frac{1-q}{\sqrt{\pi}\,B}\, e^{-\left(\frac{\Theta}{B}\right)^2} + \frac{q}{\sqrt{\pi}\,H}\, e^{-\left(\frac{\Theta}{H}\right)^2} \qquad (46)$$

is the point image function of the telescope, $q = q_1 + q_2$ the integral scattering contribution, B the half width of the point image function, and H the half width of the scattering distribution, then the image contrast:

$$K = \frac{A_{max} - A_{min}}{A_{max} + A_{min}}$$

for a point source reads

$$K = \frac{1}{1 + \frac{2q}{1-q}\,\frac{B}{H}} \approx 1 - \frac{2q}{1-q}\,\frac{B}{H} \qquad (47)$$

If on the other hand, an extended source is the object, then the central portion of the point image function is more strongly widened than the halo, and the resulting contrast is reduced. Let us, for example, consider a Gaussian source intensity profile: $Q(\Theta) = \frac{1}{\sqrt{\pi}F} e^{-\left(\frac{\Theta}{F}\right)^2}$. In this case we obtain a contrast

$$K = \left(1 + \frac{2q}{1-q} \cdot \sqrt{\frac{B^2 + F^2}{H^2 + F^2}}\right)^{-1} \qquad (48)$$

This function is plotted in Figure 21 against the image width/49 F. The scattering component was assumed as q = 0.1, B = 15 arcsec, and H = 10 arcmin. So long as the extent of the source is small with respect to the resolution of the telescope, the contrast follows Eq. (47). If the image width equals the width of the scattering halo divided by $\sqrt{3}$, the contrast is reduced to 1-q. In the case of very extended sources the contrast does not go to zero; instead for $F \to \infty$ it tends to the limiting value $K = \frac{1-q}{1+q}$. This value reads for the above values of B, H, and q about 0.822. Thus, the image contrast can not only be improved by decreasing the integral scattering contribution, but also by increasing the resolution and by widening the scattering halo. In terms of polishing this means that one should attempt to have very small and high-frequency roughness.

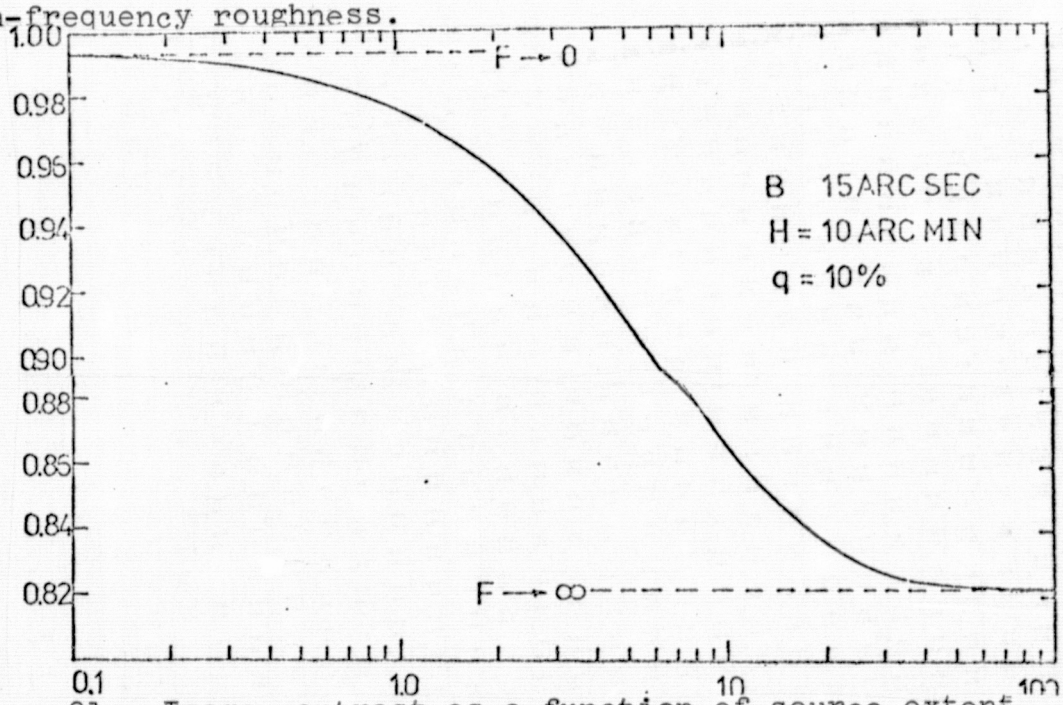

Figure 21. Image contrast as a function of source extent

4.1. Experimental Setup

The measurements of the scattering distribution were carried out with the aid of three different experimental setups which in their basic principles are quite similar (Fig. 22): An X-ray tube produces a characteristic X-ray spectrum, a collimator consisting of two slits or circular diaphragms forms a ray of some arcmin /51 (10^{-8} sterad), which is reflected at the mirror that is supposed to be tested. The intensity distribution is measured in the plane of the detector with the aid of a proportional counter with slit or circular diaphragm in front. The following table summarizes the dimensions of the apparatus:

	A (mm)	B (mm)	C (mm)	D (mm)	slit (μ)	slit (μ)	slit t3 (μ)
I	500	2370	510	2100	100/50	100/50	300/50
II	870	3000	945	2990	100/600∅	100/600∅	100/600∅
III	1300	11580	1900	3224	300	300	300

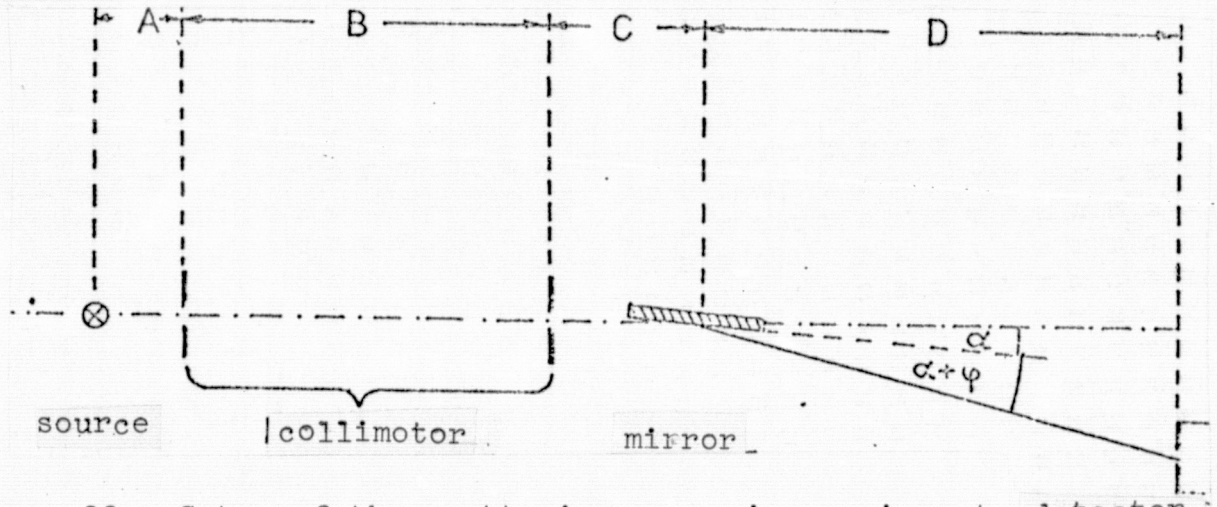

Figure 22. Setup of the scattering measuring equipment

With all three setups it is possible to remove the mirror so that a comparison with the intensity distribution of the direct ray is possible. All measurements were made at a pressure of less or or about 10^{-4} mbar. Apparatus I was made in Tubingen, II and III in

Garching and Neuried near Munich, respectively.

4.2. Survey of the Investigated Samples and of the Measured Roughness

Figure 23 provides a first orientation of the influence of the microroughness on the scattering behavior in the X-ray range: plotted are the scattering distributions for three more or less well polished samples on top of each other, with the normalization /52 done for equal total intensity. The cloth-polished kanigen sample shows at a grazing angle of 1.5° and a wavelength of 8.3 Å already so much scattering that it is impossible to separate the specularly reflected portion from the scattering halo; the half width/53 is clearly enlarged. Cloth polishing techniques are used for mirrors where the focussing is demanded, but not a high image quality in the proper sense, that is, in particular, high contrast; that is, for instance, the case with ASTRO-8 a rocket experiment done by the MPE that was flown successfully in January 1977. It consists of 12 connected paraboloids, each with 120 cm^2 geometrical collector surface. The second example is the well polished kanigen sample #23. The specularly reflected portion is clearly separated from the scattering halo. The integral scattering component amounts to about 30% which, according to Section 3.4, indicates a roughness of about 15 Å. The third measurement refers to one of the best samples #27. Here, the roughness derived from the measurements is only about 4 Å. In a qualitative fashion the difference between samples 23 and 27 could be verified by means of the micro-testing techniques with the aid of a Perthometer (see Section 4.10).

The table below shows a summary of the investigated samples. The samples were polished by the Zeiss Company in Oberkochen, except for samples 11 to 15 which are parts of the Baez telescope of the Harvard College Observatory/SAO, Cambridge, Mass., and which were measured after the flight [18]. Column 1 gives a brief description

of the sample, columns 2 and 3 state the grazing angle and the wavelength. Column 4 contains the integral scattering components, with the resulting roughness given in column 5; column 6 finally specifies the apparatus with which the measurement was done.

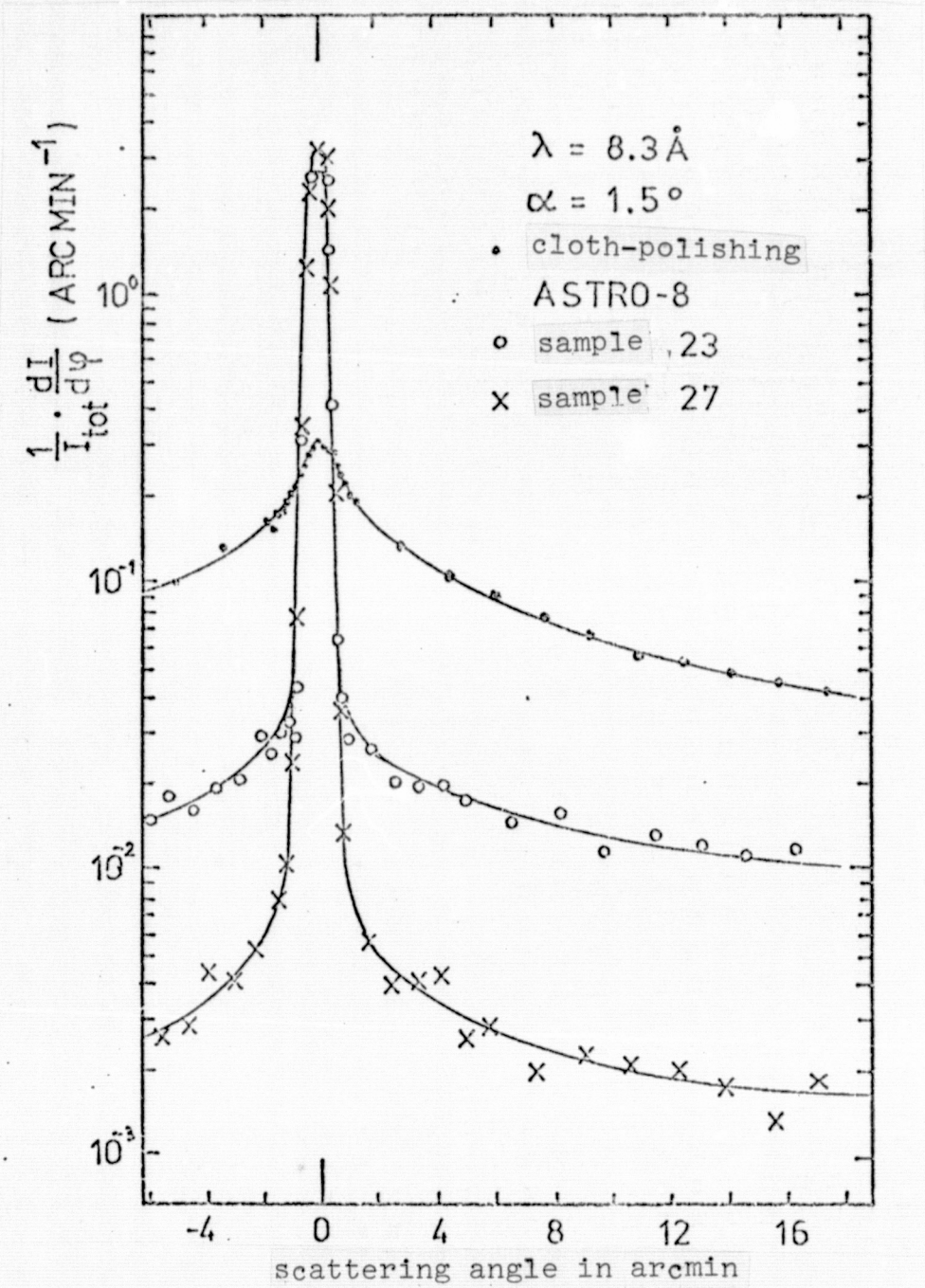

Figure 23. Comparison of the scattering distributions of three samples.

Probe	Grazing angle	Wave-length (Å)	Scattering (%)	σ (Å)	Apparatus
1 Replica on zerodur, gold surface					
2 Replica on zerodur, gold surface	1.5°	13.3	2	6	I
3 Replica on Al, etched gold surface	1.5°	13.3	6	1o	I
4 Zerodur	1.5°	13.3	4o	28.7	I
5 Original for 1 and 2, zerodur, gold surface	1.5°	8.3	57	23.1	I
	1.o°	13.3	2	9	I
11 floated glass	1.5°	8.3	1o	8	I
12 Floated glass, cleaned	1.o°	13.3	19.o	26.4	I
	1.5°	13.3	36.4	24.4	I
	1.o°	8.3	38.1	23.4	I
	1.5°	8.3	46.o	17.1	I
	1.o°	13.3	8.4	17.6	I
13 Floated glass, cleaned	1.5°	13.3	-	-	I
	1.o°	8.3	9.1	11.4	I
	1.5°	8.3	-	-	I
	1.o°	13.3	-	-	I
14 Floated glass, cleaned	1.5°	13.3	6.6	1o.4	I
	1.o°	8.3	-	-	I
	1.5°	8.3	7.3	6.8	I
	1.o°	13.3	11.o	2o.1	I
15 Kanigen on Al	1.5°	13.3	14.4	15.3	I
	1.o°	8.3	15.3	14.8	I
	1.5°	8.3	19.9	11.3	I
	1.o°	13.3	1.4	7.2	I
	1.5°	13.3	1.7	5.3	I
23 Kanigen on Al	1.o°	8.3	2.3	5.7	I
	1.5°	8.3	3.4	4.7	I
	1.5°	8.3	3o	15	I

24 Kanigen on Al	1.5°	8.3	16	1o	I
27 Kanigen on Al	1.5°	13.3	1	4	I
	1.5°	8.3	2	4	I
29 Kanigen on Al	1.5°	13.3	2	8	I
	1.5°	8.3	12	9	I
30 Zerodur, original of 3	1.5°	13.3	2	6	I
	1.5°	8.3	3	4	I
33 Kanigen on Al	1.5°	8.3	1o	8	I
33A Sample 33 after storage (30 d)	1.5°	13.3	6	6	I
	1.5°	8.3	1o	8	I
34 Kanigen on Al	1.5°	8.3	5	6	I
34A Sample 34 after varnish test (blue varnish) removed with acetone and ether	1.5°	8.3	1o	8	I
37 Kanigen on Al	1.o°	13.3	3.o	1o.5	II
	1.5°	13.3	4	8	I
	2.o°	13.3	3.4	5.6	II
	3.o°	13.3	5.4	4.7	II
	1.5°	8.3	6	6	I
37A Sample 37 after varnish test (blue varnish), 30 min acid bath, removed with acetone and ether	1.5°	8.3	9	8	I
38 Kanigen on Al, cloth polish	o.5°	13.3	47	52	III
	1.o°	13.3	82	49	III
	1.5°	13.3	85	44	III
	2.o°	13.3	9o	46	III
	1.5°	8.3	97	47	I
38A Sample 38 polished a second time (cloth)	o.5°	44.8	7	1o8	III
	o.6°	17.6	5o	116	III
	o.6°	13.3	67	111	III
	o.6°	8.3	89	96	III
	o.8°	13.3	86	1o2	III
	o.8°	8.3	98	91	III
	1.o°	44.8	29	11o	III
	1.1°	17.6	88	1o8	III

		1.1°	13.3	95	98	III
		1.3°	13.3	1oo	119	III
		1.5°	44.8	45	1o5	III
		1.5°	17.6	99	113	III
		2.o°	44.8	72	116	III
		1.2°	44.8	39	113	III
38A	Sample 38 two-dimensional scattering distribution	o.5°	17.6	-	-	II
		1.o°	17.6	-	-	II
39	Kanigen on Al	o.5°	8.3	-	-	II
		1.5°	13.3	4	8	I
		1.5°	8.3	7	7	I
39A	Sample 39, varnish test (0576), removed with acetone and ether	1.5°	8.3	1o	8	I
39B	Sample 39A with gold surface	o.5°	13.3	7	33	III
		o.6°	9.9	6	2o	III
		o.6°	8.3	6	16	III
		o.5°	5.4	11	17	III
		1.1°	13.3	8	16	III
		1.1°	9.9	9	13	III
		1.o°	8.3	7	1o	III
		1.o°	5.4	18	11	III
		1.5°	13.3	11	14	III
		1.5°	9.9	11	1o	III
		1.5°	8.3	1o	8	III
		2.o°	13.3	14	12	III
		2.o°	9.9	17	1o	III
		2.o°	8.3	15	8	III
50	Kanigen on Al, with preferential direction	∥ o.5°	8.3	2.5	11.9	II
		∥ 1.o°	8.3	7.1	1o.o	II
		∥ 2.o°	8.3	29.7	11.2	II
		⊥ 1.o°	8.3	4.7	8.1	II
		⊥ 2.o°	8.3	9.4	5.9	II

60 Kanigen on Al, gold surface	0.5^{o}	13.3	o.2	5.4	II
	1.5^{o}	13.3	o.3	2.2	II
	2.0^{o}	13.3	o.3	1.7	II
	2.5^{o}	13.3	o.4	1.5	II
61 Homosil, gold surface	3.0^{o}	13.3	o.6	1.6	II
	1.0^{o}	8.3	o.o7	3.15	II
	1.5^{o}	8.3	o.12	2.73	II
	2.0^{o}	8.3	o.17	2.45	II
	2.5^{o}	8.3	o.17	1.96	II
	3.0^{o}	8.3	o.36	2.41	II

After some preliminary tests of the choice of material as well as the polishing technique [25] we chose for the 32 cm telescope kanigen on aluminum. Thus, the majority of the above samples consists of aluminum with a kanigen surface that had been carefully polished. The samples 23 to 29 were used to test methods to apply the kanigen as well as the polishing materials and techniques (Zeiss Company, Oberkochen). With an optimum method defined, a set of samples [33 to 39] was produced in order to test the reproducibility of the optimum polish. The roughness of these samples is between 6 and 8 Å and, on the average, (7.2 $\pm$ 1.0) Å.

The later varnish tests of these samples were also designed [33A to 39A] for the production problems of the 32 cm telescope /58 (see Section 4.5).

We had indeed expected to encounter difficulties when, upon completion of the telescope, the polishing technique had to be applied to a two-dimensionally curved surface. At this time, scattering investigations are carried out with the finished paraboloid-hyperboloid system in the X-ray range. The first tests indicate a roughness of about 10 Å. Thus, the telescope is well suited to observe astrophysical scattering holes: At $\lambda = 13.3$Å and for dust

grain sizes of 0.8 µm the expected astrophysical halo (Sco X-1) is about one order of magnitude above the experimental halo as it appears from reflection in the limit of vanishing scattering angle.

Aside from our studies with respect to the development of the telescope we have, with samples 1 to 5, tested a method for the production of highly polished mirrors which promises to reduce costs drastically in the future, namely, the so-called replica method (Section 4.7). A special case is presented by sample 50 where we tested a possibility to improve the scattering behavior by the choice of a preferred polishing direction. The cloth polishing as applied to samples 38, 38A, and 39B is less expensive and useful for mirrors which are not supposed to produce exact images, /59 but rather to focus solely (paraboloid mirrors of the ASTRO-8 type). The sample was used to investigate the decrease of reflectivity through microroughness (Section 4.9). The samples were also used together with the samples 60 and 61 to investigate the dependence of the scattering on grazing angle and wavelength with the aim of verifying the applicability of the statistical surface scattering theory (Section 4.3). Samples 11 to 15 are pieces of the Baez telescope of the Harvard College Observatory/SAO, Cambridge, Mass., that were flown successfully and partially cleaned and tested for scattering. The results are that floated glass has a surface quality similar to that of the optimally polished kanigen mirror.

Some of the measurements will be discussed in detail below.

4.3. Integral Scattering Component

According to Section 3.4., the incoherently scattered contribution to the total reflected energy flux is independent of the exact form and lateral distribution of the unevenness of the mirrors. It is only the standard roughness σ which influences this quality: In the case of a normal distribution of the heights we have for the integral scattering contribution:

$$I_{Str} = 1 - e^{-g} \quad \text{where} \quad g_0 = (2k\sigma\alpha)^2$$

Since grazing angle and wavelength are known, this quantity allows to test the applicability of the statistical surface scattering /60 theory (Section 3.4) in the energy range of soft X-rays and in the case of grazing incidence. If, in turn, the applicability of this theory is verified, then X-ray measurements are excellent means to determine the microroughness of optical mirrors:

$$\sigma = \frac{\lambda}{4\pi\alpha}\sqrt{-\ln(1 - I_{Str})}$$

Aside from studying the λ-and α-dependence of the scattering component with samples 38A, 39B, 60 and 61 we carried out comparison measurements in order to determine the roughness depth on the basis of other methods (Section 4.10) but with the same samples.

The parameter g_0 was determined from the measurements in the following manner: Angular measurements ($|\varphi|_{max} \approx 1^o$) were integrated over the entire angular range, except for $|\varphi| \leq$ 1 arcmin , with an exponential interpolation for the behavior of the scattering flux density for $|\varphi| > 1^o$. In the table below the fourth column shows this integral in units of counts/sec·arcmin. Column 1 shows the number of the measurements, column 2 the measured portion of column 4, column 3 the extrapolated portion.

In order to obtain a clear picture of the separation of the specularly reflected component and the scattering halo, we have carried out scattering measurements at very small angles($|\varphi| \leq$2arcmin). These measured curves were integrated over the range $|\varphi| \leq$ 1arcmin. The halo component of this integral was obtained by extrapolation of the halo from the range o.5arcmin $\leq |\varphi| \leq$ 2arcmin to the range $|\varphi| \leq$ o.5arcmin . Column 5 identifies the running number of this small-angle measurement, column 6 states the integral

1 Nr	2 Measure-ment Σ(I/21')	Extra-polation 3 ΣExtr (I/21')	4 Σtotal (I/21')	5 Nr	6 Measure-ment Σ(I/21')	Extra-polation 7 ΣExtr (I/21')	8 ΣPeak (I/21')	9 Σtotal	1o ΣHalo	11 g	12 α degree	13 σ(Å)	14 R
				9o				1843.6			o.o		
92	163.4	22.2	185.6	91	9o9.o	83.4	825.6	1o94.6	269.o	o.28	1.oo	1o8.5	o.59
94	243.9	9.4	253.3	93	596.3	125.2	471.1	849.6	378.5	o.55	1.5o	1o1.4	o.46
96	259.4	6o.1	319.5	95	329.6	1o1.8	227.8	649.1	421.3	1.o5	1.98	1o5.6	o.35
98	55.2	8.3	63.5	97	1294.7	29.6	1265.1	1358.2	93.o	o.o7	o.5o	1o8.9	o.74
1oo	2o7.4	46.2	253.6	99	671.3	84.7	586.6	924.9	338.3	o.46	1.25	11o.3	o.5o
				83				796.3			o.o		
85	288.3	71.1	359.4	84	114.8	61.4	53.4	474.2	42o.8	2.18	o.58	96.3	o.6o
87	266.1	4o.4	3o6.5	86	36.1	3o.5	5.6	342.6	337.o	4.11	o.84	91.3	o.43
				64				647.6			o.o		
66	142.o	14.5	156.5	65	246.4	44.3	2o2.1	4o2.9	2oo.8	o.69	o.58	116.2	o.62
68	2o3.7	3o.5	234.2	67	78.7	39.9	38.8	312.9	274.1	2.o9	1.o9	1o7.6	o.42
7o	2o5.2	9.8	215.o	69	31.1	27.7	3.4	246.1	242.7	4.27	1.49	112.6	o.37
				71				1178.6			o.o		
75	3o2.6	48.8	351.4	74	325.2	1o3.7	221.5	676.6	455.1	1.12	o.58	11o.6	o.57
77	368.5	38.o	4o6.5	76	72.7	5o.9	21.8	479.2	457.4	3.o9	1.o9	97.8	o.41
79	4o6.7	38.5	445.2	78	173.7	9o.o	83.7	618.9	535.2	2.oo	o.84	1o2.1	o.52
81	291.5	64.8	356.3	8o	41.o	34.3	6.7	397.3	39o.6	6.39	1.29	118.8	o.34

Measurement 1 to 11: Sample 38 , λ= 8.3Å
Measurement 2o to 28: Sample 39B, λ= 13.3Å
Measurement 31 to 39: Sample 39B, λ= 9.9Å
Measurement 42 to 5o: Sample 39B, λ= 8.3Å
Measurement 53 to 56: Sample 39B, λ= 5.4Å
Measurement 46 to 7o: Sample 38A, λ= 17.6Å
Measurement 71 to 81: Sample 38A, λ= 13.3Å
Measurement 83 to 87: Sample 38A, λ= 8.3Å
Measurement 9o to 1oo: Sample 38A, λ= 44.8Å

1	2 Measure-	Extra-	3	4	5	6 Measure-	Extra-	7	8	9	10	11	12	13	14
Nr	Σment $\|\varphi\|\geq 1'$	polation ΣExtr $\|\varphi\|\geq 1'$		Σtotal $\|\varphi\|\geq 1'$	Nr	Σment $\|\varphi\| < 1'$	ΣExtr $\|\varphi\| < 1'$		Σpeak $\|\varphi\| < 1'$	Σtotal	ΣHalo	g	α(degree	G(Å)	R
11					1					2742.7			o.o		
1o	799.3	49.1		848.4	2	1637.1	3o8.9		1328.2	2485.5	1157.3	o.63	o.58	51.7	o.91
9	97o.4	15.o		985.4	3	65o.9	355.6		295.3	1636.3	1341.o	1.71	1.oo	49.5	o.6o
8	8o9.4	7.5		816.9	4	382.2	321.6		6o.6	1199.1	1138.5	2.98	1.49	43.9	o.44
7	127.3	1.3		128.6	5	48.4	47.7		o.7	177.o	176.3	5.53	1.98	44.5	o.o6
					2o					1539.8			o.o		
22	5o.o	2.7		52.7	21	1149.1	34.2		1114.9	12o1.8	86.9	o.o75	o.51	32.6	o.78
24	39.o	4.7		43.3	23	91o.o	33.1		876.9	953.3	76.4	o.o83	1.o9	16.o	o.62
26	6o.o	7.5		67.5	25	711.5	21.5		69o.o	779.o	89.o	o.121	1.49	14.2	o.51
28	56.o	6.1		62.1	27	461.7	12.o		449.7	523.8	74.1	o.153	1.98	12.o	o.34
					31					1286.2			o.o		
33	41.3	2.o		43.3	32	1o7o.4	26.3		1o44.1	1113.7	69.6	o.o64	o.58	19.7	o.87
35	44.2	11.1		55.3	34	898.6	3o.8		867.8	953.9	86.1	o.o95	1.o9	12.8	o.74
37	59.3	1o.5		69.8	36	7o4.8	15.4		689.4	774.6	85.2	o.117	1.49	1o.4	o.6o
39	72.o	8.o		8o.o	38	458.7	11.8		446.9	538.7	91.8	o.187	1.98	9.9	o.42
					42					1514.4			o.o		
44	44.3	6.o		5o.3	43	1167.4	25.8		1141.6	1217.7	76.1	o.o64	o.58	16.5	o.8o
46	37.2	7.8		45.o	45	916.8	24.o		892.8	961.8	69.o	o.o74	1.oo	1o.3	o.64
48	48.5	6.7		45.2	47	697.6	26.3		671.3	742.8	71.5	o.1o1	1.49	8.1	o.49
5o	5o.o	8.3		58.3	49	4o5.4	9.9		395.5	463.7	68.2	o.159	1.98	7.6	o.31
					53					812.9			o.o		
55	25.2	7.1		32.3	54	496.1	26.3		469.8	528.4	58.6	o.118	o.5o	16.9	o.65
57	37.3	8.3		45.6	56	268.7	12.6		256.1	314.3	58.2	o.2o5	1.oo	11.1	o.39

over the range $|\varphi| \leq 1$arcmin , column 7 the extrapolated halo contribution for $|\varphi| \leq 1$arcmin and column 8 the specularly reflected component obtained from these operations (column 8 corresponds to column 6 minus column 7). The sum of columns 4 and 5 then yields the total reflected energy flux (column ?). Column 11, finally, shows the quantity g. The grazing angle is stated in column 12; columns 13 and 14 summarize the values for the roughness σ as obtained by computation from column 11, and the reflectivity in the form of the ratio of the values from column 9 and the corresponding integrals over the direct ray, respectively.

In the case of sample 38A we find by averaging all σ-values of the above table a mean roughness of: $\bar{\sigma} = (106.3 \pm 7.7)$Å. Making use of this value for the roughness, we have in Fig. 24 entered the theoretical dependence of the relative scattering contribution on the grazing angle as the solid curve. The wavelength parameters are 8.3Å, 13.3Å, 17.6Å and 44.8Å . The small error in the standard roughness of 7.7 Å corresponding to 7% is reflected in the data by the good agreement between the measured and the theoretical values. The error limits as shown were determined in the following manner: If P is the counting rate at the peak, S the counting rate in the halo, then the error Q = S/ (S+Q) reads

$$\Delta Q = \left| \frac{S + \Delta S}{P + \Delta P + S + \Delta S} - \frac{S}{S + P} \right| = \frac{1}{P+S} \left| \Delta S - \frac{S}{P+S} (\Delta P + \Delta S) \right|$$

/64

If the errors ΔS and ΔP are proportional to S and P, respectively, that is, $\Delta S = qS$, $\Delta P = qP$, then $\Delta Q = 2q(Q - Q^2)$.

For sample 38A we estimated the error in P and S to be about 20%. This results in a maximum error for Q = 0.5 of $\Delta Q_{max} = 10\%$ The departure of the experimental data from the corresponding theoretical curves is only in the case of large scattering larger than the error as computed above. That means that the rough-

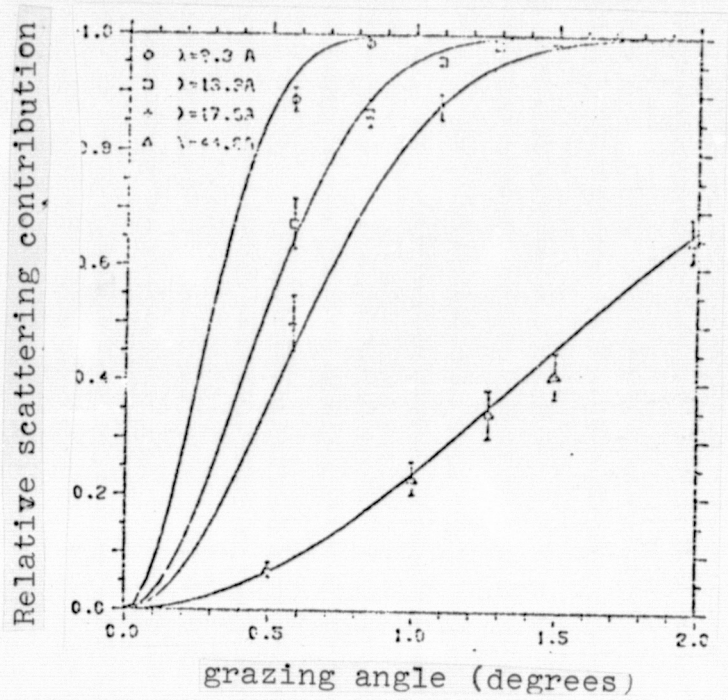

Figure 24. Comparison of theoretical and measured dependence of the integral scattering component on the grazing angle and the wavelength in the case of sample 38A.

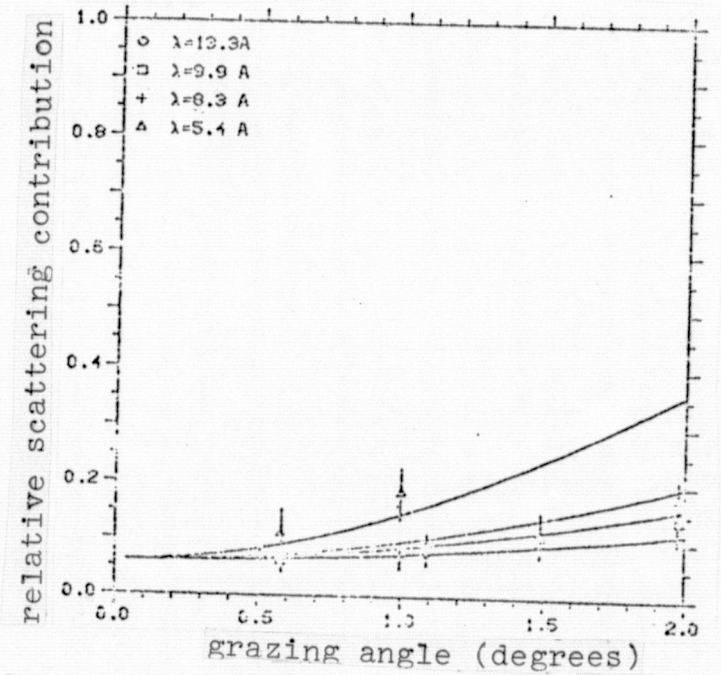

Figure 25. Comparison of theoretical and measured dependence of the integral scattering contribution on the grazing angle and the wavelength in the case of the sample 39B.

ness indeed follows a normal distribution. In the case of an exponential height distribution, $w(z) = \frac{1}{2\sigma} e^{-\frac{|z|}{\sigma}}$ we find a much larger mean error for the standard roughness: For $I_{Str} = 1 - \frac{1}{(1+g)^2}$ we find from the measurements a mean roughness of

$$\bar{\sigma} = (97.4 \pm 19.9)\text{Å}.$$

We shall compare this result in Section 4.10 for normal distribution ($\bar{\sigma} = 106$Å) with results of other roughness measurements.

The same reduction method has been used with sample 39B which represents a well polished kanigen sample with gold surface. The integral scattering contribution in this case is much less dependent on the grazing angle and the wavelength (Fig. 25). It should be mentioned, however, that in this case the errors ΔS and ΔP are much broader, so that the error increases during the extrapolation toward larger scattering angles. The evaluation according to the above method leads to a roughness of $\bar{\sigma} = (13.9 \pm 6.4)$Å. . If, on the other hand a fit of the type $I_{scatt} = I_{surface} + C$ is imposed on the measured values, then the constant C receives the value of 0.06 ± 0.02. This fit is also entered in Fig. 25. From here we find an average roughness of $\bar{\sigma} = (7.3 + 2.9)$Å. . The relative scattering of the single values of σ thus cannot be reduced significantly by introducing a constant scattering component /66 (change from 46 to 40%). There is also a basic difficulty involved in assuming a constant scattering component, since it was shown in Section 3.5 that the contribution of volume scattering is much less than 6%. It appears more probable that the departures from the exp(-g) - relation are due to an increase of the roughness toward the edges. The measurements were carried out with the aid of a 300μ collimator slit with the result that the irridated surface of the mirror was 34.4 mm wide at 0.5°, but only 8.6 mm wide at 2°. If only the measurements at a grazing angle of 2° are retained, then a mean roughness of (9.4 ± 2.1)Å is obtained and the scatter of individual values is only 22%.

Pictures taken with the multiray interference microscope (Section 4.10) did not verify an increase of the roughness toward the mirror edges; the resolution of optical measurement techniques is not sufficient for the purpose. In order to test the applicability of the above scattering theory for mirrors whose roughness is below 10 Å, a small sample was produced that could also be tested in an electron interference microscope (Section 4.10).

The dependence of the integral scattering component on the grazing angle in the case of highly polished samples was obtained with a gold-surface homosil sample with the aid of a 100 collimator (apparatus II): At 8.3 Å, the scattering distribution at 1°, 1.5°, 2°, 2.5° and 3° was measured and compared with the scattering of the direct ray: If the direct ray is separated into the peak and halo components D_p and D_H, with the corresponding components for the reflected ray $R_p + R_H$, then we have

$$R_p + R_H = (D_p + D_H) \circledcirc (\delta_p + H) \approx D_p + D_H + D_p \circledcirc H.$$

Here, $\delta_p + H$ is the slit image function of the mirror which has been decomposed in the same manner with a specular contribution δ and the scattering contribution H. Hence, if one subtracts from the reflected ray the reflected ray normalized to identical total intensity, then approximately the folding integral of the peak of the direct ray with the halo H is obtained. An example of this difference is shown in Fig. 26.

One might conceive of the scattering distribution as consisting of two contributions: A steeply decreasing component St_1 whose width suggests an autocorrelation length of $\gtrsim 50\mu$, and a broad contribution St_2 corresponding to an autocorrelation length of $\approx 6\mu$. The two components as well as the total scattering and the resulting values of g_1, g_2, σ_1, σ_2 are shown in the table to follow:

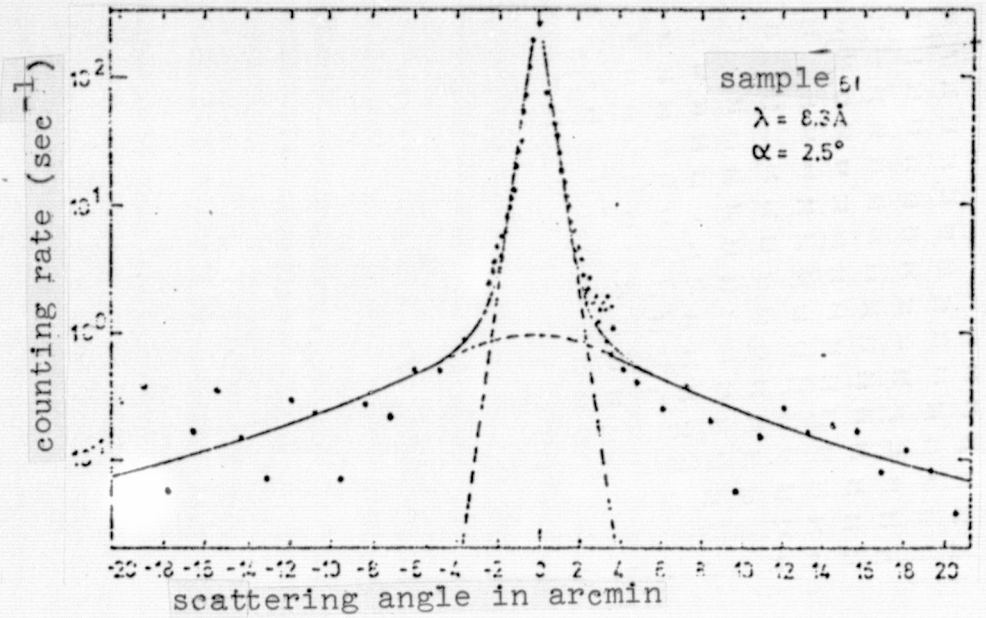

Figure 26. Scattering distribution (difference) for sample 61 for

$\lambda = 8.3$Å, $\alpha = 2.5^{o}$

	1.0°	1.5°	2.0°	2.5°	3.0°
Str_1	4.32×10^{-2}	8.15×10^{-2}	1.40×10^{-1}	2.09×10^{-1}	3.12×10^{-1}
Str_2	6.89×10^{-3}	1.16×10^{-2}	1.66×10^{-2}	1.66×10^{-2}	3.57×10^{-2}
St	5.10×10^{-2}	9.31×10^{-2}	1.57×10^{-1}	2.26×10^{-1}	3.48×10^{-1}
g_1	4.42×10^{-2}	8.50×10^{-2}	1.51×10^{-1}	2.34×10^{-1}	3.74×10^{-1}
g_2	6.91×10^{-3}	1.17×10^{-2}	1.67×10^{-2}	1.67×10^{-2}	3.64×10^{-2}
g	5.14×10^{-2}	9.77×10^{-2}	1.71×10^{-1}	2.56×10^{-1}	4.28×10^{-1}
σ_1 (Å)	7.96	7.36	7.35	7.32	7.72
σ_2 (Å)	3.15	2.73	2.45	1.96	2.41
σ (Å)	8.58	7.89	7.83	7.66	8.26

For the steeply decreasing component a roughness of $\sigma_1 = (7.5 \pm 0.3)$Å, is computed. Volume frequencies between $\frac{2\pi}{1\mu}$ and $\frac{2\pi}{15\mu}$ as taken into account for the same sample in the electron interference microscope, however, are only present with a mean roughness of $\sigma_2 = (2.54 \pm 0.44)$Å . In the present case the additive decomposition is allowed, since for small scattering ($g_0 \ll 1$) the scattering distribution is proportional to the Fourier comp- /69

onent of the autocorrelation function, so that as well $St_1 + St_2$ a:/69 $\mathcal{F}^+(c_1) + \mathcal{F}^+(c_2)$ (see Section 3.4). Fig. 27 summarizes the comparison of the two scattering components and of the total scattering contribution with the theoretically expected behavior as a function of the grazing angle. Both scattering components suggest a normal distribution in height. The corresponding theoretical curves agree within the error limits with the measured values. We conclude that even in the range of microroughnesses of only a few Å and for scattering contributions of a few percent the theory of surface scattering is adequate to describe the scattering process.

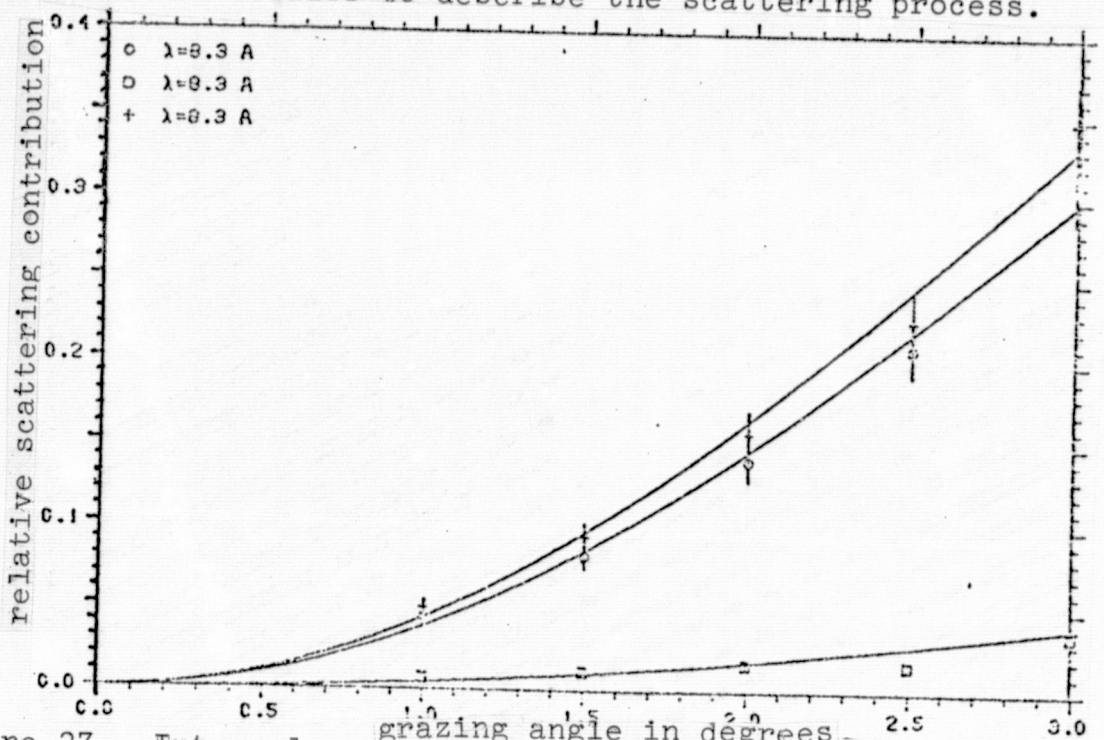

Figure 27. Integral scattering components St_1, St_2, and St as a function of grazing angle for sample 61.

4.4. Scattering Distribution

/70

According to Section 4.3, the scattering distribution not only yields a value for the roughness, ; in addition, the form of the distribution yields information on the behavior of the autocorrelation function. In the simplest case, that is, that of a very small scattering angle $(g_0 \ll 1)$, the autocorrelation function is pro-

portional to the Fourier transform of the scattering distribution (Eq. 34). Hence, one can derive the autocorrelation function directly from the scattering distribution. In the case of larger scattering, however, the scattering distribution is the sum of the Fourier transform of powers of the autocorrelation function (Eq. 33), and this relation cannot be solved any more for $C(\tau)$.

In order to determine the autocorrelation function from the measurements of sample 38A where the scattering contribution is not small with respect to unity, we have for various autocorrelation functions with the roughness G as determined in the last Section obtained the scattering distribution according to Eq. (33) and compared with the measurements. A Gaussian as well as a Lorentzian shape of the autocorrelation function could be excluded in this manner. The best agreement between the measured scattering distribution is obtained for an exponential shape of the autocorrelation function: $C(\tau) = e^{-\frac{|\tau|}{T}}$ This result agrees with the studies by Eastman and Baumeister [13] in the optical range.

The scattering distributions we have calculated in this man-/73
ner are shown in Figs. 28 a to j as solid curves ($T = 10.0\,\mu$). The vertical arrows at the positions -30, -45, and -90 arcmin show the position where the detector enters the shadow of the mirror so that the scattering intensity should decrease to zero. The constant background of 0.05 counts/sec has already been taken into account in this context.

Figures 28 a to j show good agreement of the measurements with the theoretical scattering curves; small departures are only evident in the immediate neighborhood of the specularly reflected component. This means that long-wavelength roughnesses ($\geq 50\mu$) are underrepresented in the exponential autocorrelation function. An ad- /74
ditional departure for the theoretical curves is found at $\alpha = 0.5°$ if φ tends to $-\alpha$: Here, the flux density of the intensity is less than expected. The reason for this behavior is the fact that the

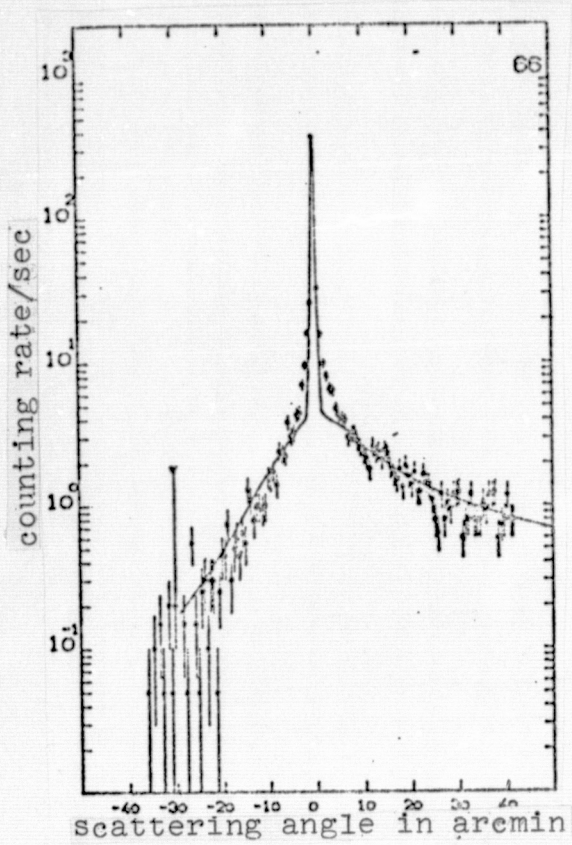

Figure 28a. $\lambda = 17.6\text{Å}, \alpha = 0.5^{o}$

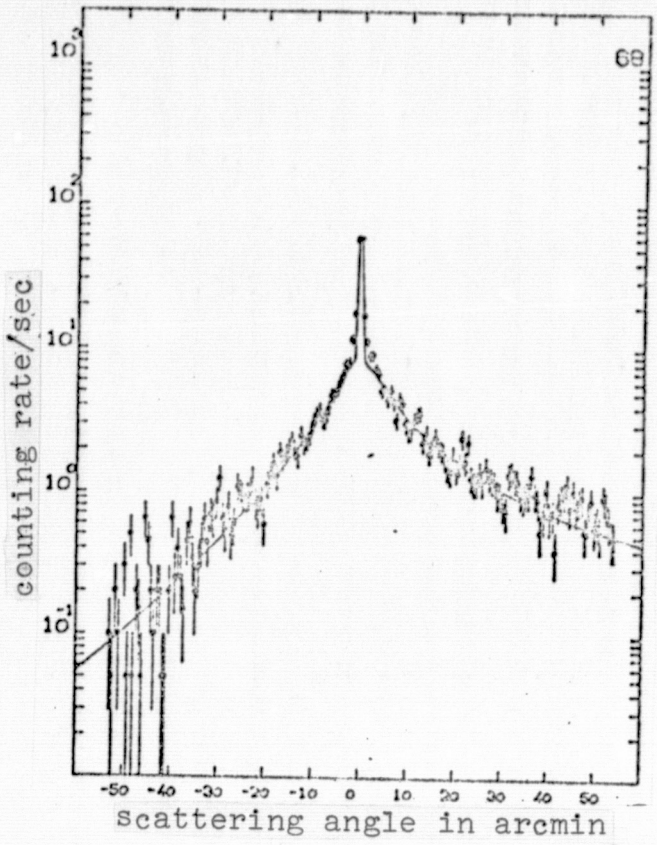

Figure 28b. $\lambda = 17.6\text{Å}, \alpha = 1.0^{o}$

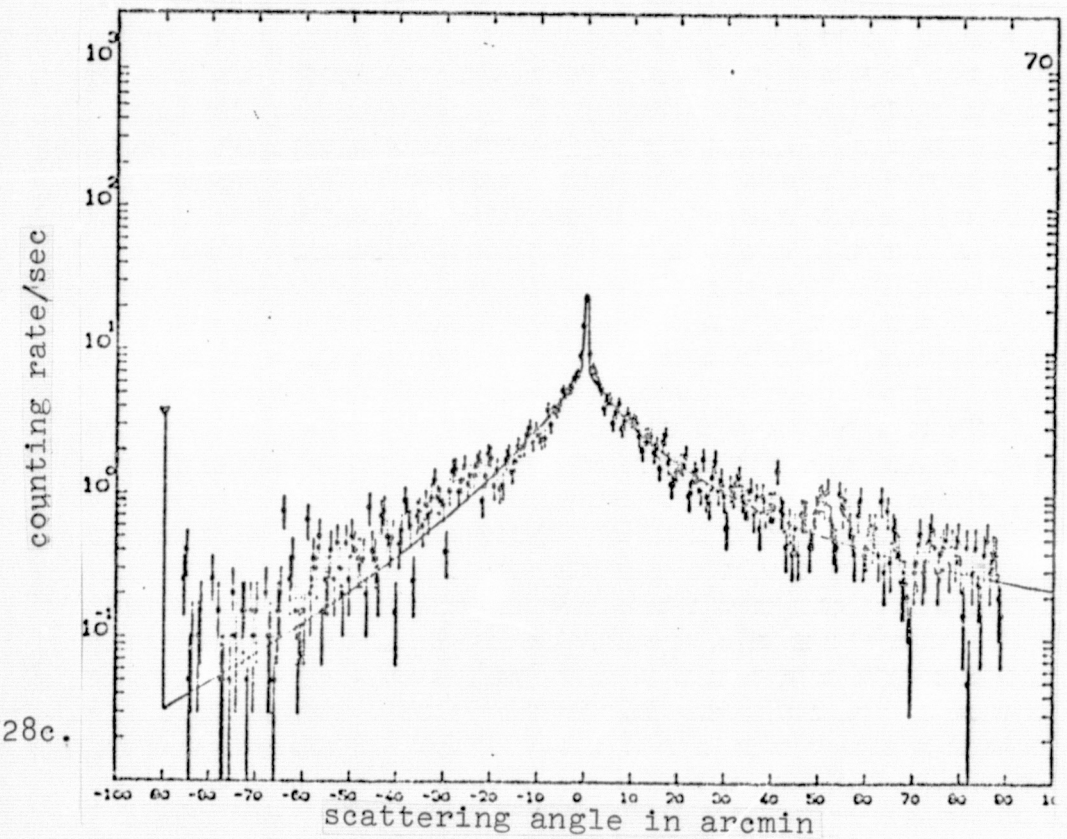

Figure 28c. $\lambda = 17.6\text{Å}, \alpha = 1.5^{o}$

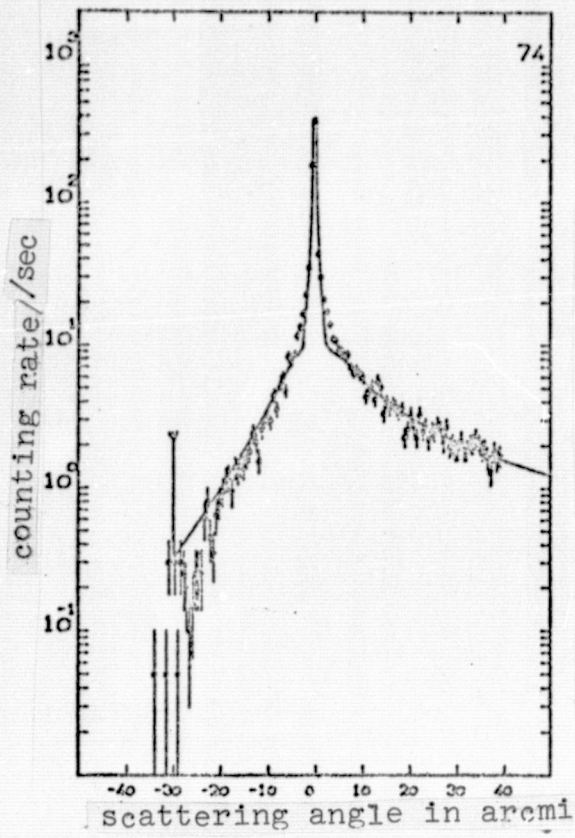

Figure 28d $\lambda = 13.3\text{Å}$, $\alpha = 0.5^{o}$

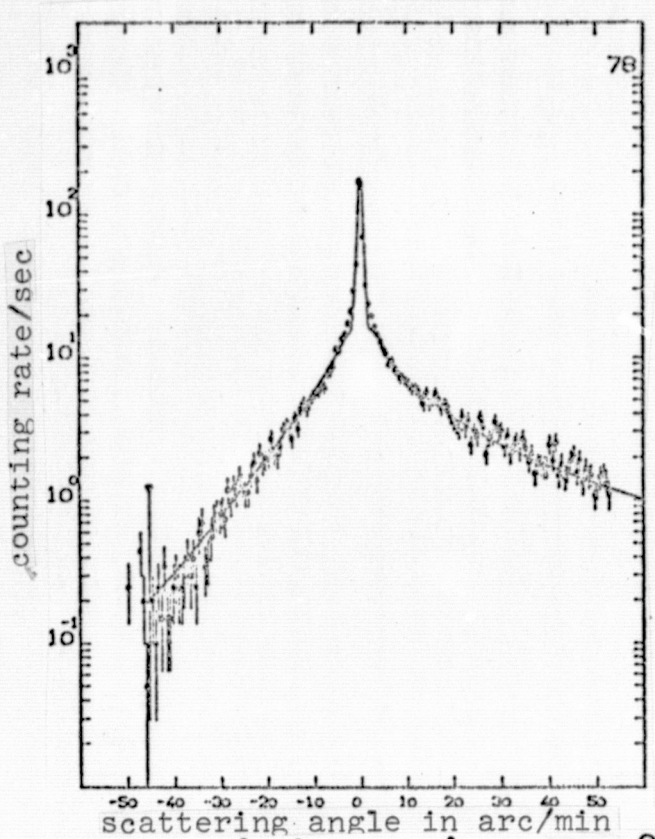

Figure 28e $\lambda = 13.3\text{Å}$, $\alpha = 0.75^{o}$

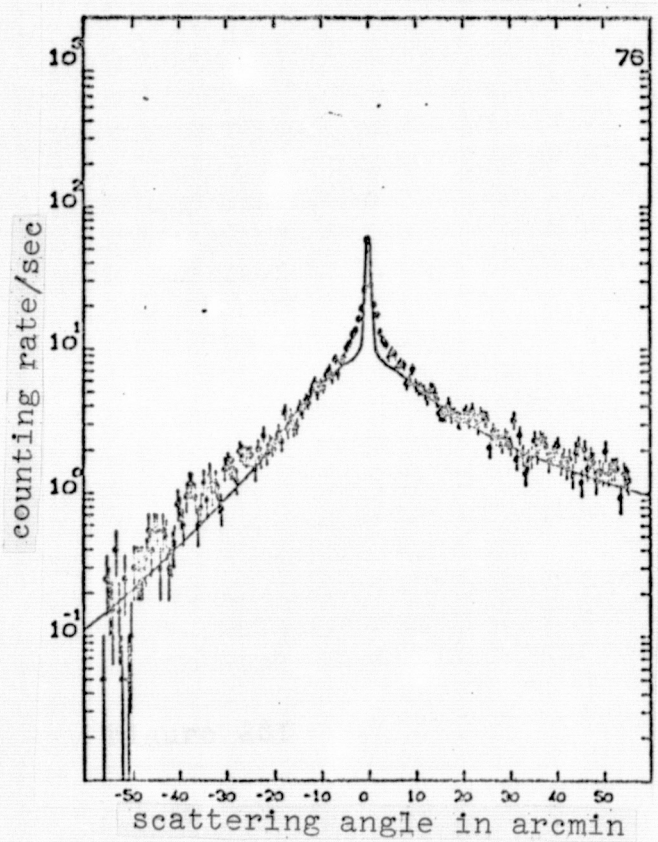

Figure 28f $\lambda = 13.3\text{Å}$, $\alpha = 1.0^{o}$

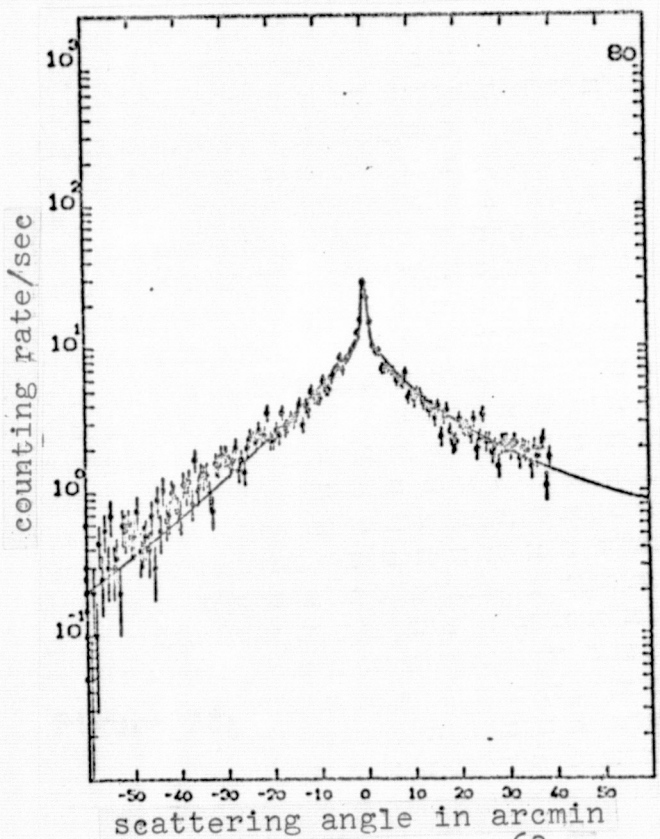

Figure 28g $\lambda = 13.3\text{Å}$, $\alpha = 1.25^{o}$

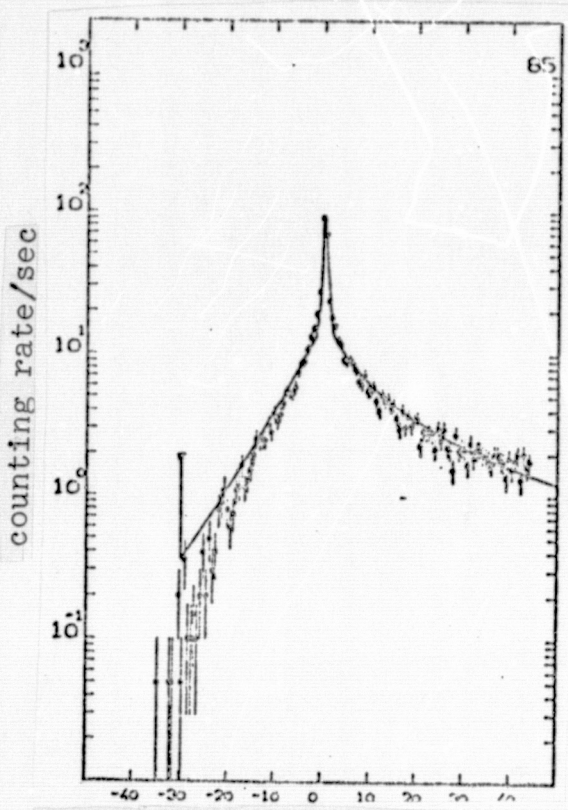

Figure 28h $\lambda = 8.3$Å, $\alpha = 0.5^{\circ}$

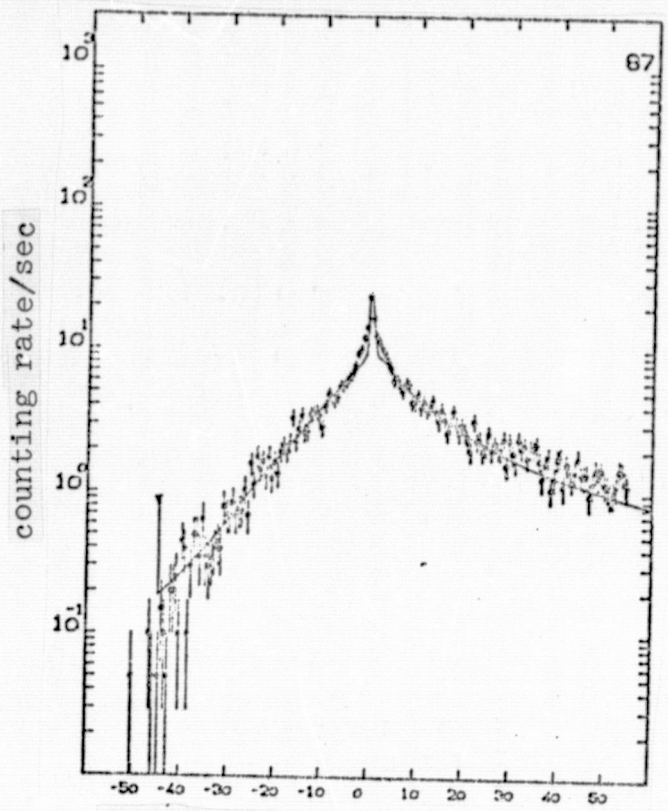

Figure 28j $\lambda = 8.3$Å, $\alpha = 0.75^{\circ}$

theory does not include multiple scatterings and shadowing effects. For small grazing angles the probability that the outgoing wave hits the surface again increases significantly, in particular, if the outgoing wave is almost parallel to the surface ($\varphi \to -\alpha$). Multiple scatterings may be neglected for grazing angles above 0.5° as shown by the measurements; this holds for the scattering distribution, but not for the reflectivity, as will be shown in Section 4.9.

4.5. Dependence of the Scattering on the Surface Treatment /75

Difficulties appear during polishing at the edges. Impurities and fresh polishing material that may get under the polishing tools result in increased roughness. On the other hand, the pressure exerted by the tools at the edge is different with the result that the exact form of the mirror is not maintained at the very edge. Thus, one plans for an overshoot which is then separated after the

polishing has been finished. In order to avoid any damage to the /76
mirror surface by this separation procedure, it is protected by
a varnish layer.

We have tested three of the kanigen samples of about the same quality [34, 37, and 39] for the consequences of the varnish and acid treatment for the scattering behavior. Figs. 29 a to d show the results of the treatment with respect to scattering. The untreated and dustfree stored sample 33 shows no change in the scattering behavior within the limits of the measuring accuracy; the two measurements were separated by about a month. Sample 34 was covered with blue varnish, and the varnish was then removed two weeks later with the aid of acetone and ether. The scattering increases by about 50%. Sample 39 was treated with some other type of varnish (0576). Again, the scattering increased, this time by 30%. Sample 37 was similarly treated with 0576. The sample was protected and then put for 30 minutes into an acid bath; the varnish was then finally removed in the same manner as with sample 34. Again, the scattering increase was about 30%. Since the surface that must be protected in the case of the telescope is only about 5% of the total mirror surface, the varnishing changes the scattering behavior of the telescope by less than 1%.

4.6. Two-dimensional Scattering Distribution /77

The theory of scattering states that the width of the scattering distribution in the meridional direction, that is, in the plane of incidence, is larger by a factor $(\sin \alpha_1)^{-1}$ than the distribution in the sagittal direction, that is, perpendicular to the plane of incidence; see Eq. (29). In order to test this theoretical result, we have measured the scattering distribution in the case of sample 38A in two dimensions: The collimator slits were replaced by diaphragms with circular openings (diameter 600 μ), and a circular diaphragm of the same diameter was mounted in front of the detector. The intensity distribution was then measured horizon-

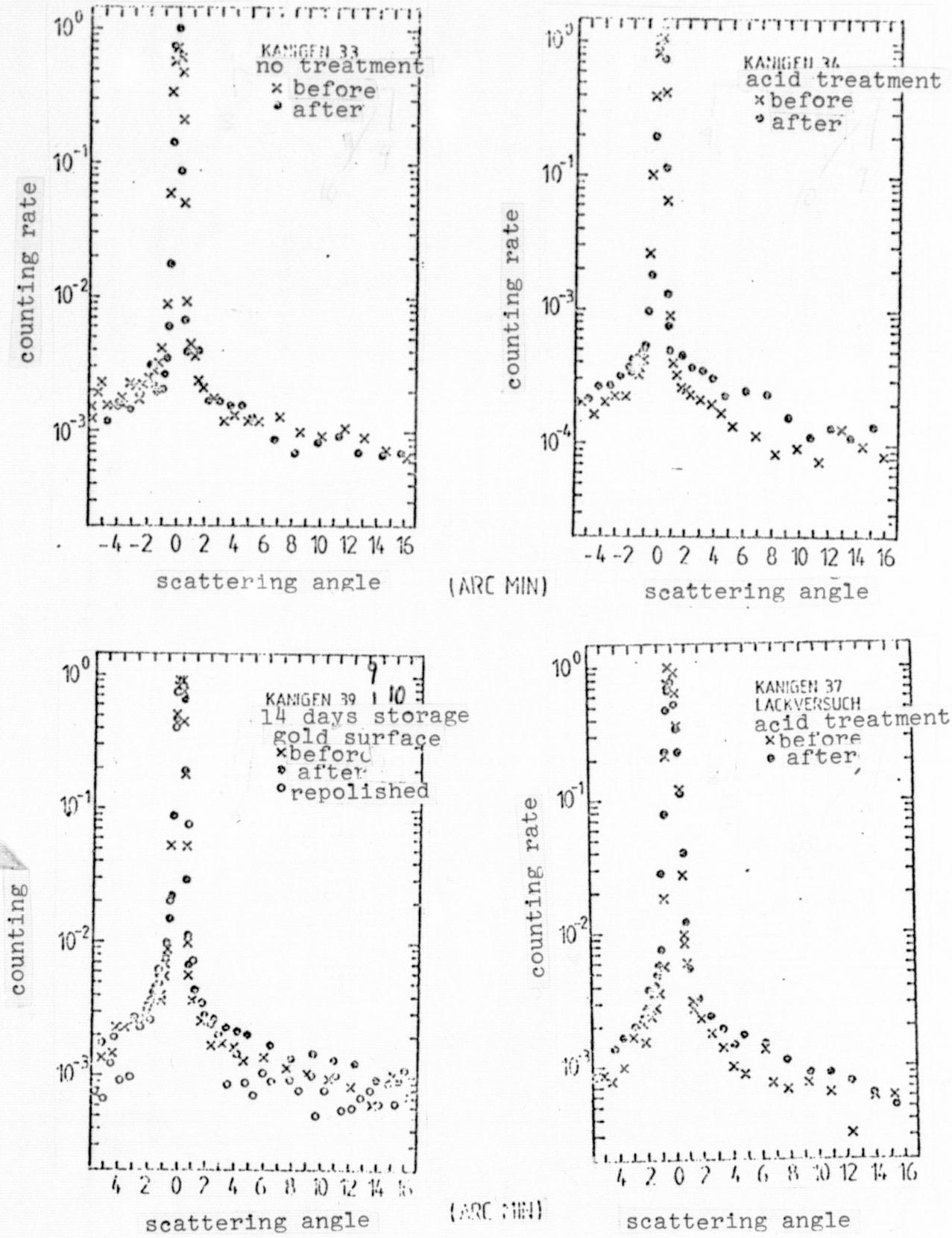

Figs. 28a to d. Scattering measurements with samples 33,34,39 and 37.

tally, that is, meridionally. Figs. 29 a to d show the results of these measurements in the form of height profiles: Each cross-over point corresponds to a measuring point in the neighborhood of the core. In the halo case, however, only every tenth cross-over point in meridional direction corresponds to a measuring point; in between we have used a linear interpolation.

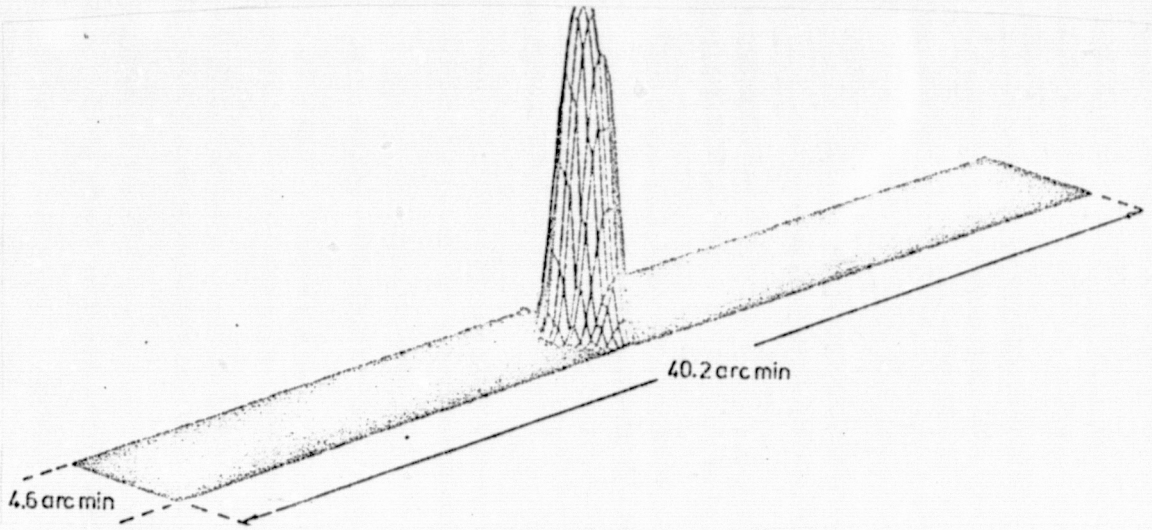

Figure 29a. Intensity distribution of the direct ray in the plane detector: $\lambda = 17.6\text{Å}$

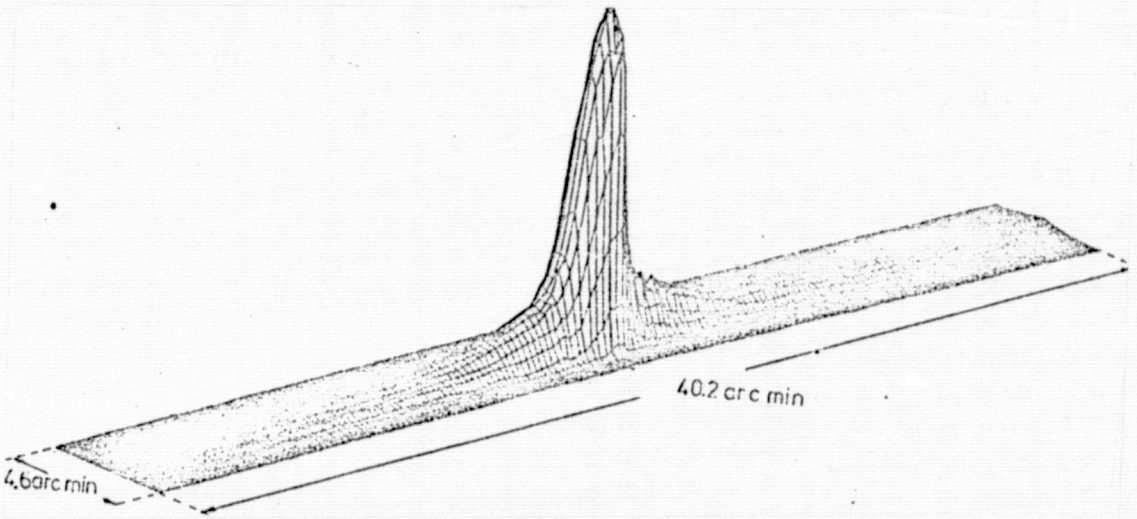

Figure 29b. Intensity distribution of the reflected ray in the plane of the detector, sample 38A $\lambda = 8.3\text{Å}, \alpha = 0.5^{o}$. Plane of incidence is in the longitudinal direction and perpendicular to the plane of the profile.

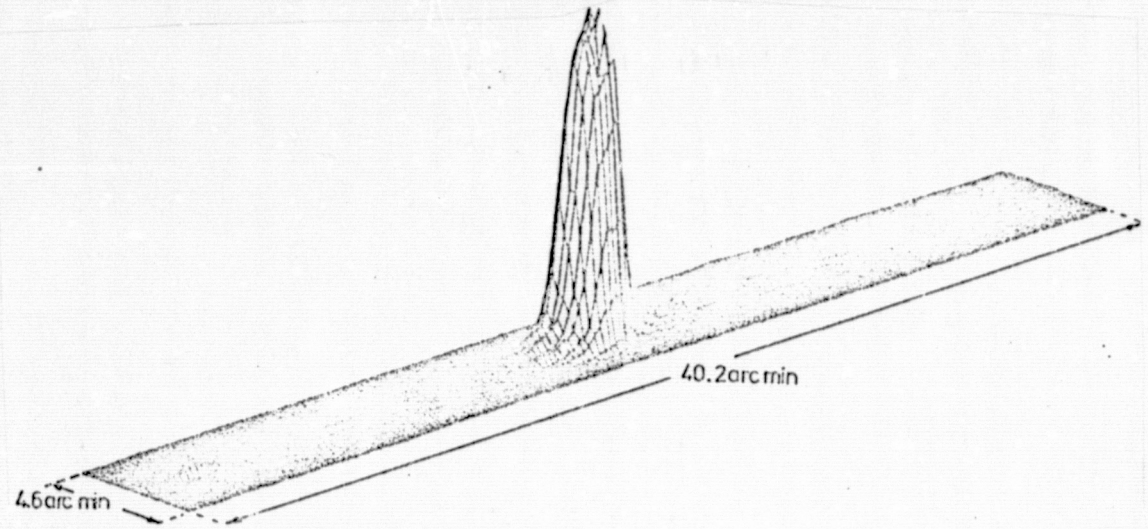

Figure 29c. Intensity distribution of the reflected ray in the plane of the detector, sample 38A, $\lambda = 17.6$Å, $\alpha = 0.5^{o}$. Plane of incidence as in Fig. 29b.

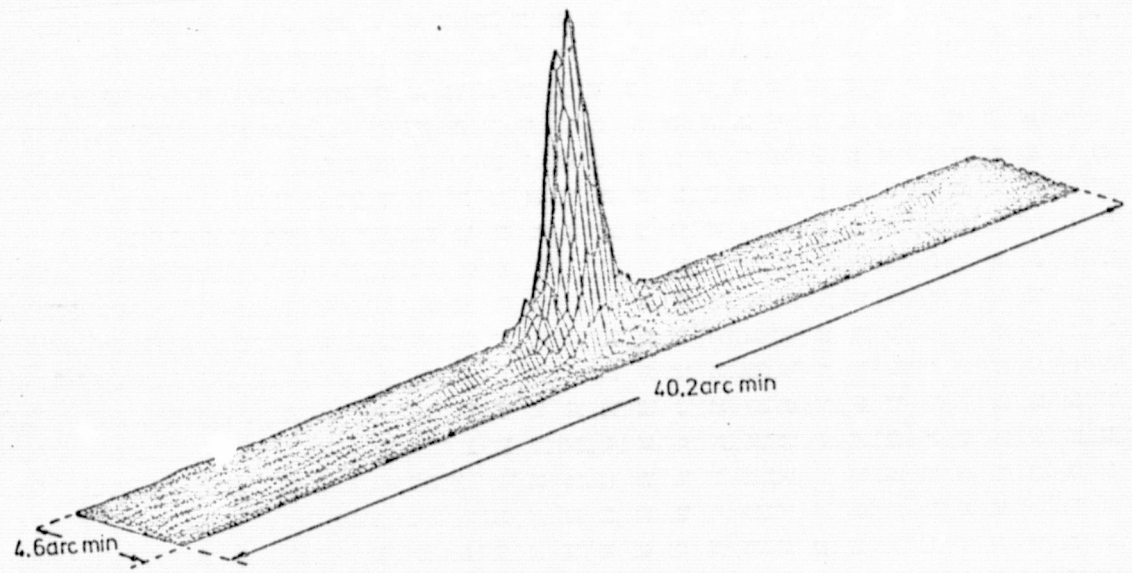

Figure 29d. Intensity distribution of the reflected ray in the plane of the detector, sample 38A, $\lambda = 17.6$Å, $\alpha = 1.0^{o}$. Plane of incidence as in Fig. 29b.

The mountains in the intensity distribution show the expected form: The specularly reflected component has the same form as the direct ray (plane mirror), while the scattering halo is only spread in the meridional direction; in the perpendicular direction no spreading is seen by comparison with the direct ray. The energy flux density is shown in Figs. 29 a to d in linear measure (in arbitrary units). The preference for scattering in the meridional direction is particularly clear in Fig. 29b.

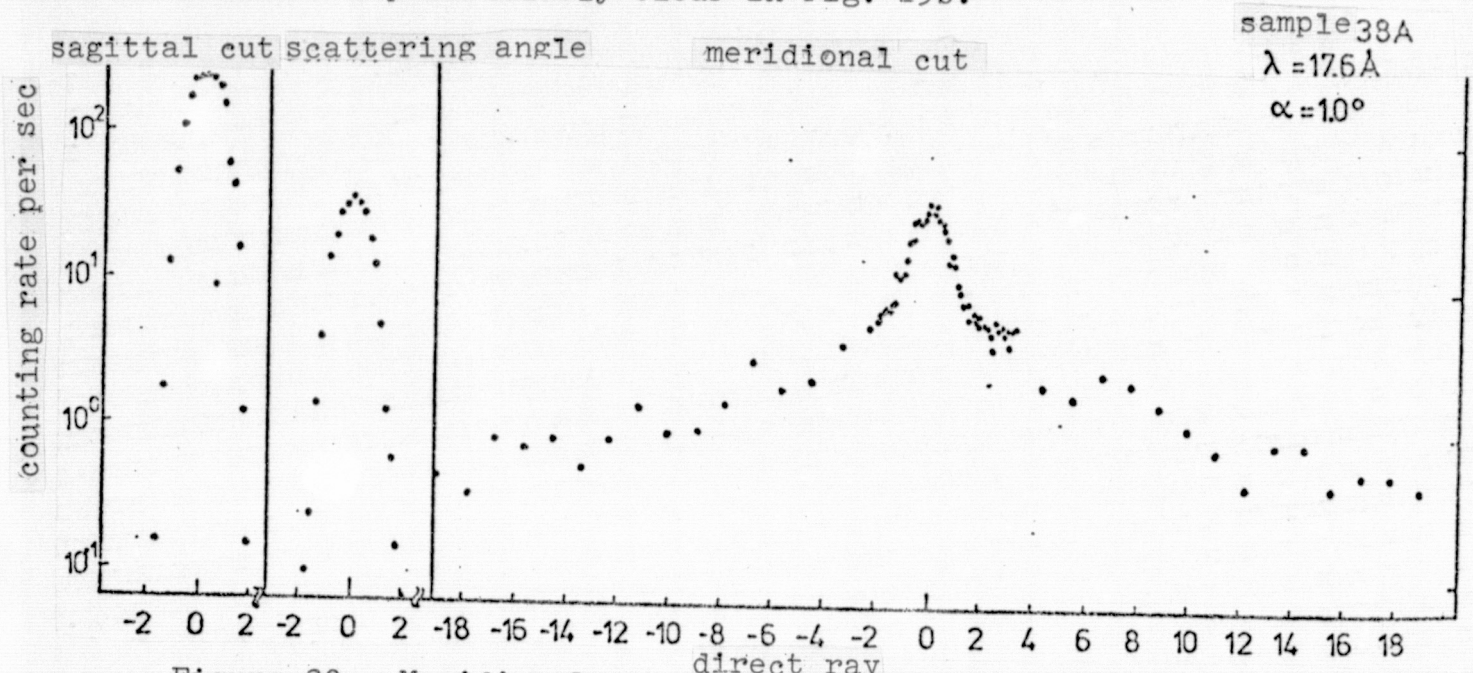

Figure 30. Meridional and sagittal cut through the point image function, sample 38A, $\lambda = 17.6\text{Å}$, $\alpha = 1^{\circ}$. /80

The behavior of the scattering distribution in the meridional direction allows to determine the scattering amplitude A from the relation: $\langle S S^{*} \rangle = I_{\text{Spekular}}(\varphi, \gamma) + A \cdot I_{\text{Halo}}(\varphi, \gamma)$ where $I_{\text{Halo}}(o,o) = 1$. From the fact that the intensity distribution of the reflected ray in the sagittal direction has, within 0.5 arcsec, exactly the same width as the direct ray, even where the intensity has decreased to 10^{-3} of the maximum value (see Fig. 30), we find for a known scattering width in the sagittal direction that the scattering distribution in the γ-direction is less than 30 arcsec. The theoretically expected scattering width is by a factor between 3 and 6, depending on the grazing angle, below this limit.

4.7. Scattering Measurements on Replica Samples /81

The replica method is particularly attractive for the mass production of highly polished mirrors. The method consists of copying several mirrors from a highly polished negative original. The original obtains a thin layer (200 Å) of gold on a layer of chromium oxide that increases the adhesion between gold and carrier. This carrier is last added, either as a preformed piece, to be glued on with an intermediate layer of epoxy (EXOSAT), or else, the carrier material is applied electrolytically. In the latter case, the epoxy layer is unnecessary. The advantage of this method is self-evident in that the expensive polishing is practically avoided, since many copies can be made from one original.

The first method was tested with three plane samples: Two copies of an optimally polished zerodur sample were made on equally well polished zerodur mirrors. The copies were of the same quality as the original, in fact, the copy on sample 1 had even a smaller roughness than the original. This is understandable since in order to dimension out the original it had to obtain a layer of gold in order to achieve a measurable reflectivity at 1.5°. Fig. 31 shows the results for the third sample. Here, the carrier is a coarsely polished aluminum mirror which had been etched prior to copying. While the original at wavelengths of 13.3 and 8.3 Å had 2 and 3% integral scattering contribution, respectively, the replica sample showed scattering contributions of 39.7 and 56.7%, respectively, corresponding to a roughness of 26 Å. The scattering distribution is well represented by a Lorentzian /83 shape (solid line in Fig. 32) with its width corresponding to an autocorrelation length of between 28μand 22μ. These measurements show that the replica method at this time only then yields good results with epoxy application, if the carrier and the original are of comparable quality. This,however, defeats the purpose of the replica method.

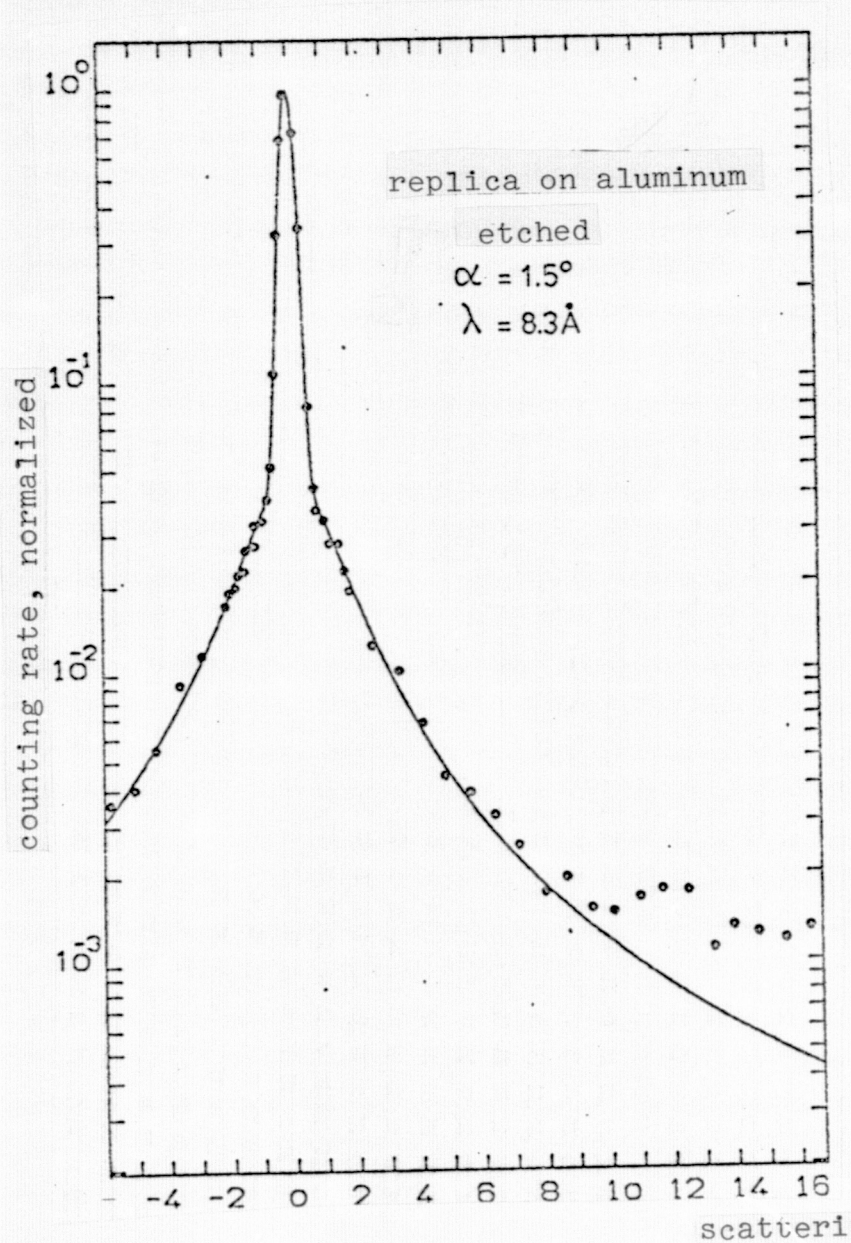

Figure 31a. Scattering distribution for sample 3. $\lambda = 8.3\text{Å}$, $\alpha = 1.5^\circ$

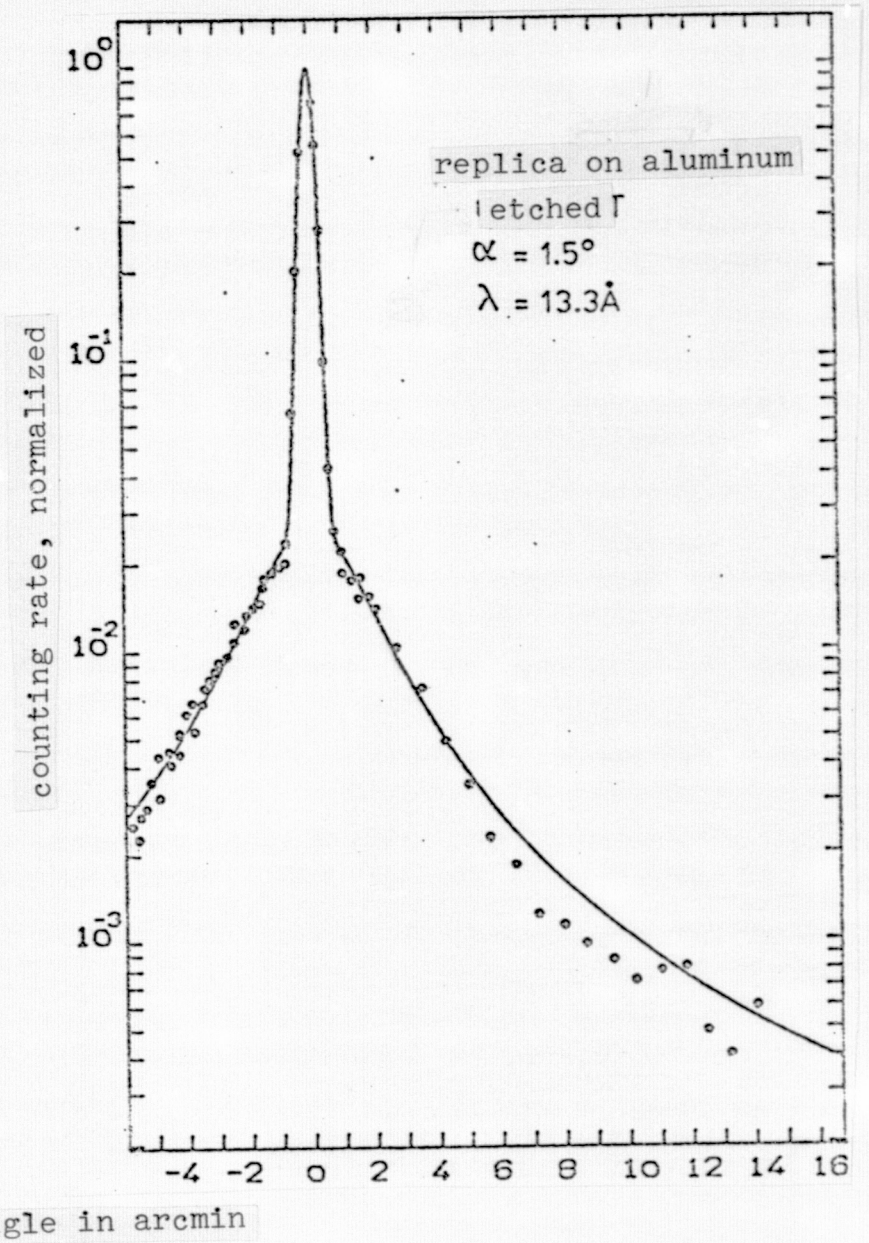

Figure 31b. Scattering distribution for sample 3. $\lambda = 13.3\text{Å}$, $\alpha = 1.5^\circ$

4.8. Dependence of the Scattering on the Polishing Direction

The scattering theory presented in Section 3.4 assumes that the roughness of the mirror is the same in all directions and, in particular, that the autocorrelation function depends only on $\tau = \sqrt{\Delta x^2 + \Delta y^2}$. The normal polishing methods indeed makes sure that there is uniformity in all directions. Thus, in the case of perpendicular incidence, the rotational symmetry is maintained.

Schroeder and Klimasenki [36] made the first study of the /84 influence of a preferred direction in the polishing on X-ray scattering in the case of grazing incidence. At a wavelength of 1.9Å and a grazing angle of about 10 arcmin, the authors found a slightly increased scattering in the case that the direction of polishing is perpendicular on the direction of incidence. The measurements were carried out at atmospheric pressure. Since at such small grazing angles, shadowing effects are very important, the results of these authors cannot be extrapolated to the soft X-ray range.

We have investigated the dependence of the scattering on the polishing direction at 8.3 Å and for grazing angles between 0.5 and 2°. The mirror we used was a well polished sample with kanigen on aluminum, with the final polishing carried out in one direction. This preferred direction is easily recognizable in the Normarski /85 interference microscope (Fig. 35c). The table below shows the results of our measurements. The numbers given for the scattering contribution refer to the measuring range between -18 and +18 arcmin; this means that the resulting values for g and σ represent a lower limit. The scattering depends clearly on the polishing direction: If the polishing direction is perpendicular, the scattering contribution is 2-3 times the amount of the parallel arrangement. In the former case one finds from the scattering contribution a roughness of (7.0 ± 1.6) Å, in the latter (11.0 ± 1.0) Å. The scattering-theory result that in the case of small scatter-

ing contributions the roughness σ is obtained from the relative scattering component I_{Str} as $\sigma = \frac{I_{Str}\,\lambda}{4\pi \sin\alpha}$ had been derived in Section 3.4 independent of the autocorrelation function. Hence, the result must be equally valid in the case of a preferred direction of polishing. The difference in the roughness can then be explained by assuming that perpendicular to the polishing direction the roughness has a smaller wavelength than as in the parallel direction. The higher spatial frequencies of the roughness correspond to larger widths in the corresponding scattering distribution. If the polishing direction is perpendicular to the plane of incidence, the intensity is scattered into larger angular ranges with the result that a larger percentage falls outside of the measuring range. This then leads to the erroneous result that in the case of perpendicular direction the roughness is smaller.

Polishing direction	Grazing angle	Scattering contribution g	σ(Å)	
⊥	1.025°	0.047	0.048	8.1
	2.010°	0.094	0.099	5.9
∥	0.500°	0.025	0.025	11.9
	1.025°	0.071	0.074	10.0
	2.010°	0.297	0.353	11.2

The image contrast of an X-ray can therefore be increased by choosing a large rotational speed with respect to the axis of the telescope during the final polishing process by comparison with the axial displacement speed.

4.9. Influence of the Roughness on the Integral Reflectivity

Our scattering theory treated the reflectivity as independent of the roughness of the mirror samples. One suspects, however,

that the reflectivity does in reality not only depend on the roughness, but also on the chemical properties of the surface, such as the possibly present monomolecular layers of foreign matter [11]. There are currently very few measurements of the reflectivity available in the soft X-ray range, and the results show significant differences. For instance, the values for the decrement of the refractive index vary between authors - von Ershov et al. [15], Lukirskii et al. [27, 28], Costa et al. [11] - by more than 100%. Part of the differences is the fact that not always a distinction is made between specular and integral reflectivity; we shall understand by reflectivity in the following the integral reflectivity. We shall not attempt to investigate the discrepancies; this would have to be done with the aid of a monochromator and include a chemical analysis of the surface. Instead, we shall discuss the dependence of the reflectivity on the roughness on the basis of samples 38A and 39B, comparing reflectivity measurements with a well polished surface by means of the monochromator [32] and with theory.

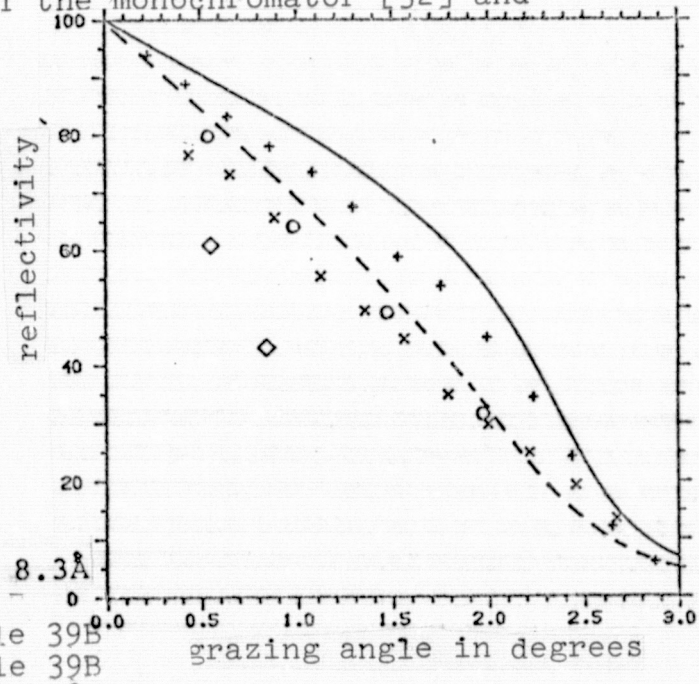

Figure 32a. Reflectivity for $\lambda = 8.3$ Å

x = specular reflectivity, sample 39B
o = integral reflectivity, sample 39B
◇ = integral reflectivity, sample 38A
\+ = Measurement Rausch
—— = theoretical, gold
– – = theoretical, nickel

As we were able to show in Section 4.4., shadowing effects and multiple scattering does not have to be taken into account when the scattering distribution is computed. However, as shown by Figs. 32 a to e, these effects influence the reflectivity. The shadowing effects make the mean microscopic grazing angle differ from the macroscopic, that is, the former shifts to larger angles with increasing roughness, and this in turn results in a decrease of the reflectivity. The case of multiple scattering obviously influences the reflectivity. The decrease is clearly seen for samples 38A and 39B by a comparison of the measured and theoretical reflectivities. /88

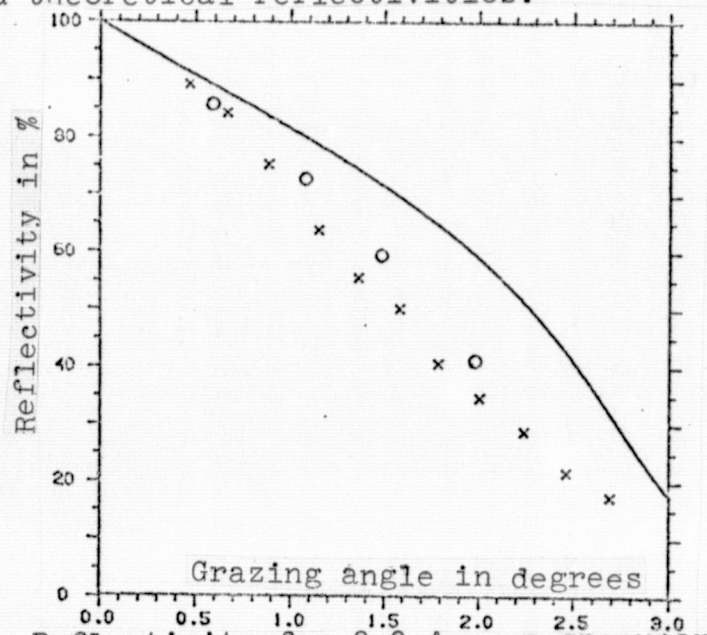

Figure 32b. Reflectivity for 9.9 A. x = specular reflectivity, sample 39B
o = integral reflectivity, sample 39B
—= theoretical, gold

Figures 32 a to e compare the theoretical reflectivities for gold (____) and nickel (----) with experimental determinations by Rausch [32] (+++) and those for samples 38A and 39B. The theoretical values are all above the experimental ones. Whereas the measurements by Rausch with the monochromator are fairly close to the theoretical values, except at 44.8 Å, the reflectivitities of samples 38A and 39B are as much as 50% below the theoretical

values.

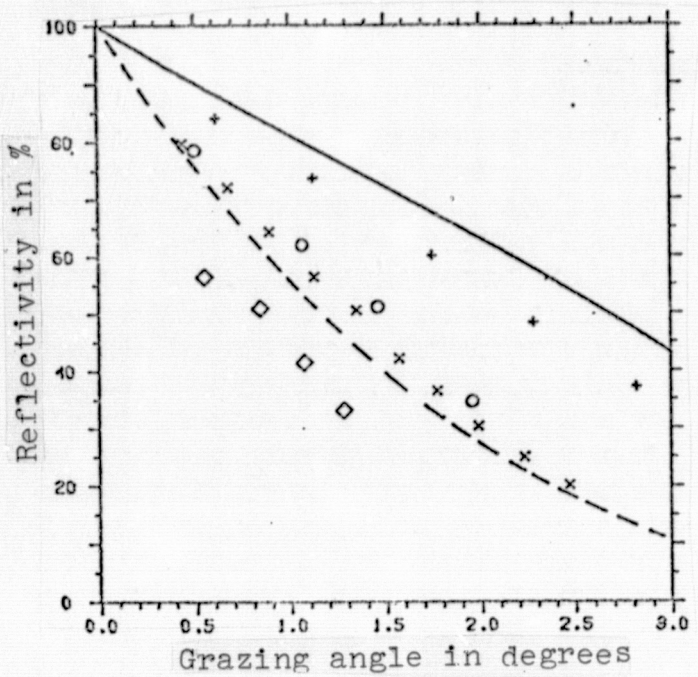

Figure 32c. Reflectivity for 13.3 Å, x = specular reflectivity, o = sample 39B
◇ = integral reflectivity, sample 39B
+ = integral reflectivity, sample 38A
—— = Measurement Rausch
– – = theoretical, gold
theoretical, nickel

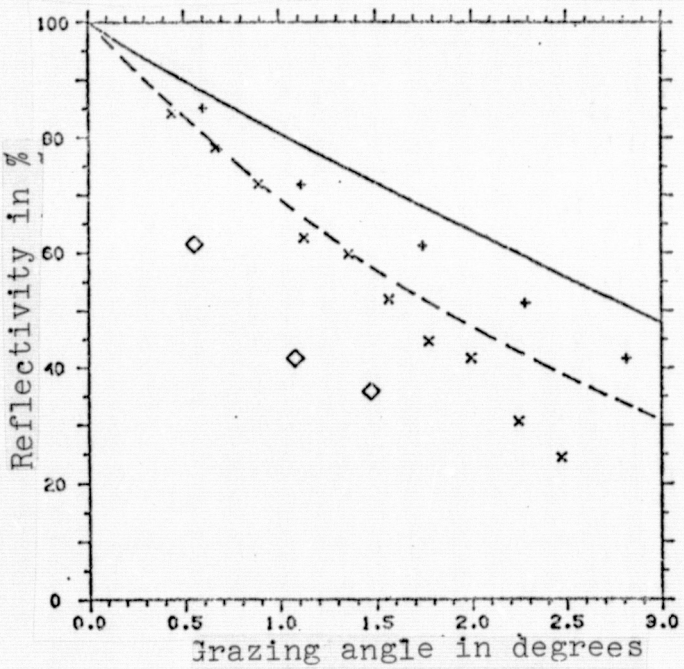

x = specular reflectivity,
◇ = sample 39B
integral reflectivity,
+ = sample 38A
Measurement Rausch
—— = theoretical, gold
– – = theoretical, nickel

Figure 32d. Reflectivity for 17. 6 Å.

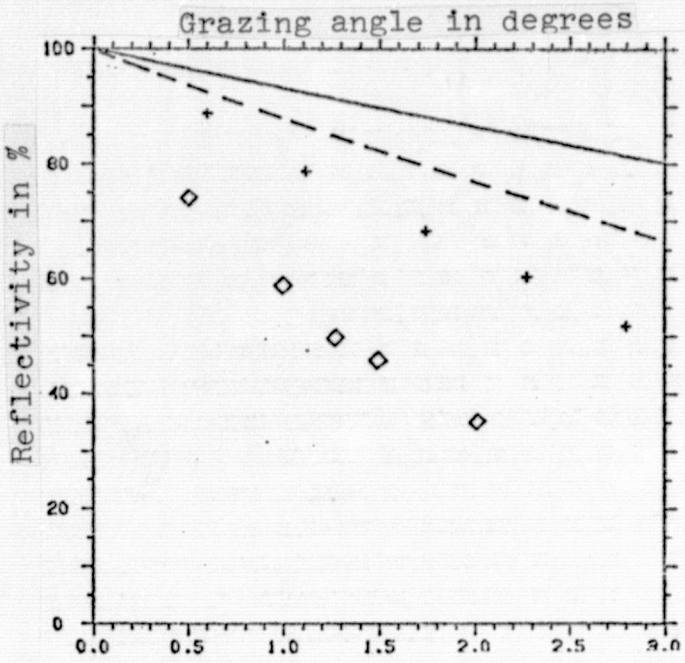

Figure 32e. Reflectivity for 44.8 Å. = integral reflectivity,
◇ = sample 38A
\+ = Measurement Rausch
—— = theoretical, gold
– – = theoretical, nickel

If one forms the ratio of the measured reflectivity and the theoretically expected value, a linear dependence of the grazing angle is obtained:

$$Q(\alpha,\lambda) = \frac{R_{Mess}(\alpha,\lambda)}{R_{theor}(\alpha,\lambda)} = 1 - A(\lambda)\alpha$$

The quantity A was determined from the relation $A = \frac{n - \sum Q(\alpha_i)}{\sum \alpha_i}$ where n is the number of points. The influence of the shadowing effects and of multiple scattering increases with increasing grazing angle. Samples 38A and 39B lead to the following values for A (λ)

	Sample 38A				Sample 39B			
λ(Å)	8.3	13.3	17.6	44.8	8.3	9.9	13.3	17.6
A/Grad	0.49	0.22	0.30	0.32	0.21	0.11	0.22	0.19

The portion of the incident intensity which is lost due to the

roughness of the surface, that is the difference R_{theor} - R measured, is then defined by $A(\lambda)R_{theor}(\alpha,\lambda)\cdot\alpha$.

It is surprising that neither Q nor the difference R_{theor} - $R_{measured}$ vanish for $\lambda \to 0$. The reason is possibly the uncertainty in the optical constants for large wavelengths; in addition, the resolution of the proportional counter is insufficient at the low photon energy.

4.10. Comparison Measurements of the Roughness

In view of the significant experimental effort required by scattering measurements in the X-ray range, other measurement techniques for roughness should be explored. These measuring techniques should ultimately provide values for small-angle scattering in the X-ray range. In order to avoid any disturbance of the polishing process of the telescope, a technique is preferable which allows the mirror to remain in the polishing device.

J. M. Bennet [3] gives an extensive survey of measuring techniques for surface roughness and wave-type patterns. We shall in the following discuss four such methods; the last one actually is not yet listed in reference [3].

PERTHOMETER

The perthometer is a measuring device which follows mechanically the surface with a diamond and translates height fluctuations/92 by means of induction into electrical voltage fluctuations. The result is then recorded (fig. 33). The height profile is used to determine the height distribution and the autocorrelation function; the procedure is shown for a 1μ-diamond lapping sample in Fig. 33. Since the diamond visibly etches the surface, in particular, on a soft gold surface, this type of quantitative evaluation makes only sense in the height range below 50 Å. The lateral resolution is

about 1μ. In a qualitative sense it is possible to compare samples down to about 10 Å, except in the case of soft surfaces, such as gold.

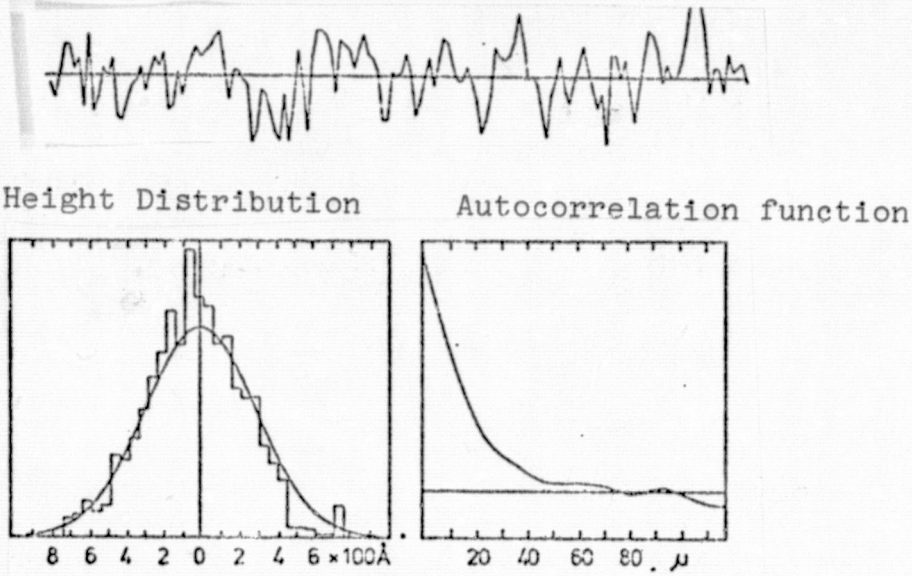

Figure 33. Height profile, height distribution, and autocorrelation function of a 1μ - lapped sample.

The recording of 20 measurements at various positions and in different directions for the sample 38A resulted for the standard deviation σ and the maximum deviation R_t in the following values:

$$\sigma = (112.0 \pm 17.3)\text{Å}, \qquad R_t = (838.0 \pm 168.6)\text{Å}$$

An individual measuring interval was 1 mm. Spatial frequencies below $\frac{2\pi}{250\mu}$ were suppressed. The result for the standard deviation of the sample 38A is in agreement with the determination of the roughness from scattering measurements as 106 Å. /93

Nomarski-Interference Microscope

A second method for the evaluation of surface roughness, in particular in the range $\sigma \leq 50$Å, makes use of the Nomarski interference microscope, a twin-beam polarization interference microscope [30]. Linearly polarized, monochromatic light is separated

by a Wollaston prism into two mutually perpendicularly polarized beams (fig. 34). The two beams suffer different phase changes upon transmission and reflection at the object. If the beams are brought back together again and interfere, the image reflects the inhomogeneities of the object, although a quantitative reduction of the data is not possible. P. A. J. de Korte and R. Laine [23] attempted to obtain, from interference microscope pictures, data on the lateral structuring in the case of highly polished /95
X-rays mirrors. The Nomarski method allows to obtain a three-dimensional impression of the microstructure of the surface and to compare samples in a qualitative manner.

Figures 35 a to d show pictures of the samples 38A, 39B, 50 and 12 in the differential interference contrast according to Normarski. In a qualitative sense, the difference between the samples 38A and 39 is obvious. The high contrast of the scratches in the case of sample 38A is evidence for the depth of the scratches. If a linear scan is chosen across the sample and if the clearly visible scratches are counted that cross that line, then a scratch is found every about 5μ , that is, we have a correlation length $T = 5\mu$. This value is for obvious reasons smaller than the one obtained from scattering measurements (10.0 μ): flat and, for this reason, low-frequency uneven areas are under represented in the estimate. However, the two results agree as to the correct order of magnitude.

Samples 39B and 50 show approximately the same contrast, and this reflects the approximately equal results of the scattering measurements. The preferred direction during the final polishing procedure in the case of sample 50 is clearly visible in the Nomarski picture.

A picture with floated glass (sample 12) is added for com-/96
parison. The contrast is decreased again at places with respect

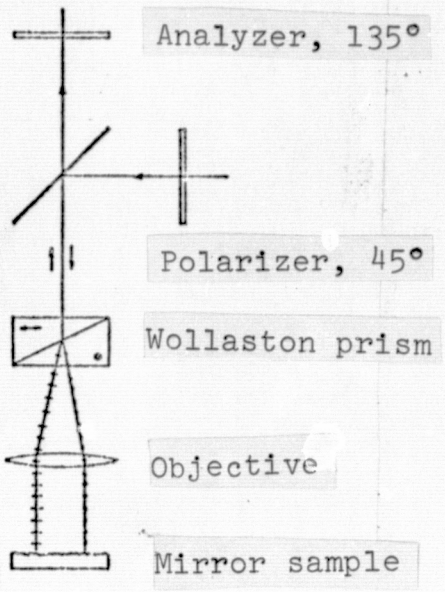

Figure 34. Basic setup of a Nomarski microscope

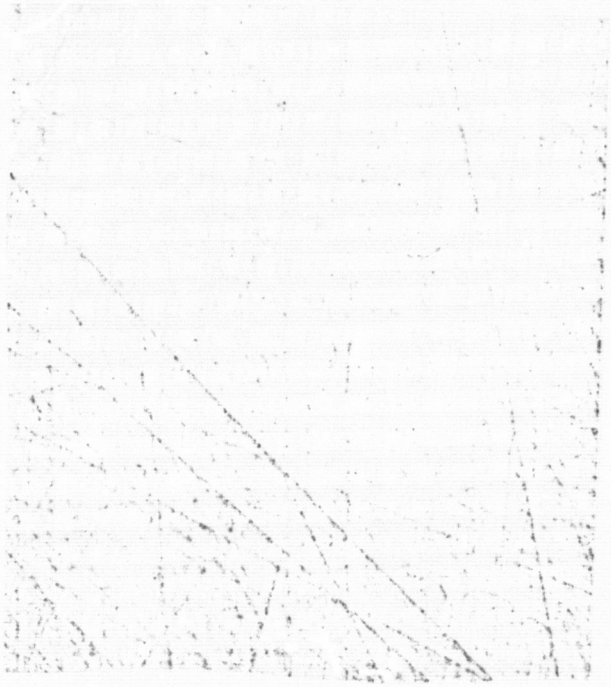

Figure 35a. Sample 38 A 20μ

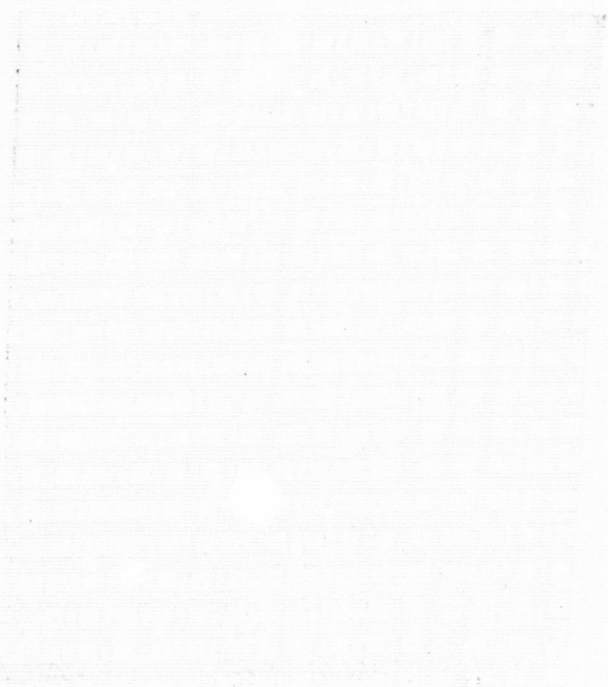

Figure 35b. Sample 39B 20μ

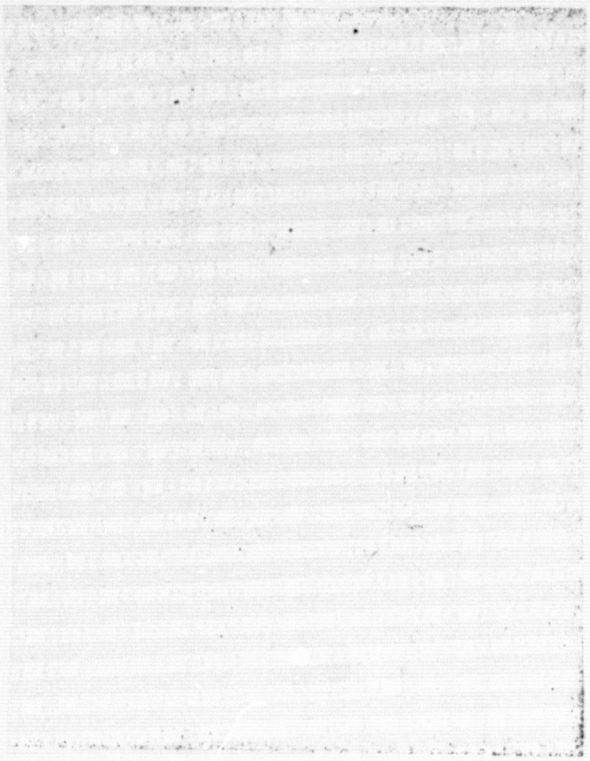

Figure 35c. Sample 50 20μ

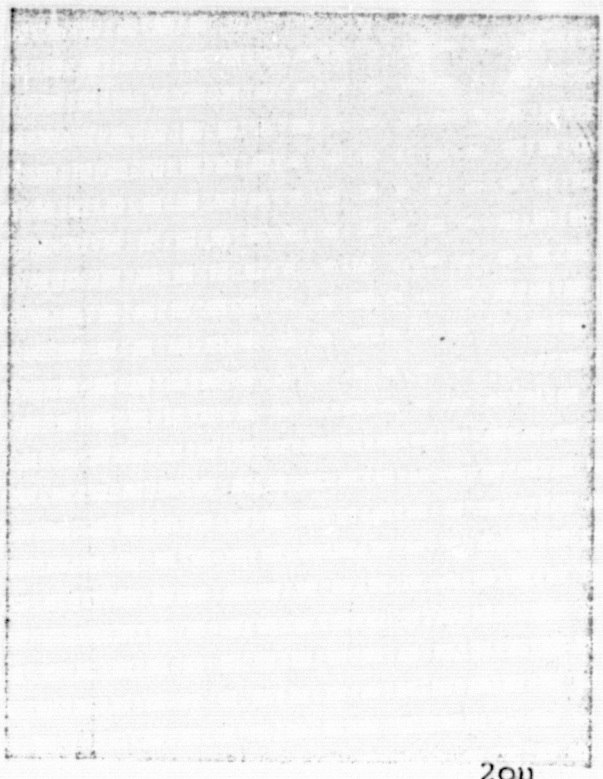

Sample 35d. Sample 12 20μ

Nomarski pictures, made by the Zeiss Company in Oberkochen

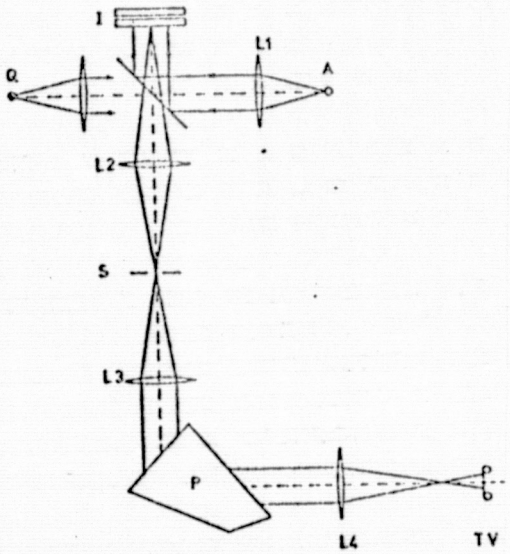

Figure 36. The principle of the FECO method.

samples 39B and 50. On the other hand, significant disturbances are visible that cannot be described with the aid of a statistical theory. It is for this reason not surprising that measurements with the glass samples yield so different results. The results

simply depend on the number of disturbances that happen to be present on the illuminated portion of the mirror surface.

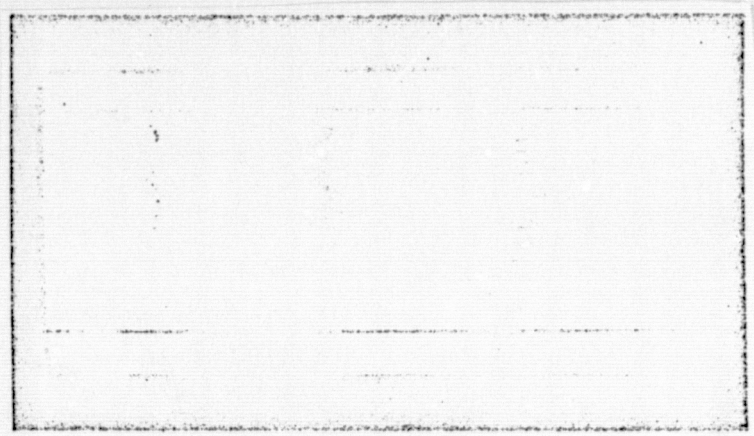

Fig. 37a
FECO image of sample 38A

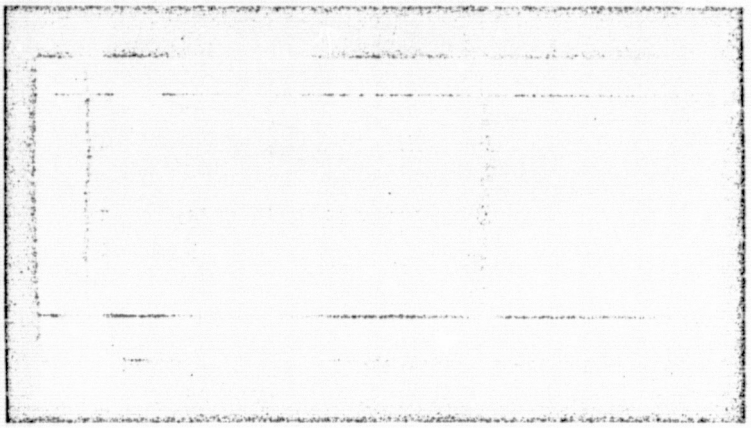

Fig. 37b. FECO image of sample 50. Slit perpendicular to the direction of polishing.

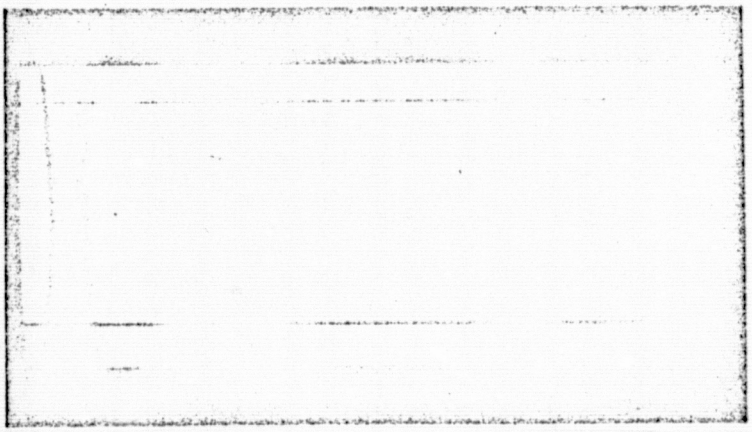

Figure 37c. FECO image of sample 50. Slit parallel to the direction of polishing

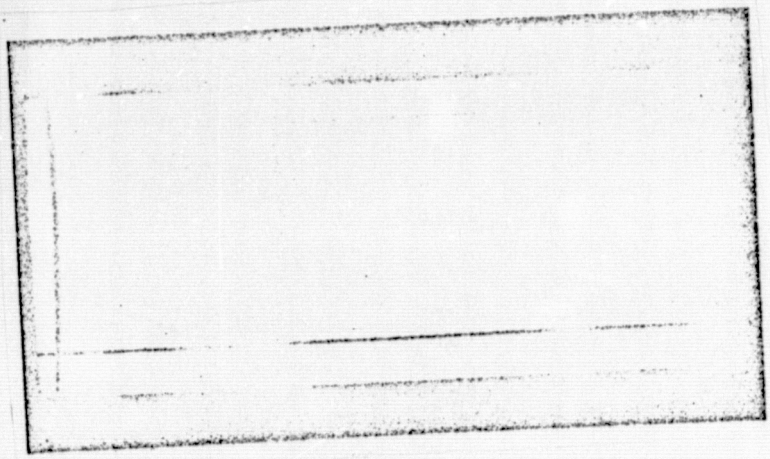

Figure 37d. FECO image of Sample 39B.

THE FECO METHOD

The method described in the literature by the term FECO (fringes of equal chromatic order) uses multiple interference [3] and was developed to the point that roughnesses of only a few Å can be evaluated (lateral resolution 2μ). White light is, via semi-transparent plate, mirrored into an interferometer whose one mirror surface is the sample. A lense L_2 forms at the entrance slit of a spectrograph (L_3, P, L_4) an interference image.

An interference fringe pattern is thus produced in the image/98 plane of the spectrograph, and this pattern is recorded by the camera. In order to calibrate the height resolution, a line spectrum is entered on the semi-transparent plate from the left (Fig. 36). Fig. 37e shows the height amplification as a function of the position of the strip on the image. This calibration yields for the individual samples an average roughness of 80 Å (sample 38A), 10 Å (sample 50) both in perpendicular and parallel position, and 15 Å (39B). The resolution is not good enough to distinguish the correlation lengths perpendicular and parallel to the direction of polishing (Figs. 37 b and c); The correlation length is less than 1μ.

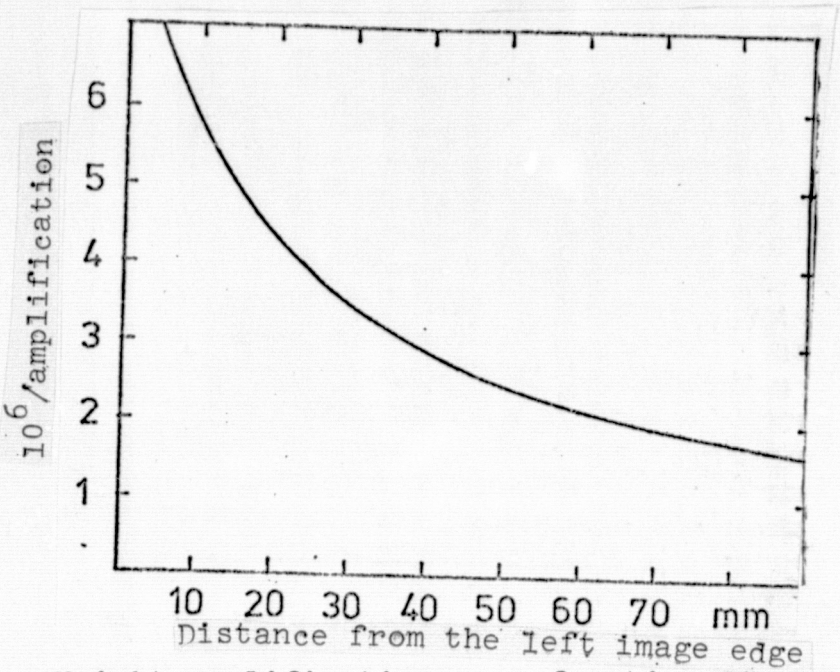

Figure 37e. Height amplification as a function of the position on the interference image.

DIRECT LIGHT ELECTRON INTERFERENCE MICROSCOPE /99

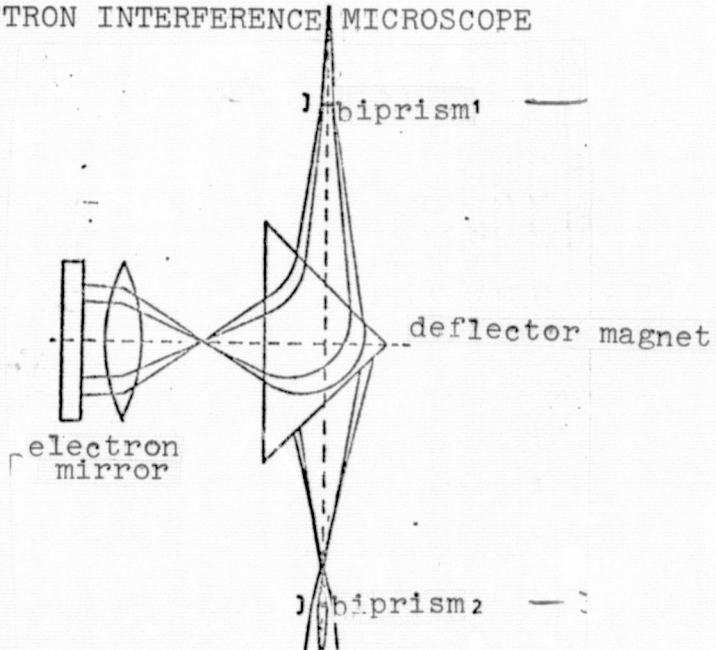

Figure 38. The principle of the direct light electron interference microscope.

The ray path of the direct light interference microscope is similar to that of the Nomarski microscope (Fig. 38). However, in the case of electron interference, the interfering beams are spat-

ially separated on the object [26]: An electron beam is separated into two equal beams by a biprism. The two coherent beams reach the mirror sample via deflector magnet, and here they are reflected by means of an appropriate counter voltage. If the electrons are sufficiently monochromatic, and if the counter voltage is only a little above the accelerating voltage so that all electrons are reflected just in front of the mirror ($1\,\mu$), then a fringe pattern is produced by the subsequent superposition of the coherent electron beams. This pattern shows the form of the counter voltage just in front of the mirror surface and hence, provided there are no magnetic or electrostatic inclusions, the surface form itself. This method allows the measurement of height differences in steps /100 of 0.1 Å according to reference [26].

The method has been tested with sample 61: The surface profile was determined at 20 different positions, and the average roughness computed in the spatial frequency range between $\frac{2\pi}{1.5\,\mu}$ and $\frac{2\pi}{15\,\mu}$. Whereas scattering measurements produced in this frequency range a roughness of (2.54 ± 0.44) Å (see Section 4.3), the roughness obtained from the electron interference microscope pictures resulted in (3.2 ± 1.2) Å. Within the stated error limits, the two measurements are in agreement. Thus, we conclude that the measurement of surface roughnesses with the aid of the direct light electron interference microscope yields even for very small roughnesses of the order of a few Å, results that allow to predict correctly the scattering behavior via scattering theory.

The measurements with the direct light interference microscope were made by Dr. Lichte of the Institute for Applied Physics of the Univerisity Tubingen (Director Professor Mollenstedt).
I would like to thank the gentlemen for the successful collaboration.

5. SPECTROSCOPY WITH TELESCOPE AND TRANSMISSION GRATING /101

5.1. Introduction

Since thermal processes are responsible for the X-ray emission of many cosmic X-ray sources, one expects line emissions. Whereas the spectrum of a plasma at 50×10^6 K with an average element abundance shows isolated lines at 1.9 and 11.2 Å [W. H. Tucker and M. Koren [42]] that can be resolved with the limited resolution of a proportional counter, as was done first for Cyg-X-1 [34, 37], the resolving of lines at 5×10^6 K requires already a resolving power of about $\frac{E}{\Delta E} = 50$. This special resolving power can be achieved in a wide energy range by a combination of X-ray telescope and transmission grating [4, 5, 22]. We shall in the following discuss the image errors that appear in this combination and suggest means for their correction.

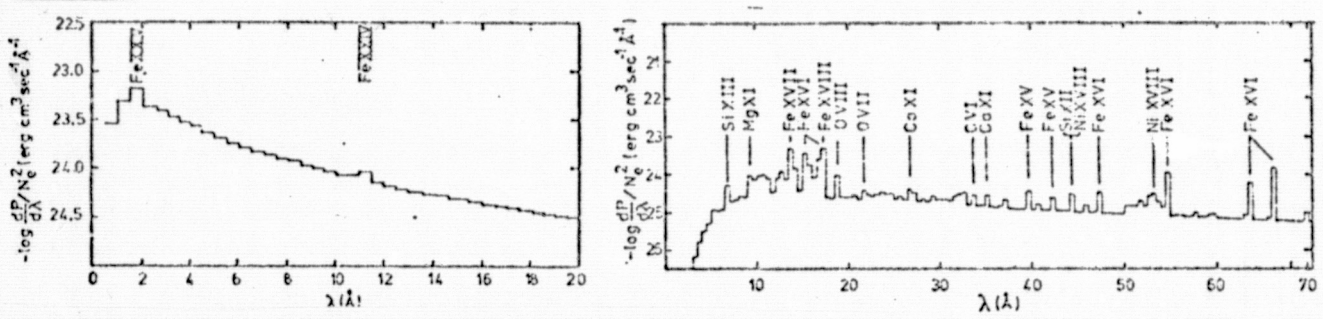

Figure 39. Spectrum of optically thin plasmas. a. T = 50×10^6 K. b. T = 5×10^6 K., according to Tucker and Koren [42].

5.2. Grating Errors and Correction Possibilities /102

Let us first consider the case where the transmission grating is arranged behind the telescope. We shall not take image errors of the telescope into account, instead we assume that the source is in the optical axis. Thus, the grating is illuminated convergently (Fig. 40); then the well-known errors of the third order appear. Their calculation and discussion uses Fermat's Principle: If the reference frame is defined such that the x-axis is identical with the optical axis and the yz-plane with the plane of the grating, then the focal point has the coordinates $P_o(D,0,0)$. P_1 $(0,y,z)$ is the locus of grating passage of the beam, $P_2(D,y',z')$ the observing point in the focal plane. Then, according to Fermat's

principle, the path

$$F(y,z,y',z') = \overline{P_1P_2} - \overline{P_oP_1} + m\lambda\int_o^y \frac{dw}{d(w,z)}$$

must be an extremum; d(w,z) is the distance between neighboring grating elements. If the path differences are expressed by the coordinates y, z, y', z' and if the derivatives with respect to y and z are formed then

$$\frac{z'}{D} = \frac{zyy'}{D^3} - \frac{zy'^2}{2D^3} + \frac{m\lambda}{D}\frac{\partial}{\partial z}\int_o^y \frac{dw}{d(w,z)} \qquad (49)$$

$$\frac{y'}{D} = \frac{1}{D^3}(3y^2y' - 3yy'^2 + z^2y' + y'^3) + \frac{m\lambda}{d(y,z)} \qquad (50)$$

We now introduce the coordinates of the Gaussian image point of the m^{th} order, that is, $\frac{y_G}{D} = \frac{m\lambda}{d_o}$ and $\frac{z_G}{D} = o$, and if we set $y' = y'_G + \eta$, $z' = z'_G + \zeta$ and $d(y,z) = d_o(1 + \delta(y,z))$ in Eqs. (49) and (50), where d_0 is the grating constant on the optical axis, then we obtain for the displacement of the Gaussian image point

$$\frac{\eta}{D} = \frac{m\lambda}{d_o}\left[\frac{3}{2}\left(\frac{y}{D}\right)^2 + \frac{1}{2}\left(\frac{z}{D}\right)^2 - \frac{3y}{2D}\frac{m\lambda}{d_o} + \frac{1}{2}\left(\frac{m\lambda}{d_o}\right)^2 - \delta(y,z)\right] \qquad (51)$$

$$\frac{\zeta}{D} = \frac{m\lambda}{d_o}\left[\frac{yz}{D^2} - \frac{z}{2D}\frac{m\lambda}{d_o} - \frac{\partial}{\partial z}\int_o^y \delta(w,z)\,dw\right] \qquad (52)$$

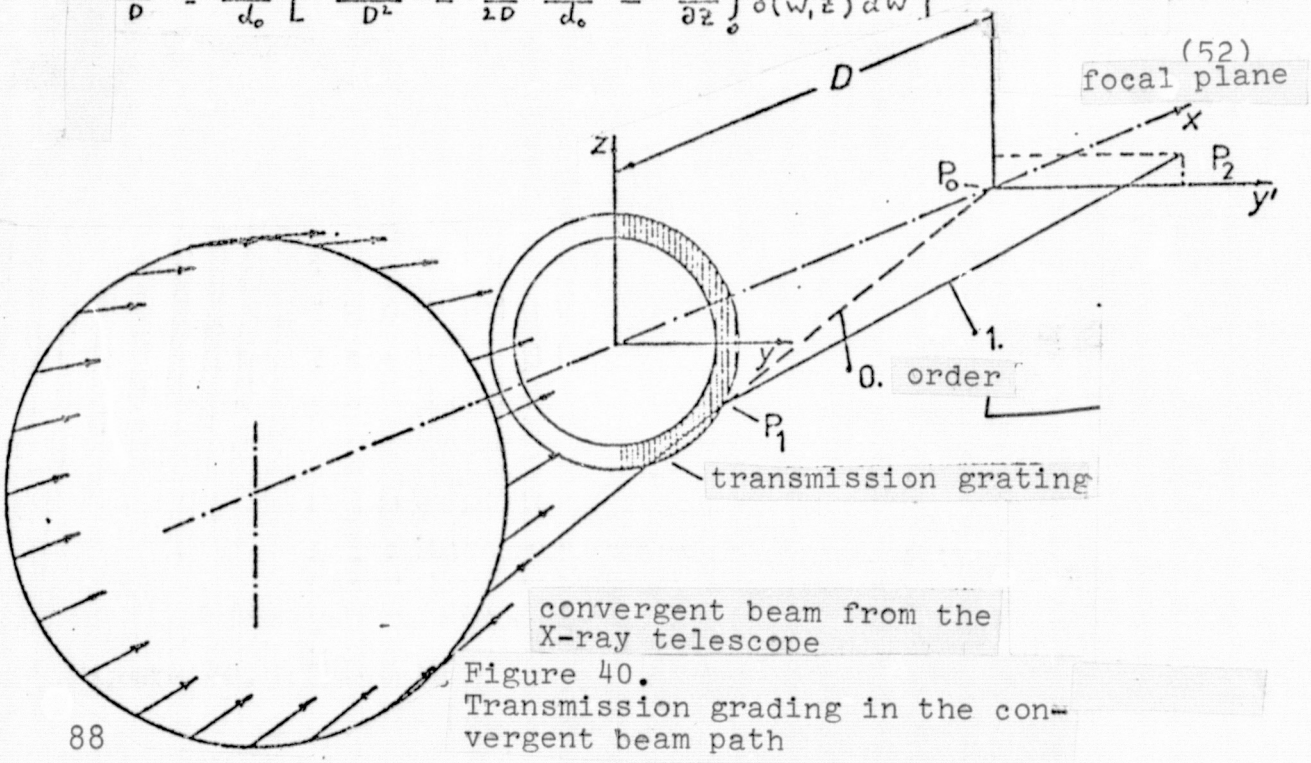

Figure 40.
Transmission grading in the convergent beam path

The first two terms in Eq. (51) together with the first term of Eq.(52) describe the comatic error. If we consider the case where only a small ring of radius R is illuminated on the grating, then the comatic error pattern is a circle of radius $r = \frac{1}{2}\left(\frac{R}{D}\right)^2 \frac{m\lambda}{d_o} \cdot D$ with its center displaced by 2r with respect to the Gaussian image point. In the case of an equidistant grating ($\delta = 0$) the comatic error is dominant for small wavelengths. If, by contrast, /104

$$\delta(y,z) = \frac{3}{2}\left(\frac{y}{D}\right)^2 + \frac{1}{2}\left(\frac{z}{D}\right)^2$$

is chosen, then the comatic error disappears altogether, since

$$\frac{\partial}{\partial z}\int_0^y \frac{3}{2}\left(\frac{w}{D}\right)^2 + \frac{1}{2}\left(\frac{z}{D}\right)^2 dw = \frac{yz}{D^2}$$

Thus, a coma-corrected grating must have a grating "constant" that increases toward the edge; in the case of the 32 cm telescope, the grating period would have to be varied by 0.01%. Such a variation is practically impossible for grating constants of 1μ or 0.5μ as are considered currently for soft X-ray wavelengths. A technically less difficult solution for the coma correction is the introduction of a curvature into the grating; this is shown in Figs. 41 a to d. The errors η and ζ as defined above are stated. Particularly interesting for point sources is the alternative 41b, since in the case of X-ray telescopes $\varphi^2 + \left(\frac{z}{D}\right)^2$ is very nearly constant. The comatic error does admittedly not disappear altogether, but it does not really make the resolution power much worse, since it only displaces the position of one line. An additional correction is possible by introducing a curvature of the focal plane [5].

The spectral resolution $\frac{\lambda}{\Delta\lambda}$ is given by the image error in the direction $\Delta y'$ of the dispersion to read

$$\frac{\lambda}{\Delta\lambda} = \frac{m\lambda D}{d_o \Delta y'} \qquad (53)$$

The spectral resolution is diminished, in addition to the consequences of grating errors, by image errors of the telescope, Δ_T, and the finite resolution of the detector, Δ_D :

Fig. 41a. Correction by means of variation of the grating period:

$$\frac{y'}{D} = \frac{m\lambda}{d_0}\left[1 - \frac{3}{2}\frac{y}{D}\cdot\frac{m\lambda}{d_0} + \frac{1}{2}\left(\frac{m\lambda}{d_0}\right)^2\right]$$

$$\frac{z'}{D} = \frac{m\lambda}{d_0}\left[-\frac{1}{2}\frac{z}{D}\frac{m\lambda}{d_0}\right]$$

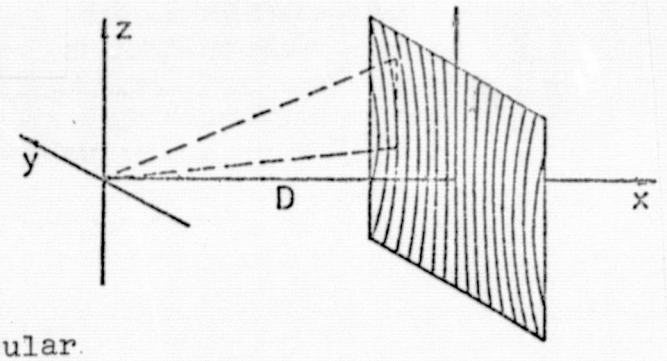

Fig. 41b. Curvature perpendicular to the grating direction around the focus:

$$\frac{y'}{D} = \frac{m\lambda}{d_0}\left[1 + \frac{\varphi^2}{2} + \frac{1}{2}\left(\frac{z}{D}\right)^2 - \varphi\frac{m\lambda}{d_0} + \frac{1}{2}\left(\frac{m\lambda}{d_0}\right)^2\right]$$

$$\frac{z'}{D} = \frac{m\lambda}{d_0}\left[\frac{z\varphi}{D} - \frac{1}{2}\frac{z}{D}\frac{m\lambda}{d_0}\right]$$

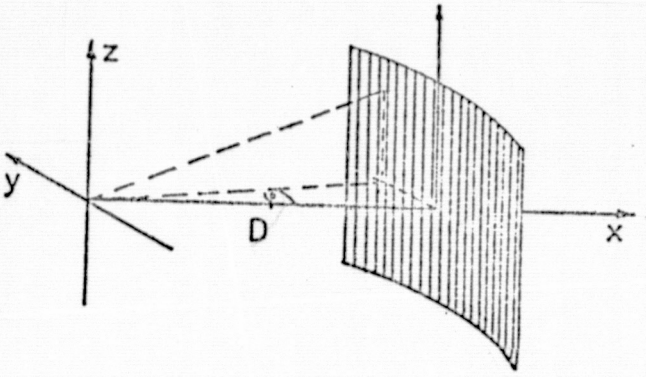

Figure 41c. Curvature parallel to the grating direction around the focus:

$$\frac{y'}{D} = \frac{m\lambda}{d_0}\left[1 + \frac{3}{2}\left(\frac{y}{D}\right)^2 - \frac{3}{2}\left(\frac{y}{D}\frac{m\lambda}{d_0}\right) + \frac{1}{2}\frac{m\lambda}{d_0}\right]$$

$$\frac{z'}{D} = 0$$

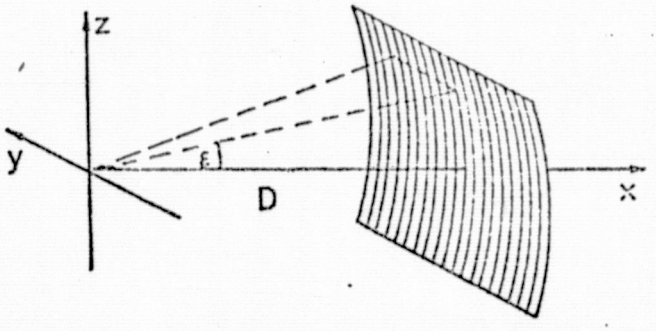

Figure 41d. Spherical curvature around the focus:

$$\frac{y'}{D} = \frac{m\lambda}{d_0}\left[1 + \frac{\varphi^2}{2} - \varphi\frac{m\lambda}{d_0} + \frac{1}{2}\left(\frac{m\lambda}{d_0}\right)^2\right]$$

$$\frac{z'}{D} = 0$$

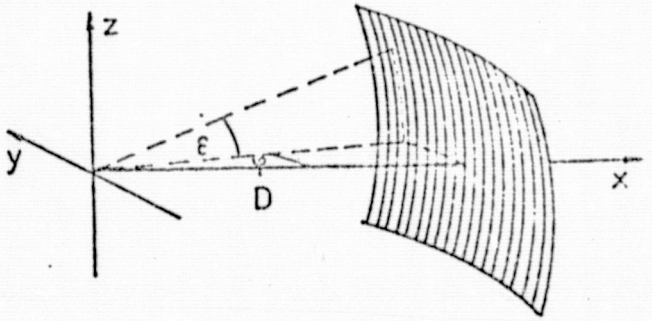

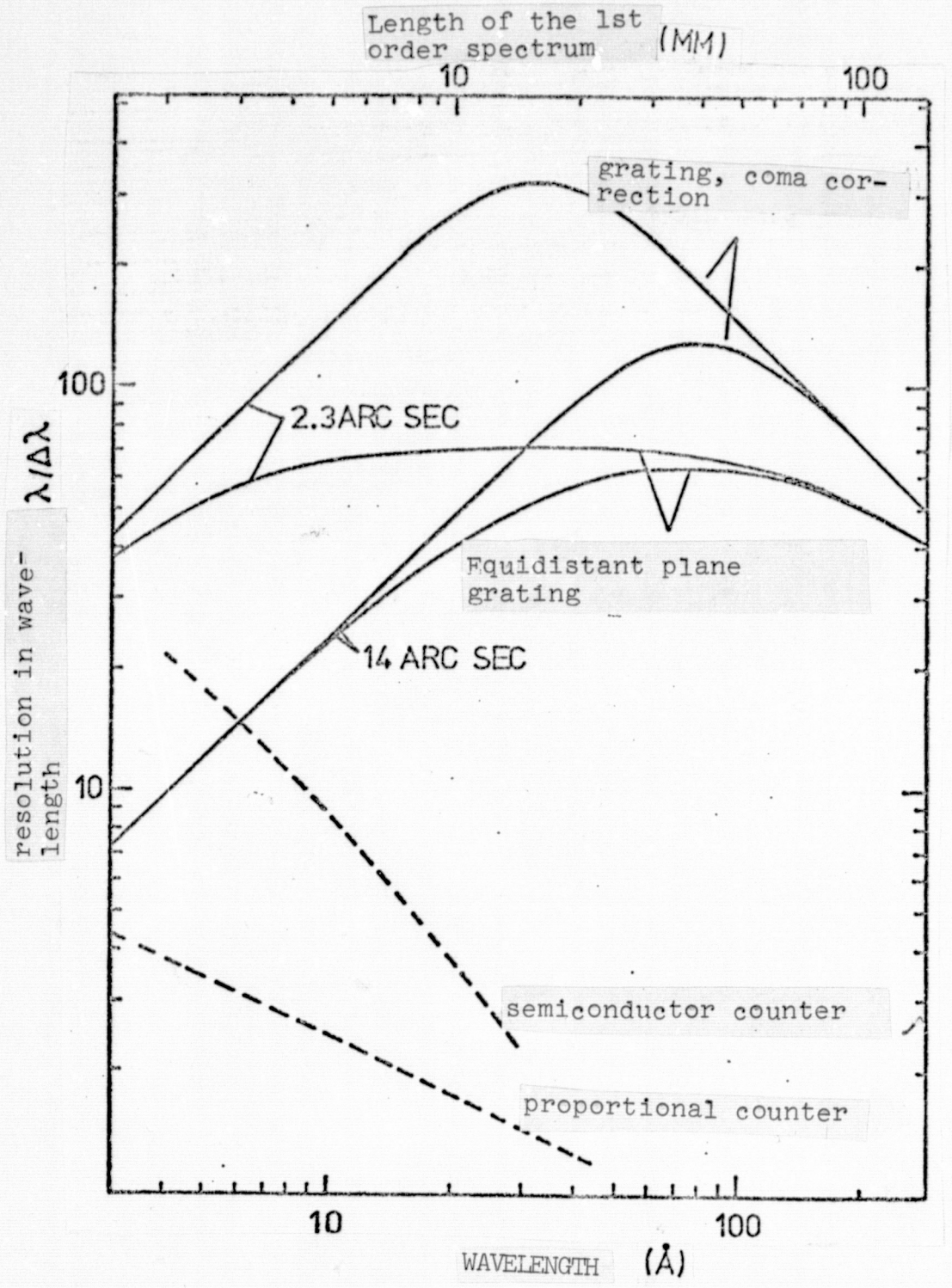

Figure 42. Comparison of the spectral resolution of a transmission grating in the beam path of an X-ray telescope ($\alpha = 1.5^{o}$, f = 300cm, D = 240cm, $d = 0.5\mu$) with the resolution of crystals and proportional counters

$$(\Delta y')^2 = (\Delta_T)^2 + (\Delta_D)^2 + (\Delta\eta)^2 \qquad /107$$

Here, $\Delta\eta$ is the grating error in the direction of dispersion.

Figure 42 shows a comparison of the resolution in various cases: The solid lines are the resolution power of a transmission grating together with an x-ray telescope($f = 300cm$, $\alpha = 1.5^o$) with or without coma correction for two different values of the angular resolution power of the telescope-detector system. At the short wavelengths, this angular resolution power is the dominant factor, so that the spectral resolution is proportional to λ, whereas for large wavelengths the resolution is proportional to λ^{-1} due to the increase of the astigmatism proportional to λ^2. In the case of the high-resolution telescope (2.3 arc sec) the grating correction results in the optimum wavelength range (30 to 40 Å) in an improvement by a factor of 5. $\tau = 1$ in this representation identifies the wavelength where the optical depth of 0.5μ gold grating elements reaches unity. In the most favorable energy ranges the spectral resolution of the telescope-grating combination is comparable with that of high-resolution crystal spectrometers.

The results of Section 5.2 were published in reference [4].

5.3. Position of the Transmission Grating /108

So far, we were concerned with the case where the transmission grating was placed into the convergent beam path behind the telescope. If, on the other hand, the transmission grating is placed in front of the X-ray telescope, then it is met by a plane wave, and no image errors occur in the grating so that no correction is required for the grating. However, the telescope now sees, in nth order, the source by $\frac{m\lambda}{d_o}$ outside of the axis, with the result that the off-axis errors of the telescope become important:

$$\sigma_{off} = \frac{1}{5}\,\frac{\tan^2\varepsilon}{\tan\alpha}\left(\frac{L_p}{f}\right) + 4\tan^2\alpha\cdot\tan\varepsilon$$

where $\tan\varepsilon = \frac{m\lambda}{d_o}$ (see Eq. (2)). In the case of the uncorrected grating behind the telescope we have for the error

$$\sigma_U = \left(\frac{m\lambda}{2d_o}\right)\tan^2 4\alpha + \frac{3}{2}\left(\frac{m\lambda}{d_o}\right)^2\tan 4\alpha$$

and for the corrected grating

$$\sigma_{korr} = \left(\frac{m\lambda}{d_o}\right)^2\cdot\frac{3}{2}\tan 4\alpha$$

The limit for the most favorable position of the grating in front of, or behind the telescope then reads

$$\frac{m\lambda}{d_o} = \frac{4\tan\alpha}{\frac{L_p}{5f\tan^2\alpha} - 6} \qquad (54)$$

in the case of the uncorrected grating, and

$$\frac{m\lambda}{d_o} = \frac{4\tan\alpha}{6 - \frac{L_p}{5f\tan^2\alpha}} \qquad (55)$$

in the case of the corrected grating (full coma correction). Fig. 43 shows this limiting line for a typical paraboloid length to focal length ratio of 0.1; both cases are represented. In the shaded area the position of the grating behind the telescope is more favorable.

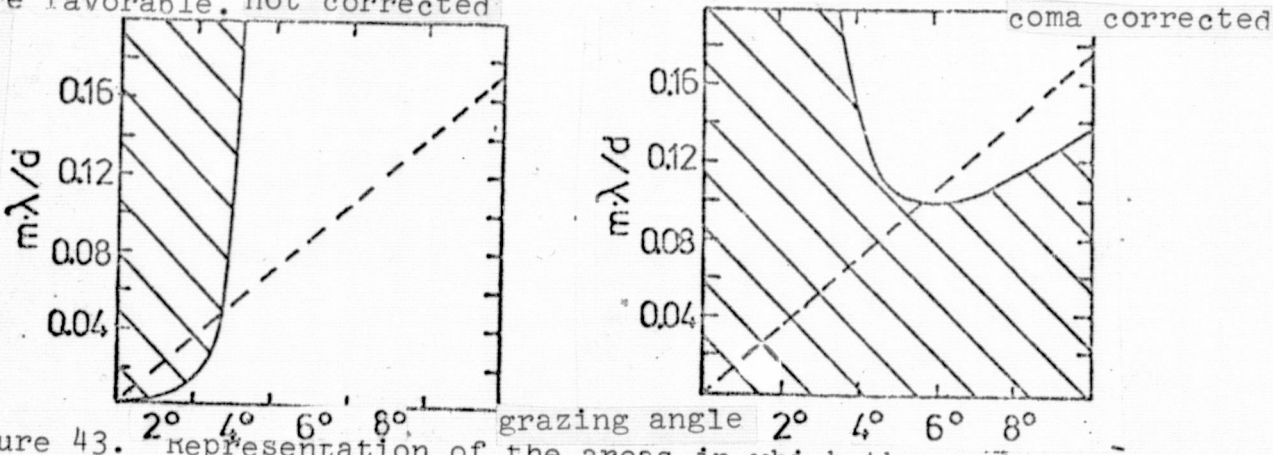

Figure 43. Representation of the areas in which the position of the grating behind the telescope causes less error than in the position in front of the telescope; dashed curve: $\frac{m\lambda}{d_o} = \tan\alpha$

If no coma correction is applied, the position behind /109
the telescope is only in a small area more favorable than the position in front of the telescope. By contrast, if the coma correction to the grating is applied, then for nearly all grazing angles and wavelengths ($\frac{m\lambda}{d_o} \leq \tan\alpha$) the position behind the telescope is more favorable. If only half the coma error is corrected, the limit does not depend on the wavelength: The position behind the telescope is more favorable if $\tan\alpha \leq \sqrt{\frac{1}{30}\frac{L_p}{f}}$ (for $\frac{L_p}{f} = 0.1$: $\alpha \leq 3.3^{\circ}$). Thus, in the soft X-ray range the position of the grating is optimal behind the telescope; in the XUV range a grating in front of the telescope may be more favorable, if a coma correction to less than one half is possible.

6. SUMMARY /110

The crucial point for a high-contrast image in the soft X-ray range of a mirror telescope is optimum polishing. We have shown on the basis of extensive scattering studies with plane samples that, aside from the glass and glass/ceramics materials well-known from optics, such as quartz, herasil, zerodur, and homosil, metals such as kanigen may yield good results: The best metal samples show scattering that corresponds to roughnesses between 2 and 3 Å.

The dependence of the scattering on the wavelength and the grazing angle was studied on the basis of three samples of different quality and compared with the statistical surface scattering theory. We were able to show that volume effects do not contribute significantly down to a surface quality of the order of 2 Å. The applicability of the surface scattering theory was verified by means of surface roughness measurements with the aid of perthometers, the FECO method, and the electron reflection microscope: Direct measurements of the roughness lead to the same results as the roughness determination from X-ray scattering measurements together with the scattering theory.

Applying optimized polishing methods and materials to the asperhical surfaces of the 32 cm telescope has led to a surface /111 quality that is even comparable to that of the glass mirrors of the high-resolution HEAO-B telescope: Whereas the HEAO-B telescope mirror shows an average roughness between 30 and 50 Å for the less perfect samples, the roughness of the mirrors of the 32 cm telescope is below 15 Å.

We have determined by means of computer simulation the point image function of the 32 cm telescope and its dependence on the off-axis angle and the position of the detector plane. The rms width of the point image function can be improved by a factor of about 2 by displacing the image plane at fixed off-axis angle; the FWHM width remains in the process essentially constant. Thus, the pointing is extremely important for astrophysical scattering halo measurements. Optical tests have shown that the 32 cm telescope is even with respect to the point resolution comparable in quality to the HEAO-B mirror.

The use of transmission gratings in connection with the telescope in the X-ray range promises hope for significant improvements of the spectral resolution if compared with proportional counters or semiconductor counters. The coma-corrected grating reaches even a resolution that is comparable to that of crystal spectrometers. In the XUV range the position of the grating behind the telescope is even with partial coma correction less favorable than the position in front of the telescope, if (in the case of typical mirror /112 length to focal length ratio of $L_f/f = 0.1$) the grazing angles exceed 3°.

The measurements reported in this thesis were carried out at the Astronomical Institute of the University Tubingen and at the Max-Planck Institut fur extraterrestrische Physik in Garching. Professor Trumper has aided me by useful discussions and suggestions which were crucial for the definition of the themes of my work. I

am particularly grateful to Dr. Brauninger and Mr. Stephan for their help with the measurements, and to Dr. Lichte for the reduction of the comparision measurements with the electron interference microscope. I am also grateful to the Zeiss Company in Oberkochen for our pleasant and successful collaboration.

REFERENCES /113

1. P. Beckmann, A. Spizzichino, The Scattering of Electromagnetic Waves from Rough Surfaces, (Pergamon Press, 1963).

2. H. E. Bennet, J. O. Porteus, Relation between Surface Roughness and Specular Reflectance at Normal Incidence, J. Opt. Soc. Am., Vol. 51, No 2, p. 123 (1961).

3. J. M. Bennett, Measurement of the rms roughness, autocovariance function and other statistical properties of optical surfaces using a FECO scanning interferometer, App. Opt., Vol. 15, No 11, p. 2705 (1976).

4. K. P. Beuermann, R. Lenzen, H. Brauniger, Properties of a transmission grating behind a grazing incidence telescope for cosmic x-ray spectroscopy, App. Opt., Vol. 16, No 5, p. 1425, (1977).

5. K. P. Beuermann, H. Brauniger, J. Trumper, Experimental and theoretical properties of x-ray transmission gratings, New Instrumentation for Space Astronomy, Pergamon Press (1978).

6. M. A. Blochin, X-ray Physics, BEB Verlag Technik, Berlin (1957).

7. J. Bouguer, Histoire de l'Academie Royale des sciences, Paris (1757).

8. J. Bouguer, Traite d'optique sur la gradation de la muniere. (Paris (1760).

9. R. C. Chase, L. P. Van Speybroeck, Wolter-Schwarzschild Telescopes for x-Ray Astronomy, App. Opt., Vol. 12, No 5, p. 1042 (1973).

10. A. H. Compton, S. K. Allison, X-Rays in Theory and Experiment Van Nostrand, Princeton, (1935). /114

11. E. Costa, G. Auriemma, L. Boccaccini, P. Ubertini, Reflectivity of gold coated surfaces in the soft x-ray range App. Opt. Vol. 17, No. 4, pl 621 (1978).

12. H. Davis, The Reflection of Electromagnetic Waves from Rough Surface Proc. I.E.E., Pt III, 101, p. 209 (1954)

13. J. Eastman, P. Baumeister, The Microstructure of Polished Optical Surfaces Opt. Comm., Vol 12. No. 4, p. 418 (1974).

14. W. Ehrenberg, X-Ray Optics: Imperfections of Optical Flats and Their Effect on the Reflection of X-rays. Ann. d. Phys., Bd. 10, p. 715, (1931)

15. O. A. Ershov, I. A. Brytov, A. P. Lukirskii, Reflection of X-rays from Certain Substances in the Region from 7 to 44Å Opt. and Spectr. Vol. 18, no 1, p. 66, (1965).

16. J. V. Feitzinger, The Zone Plate, Bundesministerium fur wissenschaftliche Forschung, Report W 68-63 (1968).

17. E. G. Flowers, J. F. Lee, M. A. Ruderman, P. G. Sutherland, W. Hillebrandt, E. Muller, Variational Calculation of Ground-State Energy of Iron Atoms and Condensed Matter in Strong Magnetic Fields, Astrophys., J., no 15, p. 291 (1977).

18. P. Gorenstein, H. Gursky, F. R. Harnden, Jr. Large area soft x-ray imaging system for cosmic x-ray studies from rockets I.E.E.E. Trans. on Nuc. Sci. NS-22, p. 616 (1975).

19. O. J. Guentert, Study of the Anomalous Surface Reflection of X-rays J. of App. Phys., Vol. 36, No 4, p. 1361 (1965). /115

20. B. P. Hildebrand, R. L. Gordon, E. V. Allen, Instrument for Measuring the Roughness of Supersmooth Surfaces App. Opt., Vol. 13, No. 1, p. 177 (1974).

21. G. W. Hopkins, Proximate Ray Tracing and Wave Aberration Coefficients J. Opt. Soc. Am., Vol. 66, No 9, 942 (1976).

22. H. Horner, X-Ray Spectroscopy of Optically Thin Plasmas with Spectrometers of Limited Resolution, Diplom (M.S.) Thesis, MPE Garching (1977).

23. P. A. J. de Korte, R. Laine, Soft X-Ray Scattering from highly polished surfaces submitted to Appl. Opt.

24. R. Lenzen, J. Trumper, Reflection of x-rays by neutron star surface, Nature, Vol. 271, p. 216 (1978).

25. R. Lenzen, Investigation of the Scattering of Soft X-Rays Upon Reflection by Plane Mirrors, Diplom (M.S.)Thesis, University Tubingen (1975).

26. H. Lichte, A Direct Light Interference Microscope for Electron Waves Ph.D. Thesis, University Tubingen (1977).

27. A. P. Lukirskii, E. P. Savinov, O. A. Ershov. Yu. F. Shepelev, Reflection Coefficient of Radiation in the Wavelength Range from 23.6 to 113 A for a Number of Elements and Substances and the Determination of the Refractive Index and Absorption Coefficient, Opt. and Spectr., Vol. 16, p. 168. (1964).

28. A. P. Lukirskii, E. P. Savinov, O. A. Ershov, I.I. Zhukova,/116 V. A. Fomichev, Reflection of X-rays with Wavelengths from 23.6 to 190.3A. Some Remarks on the Performance of Diffraction Gratings Opt. and Spect., Vol. 19, No 2, p. 237, (1965).

29. A. I. Mahan, C. V. Bitterli, Total internal reflection: a deeper look App. Opt. Vol. 17, No. 4, p. 509 (1978).

30. I. G. Nomarski, A. R. Weill, Application a la metallographie des methodes interferentielles a deux ondes polarisees. Rev. de Metallurge, Vol. 52, p. 121, (1955).

31. R. Novick, M. C. Weisskopf, J. R.P. Angel, P. G. Sutherland, The Effect of Vacuum Birefringence on the Polarization of X-Ray Binaries and Pulsars, Astroph. J. Vol. 215, pL117, (1977).

32. E. Rausch, Integral Reflection Measurements with Polished Samples in the Soft X-ray Range, M.S. Thesis, University Tubingen, (1975).

33. M.A. Ruderman, Physics of Dense Matter, IAU Symposium No. 53, Reidel, Dordrecht (1974)

34. P. Sanford, K. O. Mason, J. Ives, Observation of a Line Feature in the X-Ray Spektrum of Cygnus X-3 Mpn. Not. R. Astr. Soc., Vol. 173 p9p (1975).

35. E. P. Savinov, I. I. Lyakhovskaya, O.A. Ershov, E. A. Kovalyera, Graphical Solution of the Fresnel Equations and the Calculation of Optical Constants in the Ultrasoft X-Ray Region of the Spectrum, Opt. and Spekt, Vol. 27, No 1, p. 176 (1970).

36. J. B. Schroeder, R. G. Klimasewski, Scattering from X-Ray /117 Reflecting Surfaces, App. Opt, Vol. 7, No 10, p. 1921, (1968).

37. P. J. Serlenitsos, E. A. Boldt, S. S. Holt, R. E. Rothschild, J.L.R. Saba, Spectral variability of Cygnus-X-3 Astroph. J., Vol. 201, pL9 (1975).

38. E. A. Stewardson, J. H. Underwood, The reflection of soft x-rays by polished surfaces of glass and steel., Brit. J. Appl. Phys., Vol. 16, p. 1877 (1965).

39. L. P. Van Speybroeck, R.C. Chase, Design Parameters of Paraboloid-Hyperboloid Telescopes for X-Ray Astronomy App. Opt. Vol. 11, No 2, p. 440 (1972).

40. H. Spiegelhauer, Scattering of X-Ryas on Interstellar Dust, PH.D Thesis, University Tubingen (1978).

41. T. H. Stix, The Theorie of Plasma Waves, McGraw-Hill, New York, (1962).

42. W. H. Tacker, M. Koren, Radiation from a High Temperature, Low Density Plasma: The X-Ray Spectrum of the Solar Corona, Astroph. J., No. 168, p. 283 (1971).

43. T. S. Trowbridge, K. P. Reitz, New Ray Optical Model for the Directional Distribution of Light Reflected from a Rough Surface, Techn. Publ. TP-75-01 of Naval Missile Center (1975).

44. J. Trumper, W. Pietsch, C. Reppin, B. Sacco, E. Kendziorra, R. Staubert, Evidence for Strong Cyclotron Emission in the Hard X-Ray Spectrum of Her X-1., Prc. VIII Texas Symp., on Rel. Astrophs. (1977).

45. H.F.A. Tschunko, Imaging Performance of Annular Apertures App. Opt., Vol 13, No 8, p. 22 (1974). /118

46. V. Twersky, On Scattering and Reflection of Electromagnetic Waves by Rough Surfaces, Trans. I.R.E. Ap-5, p. 81, (1957).

47. J. Ventura, Collision Frequency and Coulomb Scattering in an Intense Magnetic Field, Phys. Rev., Vol. 18, No. 6, p. 3021 (1973).

48. M. C. Weisskopf Design of Gracing-Incidence X-Ray Telescopes 1, App. Opt., Vol. 12, No 7, p. 1436 (1973).

49. W. Werner, Imaging Properties of Wolter I Type X-Ray Telescopes, App. Opt. Vol 16, No 3, (1977).

50. C. E. Winkler, D. Korsch, Primary Aberrations for Gracing Incidence, App. Opt. Vol. 16, No 9, p. 2464 (1977).

51. H. Wolter, Mirror Systems with Grazing Incidence as Imaging Optical Systems for X-Ryas, Annalen der Physik, 10, 94 (1952).

52. H. Wolter, Generalized Schwarzschild Mirror Systems with Grazing Reflection as Optical Systems for X-Rays, Annalen der Physik, 10, 286 (1952).

53. R. S. Wriston, J. F. Froechtenigt, Soft X-Ray Scattering by Optical Surfaces, App. Opt., Vol 12, No 1, p 25. (1973).

54. Y. Yoneda, Anomalous Surface Reflection of X-Rays, Phys. Rev., Vol. 131, No 5, p 2010 (1963).

55. Atomic Data, Vol 5, No. 1, p. 49 (1973).

CURRICULUM VITAE

[redacted]

1954	Primary School: Diesterweg Schule, Moers
1958	Transferred to Gymnasium Moers (Classical Branch)
7.3.1967	(High-School) Diploma
10.2.1967	Military Service (Discharged 31 March 1969)
10.4.1969	Studies at University Tubingen
7.15.1971	Vorprufung (B.S.), physics
4.21.1975	Diplom (M.S.) Thesis (Astronomical Institute): "Studies of the Scattering of Soft X-rays Under Reflection by Plane Mirrors"
8.1. 1975	Ph.D. Thesis Studies at the Max-Planck-Institut for extraterrestrische Physik, Garching. Subject: "Imaging Properties of an X-ray Telescope of the Type Wolter-I, Taking Specifically the Contrast Decrease due to Diffuse Reflection Into Account" Readers: Professors Trumper and Brauninger

Academic Teachers: W. Braunbek, G. Elwert, F. Gonnenwein, H. Kruger, F. Lenz, G. Mack, G. Mertens, H. Mitter, G. Mollenstedt, H. Stumpf, J. Trumper, A. Wolf.